Design and Characterization of Dual-Matrix Composite Deployable Space Structures

Thesis by

Maria Sakovsky

In Partial Fulfillment of the Requirements

for the Degree of

Doctor of Philosophy

California Institute of Technology

Pasadena, California

2018

(Defended May 21, 2018)

To my sister, Elizabeth,

may everyone be as passionate about their dreams as you.

Acknowledgements

This work could not have been done without the help and support of so many here at Caltech and around the world. Firstly, I would like to extend my sincerest thanks to my adviser, Prof. Sergio Pellegrino, without whom this research would not have been possible. His guidance on research directions, technical matters, presentation techniques, and how to navigate the academic world have been invaluable over my five years at Caltech. I would also like to thank all members of my candidacy and defense committees: Prof. Dennis Kochmann, Prof. Michael Ortiz, Prof. Ali Hijimiri, Prof. Guruswami Ravichandran, and Prof. Chiara Daraio. Their feedback has had a big positive impact on my research. I also thank Prof. Wolfgang Knauss and Prof. Kawai Kwok for their helpful discussions on viscoelasticity. Thank you also to Prof. Julia Greer for allowing me to use the equipment in the research lab.

This research was done in collaboration with Dr. Joseph Costantine at the University of New Mexico. I am grateful for all of his patience explaining the workings of antennas, a field that was a mystery to me prior to our collaboration. I would also like to thank Dr. Christos Christodoulou and Dr. Youssef Tawk for their helpful input.

I would like to thank the AFOSR for the funding that made this research possible (award no. FA9550-13-1-0061, program manager Dr. David Stargel).

I would also like to thank the Keck Institute for Space Studies (KISS) for their financial support during my first year at Caltech. I extend a big thank you to Tom Prince. My deepest gratitude goes to Michele Judd for her tireless work organizing incredible lectures and teaching me the value of networking – she is a role model and an inspiration to me.

I also extend my thanks to all of the members of JPL who I have had the opportunity to work with over this time. I thank Charles Elachi, Alina Moussessian, and Jon Mihaly for their technical advice and mentorship while working on the Europa Clipper radar. I would also like to thank Greg Davis, Dan Scharf, Anthony Freeman, and Oscar Alvarez-Salazar for their advice.

I would like to acknowledge all of my colleagues at the Space Structures Laboratory (SSL) at Caltech. My deepest thank you to Dr. Ignacio Maqueda who began this research and for his mentorship during my first few years at SSL. I would also like to thank my labmates – past and present – for their years of technical advice, feedback on my presentations, moral support, and so much more: Manan Arya, Miguel Bessa, Stephen Bongiorno, Federico Bosi, Max Braun, Melanie

Delapierre, Serena Ferraro, Terry Gdoutos, Ashish Goel, Kristina Hogstrom, Kathryn Jackson, Wilfried Jahn, Christoph Karl, Marie Laslandes, Christophe Leclerc, Nicolas Lee, Yang Li, Chinthaka Mallikarachchi, Michael Marshall, Xin Ning, Antonio Pedivellano, Fabien Royer, Arthur Schlothauer, John Steeves, Thibaud Talon, Daniel Turk, Yuchen Wei, and Lee Wilson. I also extend my thank you to John Baker, Jim Breckinridge, and Andrew Shapiro.

I would also like to thank the administrative and research staff of GALCIT – Kate Jackson, Christine Ramirez, Peggy Blue, Dimity Nelson, Jamie Meighen-Sei, Stephanie Rider, Lydia Suarez, and Petros Arakelian. A big thank you also to the GALCIT machine shop staff for making the best out of my drawings – Joe Haggerty and Ali Kiani. My gratitude is furthermore extended to Jackie Gish who has been a wonderful mentor over my time at Caltech.

I also extend my gratitude to the Intentional Students Programs at Caltech and to Laura Flower Kim and Daniel Yoder – they made immigration a little bit less of a headache and for that I am forever grateful.

My thanks go to my dearest friends – whether at Caltech, Toronto, or scattered across the world – I could not have done this without their unwavering support.

To my better half I give my warmest thanks for his advice when I was indecisive, for his support when I needed it most, and for encouraging me to face my fears. I am grateful to have him by my side.

Most importantly, to my parents and my sisters I extend my deepest appreciation for always encouraging me to pursue my dreams, being by my side day and night despite the physical distance between us, and for believing in me even when I did not believe in myself. Without you, I would not have made it half as far – thank you!

Abstract

Dual-matrix composites are a promising approach to deployable high performance antennas for small satellites. Several techniques exist for packaging large antenna apertures. Assemblies of rigid bars and hinges obtain high deployed precision but are heavy and mechanically complex. Thin shell structures deployed using stored strain energy are a lightweight alternative offering efficient packaging but reduced surface precision. Moreover, elastomer composites shells attain even smaller fold radii upon packaging but are limited by the deployed structure's stiffness. Dual-matrix composites combine the advantages of several of these approaches to enable larger antenna apertures. They consist of a continuous woven fiber reinforcement with an elastomer matrix embedded in localized hinge regions and a stiff epoxy resin elsewhere. Such structures can achieve small fold radii, are strain energy deployable, and promise high deployed stiffness.

This research demonstrates the capabilities of the proposed dual-matrix structures through direct comparison to existing antenna designs. Analytic scaling relations between structural and electromagnetic performance of various deployable antenna designs are developed. These are used to rapidly predict achievable antenna performance as a function of a common set of antenna geometric parameters. Plotting of this data on a coordinated set of 2D design plots enables the direct comparison of antenna concepts and the selection of specific designs meeting all requirements. This methodology was used to design a deployable dual-matrix composite conical log spiral (CLS) antenna for use on CubeSats which outperformed existing off-the-shelf designs through higher gain, higher bandwidth, and more efficient packaging.

Starting from this initial design, the antenna is tuned to maximize performance and an assembly including the CubeSat, dual-matrix antenna, dual-matrix hinge for antenna deployment, and a flexible feeding network is developed. All portions of the assembly are prototyped and tested. The antenna electromagnetic performance is predicted using ANSYS HFSS and verified by testing in an anaechoic chamber with antenna gains predicted within 4% of measured values. Structural stiffness is characterized through the antenna's fundamental frequency with simulated performance in the Abaqus finite element software within 6% of measured values. Comparison of antenna performance before and after packaging and deployment shows the structural frequency, antenna gain, and antenna bandwidth are unaffected by folding, demonstrating that dual-matrix composites are appropriate for use as deployable structures.

Techniques for the quasi-static deployment of dual-matrix composites are presented. An analytic minimum energy method, which accounts for fiber microbuckling in regions of high curvature, is used to predict the folded shape and deployment moments of a dual-matrix hinge. The model shows excellent agreement with LS-Dyna finite element simulations for a variety of material properties. Comparison with experimental characterization demonstrates the capability of the models to predict folded radii and deployment moment of a prototype hinge withing 5% of measured values. The developed analysis tool-set enables a design of deployment restraints and mechanisms.

The woven elastomer composites forming the fold regions in dual-matrix composites have been the subject of very few studies. Existing methods for predicting the stiffness of woven epoxy composites are applied to elastomer composites here and show poor agreement with measurements. A novel approach is presented for the prediction of tow stiffness in elastomer composites using a semi-empirical approach. The reinforcing efficiency parameter in the well-established Halpin-Tsai model for tow homogenization is estimated using experimental measurements of stiffnesses of several laminates. It is shown that for elastomer composites, the parameter values are orders of magnitude higher than the heuristic values used for epoxy composites. The method is used to predict the stiffness of woven epoxy and elastomer composites making up the dual-matrix structures studied in this work showing agreement withing 15% of experimental measurements for arbitrary layups. The method is extended to the prediction of viscoelastic behavior of dual-matrix structures to enable investigation of deployment reliability after long storage times.

Published Content and Contributions

M. Sakovsky, S. Pellegrino, J. Costantine, *Rapid Design of Deployable Antennas for CubeSats*, IEEE Antennas and Propagation Magazine, DOI: 10.1109/MAP.2017.2655531, April 2017.

Developed antenna rapid design tool, user interface, and case studies.

M. Sakovsky, S. Pellegrino, J. Costantine, *Rapid Deployable Antenna Concept Selection for CubeSats*, 37th ESA Antenna Workshop, Noordwijk, the Netherlands, 2016.

Contributed antenna rapid design tool, user interface, and case studies.

J. Costantine, Y. Tawk, I. Maqueda, G.M. Olson, **M. Sakovsky**, S. Pellegrino, C.G. Christodoulou, *UHF Deployable Helical Antennas for CubeSats*, IEEE Transactions on Antennas and Propagation, Vol 64 (9), pg. 3752-3759, DOI: 10.1109/TAP.2016.2583058, 2016.

Contributed mechanical aspects of conical log spiral antenna in the study.

M. Sakovsky, S. Pellegrino, H.M.Y.C. Mallikarachchi, *Folding and Deployment of Closed Cross-section Dual-matrix Composite Booms*, SciTech 2016, San Diego, AIAA-2016-0970, https://doi.org/10.2514/6.2016-0970.

Contributed finite element models for single matrix booms as well as all experimental measurements.

M. Sakovsky, I. Maqueda, C. Karl, S. Pellegrino, J. Costantine, *Dual-Matrix Composite Wideband Antenna Structures for CubeSats*, AIAA Spacecraft Structures Conference, 5-9 January 2015, Kissimmee, FL, AIAA 2015-0944, https://doi.org/10.2514/6.2015-0944.

Contributed fabrication procedures, experimental and finite element frequency studies.

Contents

Acknowledgements iv

Abstract vi

Published Content and Contributions viii

List of Figures xii

List of Tables xvii

1 Introduction 1

1.1 Motivation . . . 1

1.2 Research Goals and Outline . . . 5

2 Rapid Design of Deployable Antennas for Small Satellites 8

2.1 Introduction . . . 8

2.2 Overview of Antenna Performance Metrics . . . 9

2.3 Design Methodology . . . 10

2.3.1 Antenna Types . . . 10

2.3.2 Structural Architectures and Packaging Schemes . . . 12

2.3.3 Predicting Antenna Performance . . . 13

2.3.4 Plots of Performance Metrics . . . 15

2.4 Preliminary Design Tool . . . 16

2.5 Case Studies . . . 17

2.5.1 UHF Antenna Design . . . 17

2.5.2 Ka-Band Case Study . . . 20

2.6 Conclusion . . . 23

3 Dual-Matrix Composite Antenna Prototype 24

3.1 Introduction . . . 24

3.2 Antenna-CubeSat Assembly . . . 25

3.3 Prototype RF Performance . . . 26

3.3.1 Antenna Geometry Optimization . . . 27
3.3.2 Antenna Position Optimization . . . 28
3.4 Antenna Feeding Network . . . 29
3.4.1 RF Testing . . . 30
3.5 Prototype Structural Performance . . . 31
3.5.1 Prediction of Vibration Modes . . . 31
3.5.2 Measured Vibration Modes . . . 35
3.6 Conclusion . . . 38

4 Fabrication and Material Characterization 39
4.1 Introduction . . . 39
4.2 Constituent Materials . . . 40
4.3 Dual-Matrix Composite Fabrication Techniques . . . 41
4.4 Interface Characterization . . . 43
4.5 Microstructure Characterization . . . 45
4.5.1 Micrographs . . . 45
4.5.2 Plain-Weave Geometry . . . 46
4.5.3 Composite Fiber Volume Fraction . . . 47
4.5.4 Tow Fiber Volume Fraction . . . 48
4.6 Analytic Predictions of Stiffness . . . 49
4.7 Experimental Techniques for Stiffness Measurement . . . 50
4.7.1 Tension Tests . . . 50
4.7.2 Four-Point Bending Tests . . . 51
4.8 Comparison of Experimental and Analytic Stiffness . . . 52
4.8.1 Effects of Fiber Microbuckling . . . 57
4.9 Conclusion . . . 57

5 Quasi-Static Deployment of Dual-Matrix Composite Hinges 59
5.1 Dual-Matrix Hinge . . . 59
5.1.1 Hinge Geometry . . . 59
5.1.2 Hinge Fabrication . . . 59
5.1.3 Composite Stiffness . . . 60
5.1.4 Analytic Model . . . 62
5.1.5 Quasi-static Deployment Experiments . . . 65
5.2 LS-Dyna Finite Element Simulations . . . 67
5.2.1 Finite Element Model Description . . . 69
5.2.2 Quasi-Static Simulations with an Explicit Solver . . . 70

5.2.3 Explicit Model Parameter Selection . . . 71
5.2.4 Implicit Model Parameter Selection . . . 72
5.3 Finite Element Results and Discussion . . . 72
5.3.1 Comparison of Models . . . 72
5.3.2 Folded Hinge Shape . . . 73
5.3.3 Deployment Moments . . . 75
5.3.4 Torsional Behavior . . . 76
5.4 Conclusion . . . 76

6 Semi-Empirical Models for Stiffness of Plain-Weave Composites 79
6.1 Introduction . . . 79
6.2 Tow Homogenization Models . . . 80
6.2.1 Tow Homogenization Implementation . . . 82
6.3 Plain-Weave Homogenization Models . . . 84
6.3.1 Plain-Weave Homogenization Implementation . . . 85
6.4 Investigation of Composite Tow Properties . . . 87
6.4.1 Applying Existing Models for Epoxy Composites . . . 87
6.4.2 Sensitivity to Tow Stiffness . . . 90
6.5 Dependence on Unit Cell Geometry . . . 93
6.5.1 Sensitivity to h^{FE} and L^{FE} . . . 94
6.5.2 Dependence on Fiber Volume Fractions . . . 99
6.6 Optimization of Woven Laminate Stiffness . . . 101
6.6.1 Model Description . . . 101
6.6.2 Results . . . 102
6.7 Conclusion . . . 103

7 Viscoelastic Characterization of Dual-Matrix Composites 105
7.1 Introduction . . . 105
7.2 Linear Viscoelasticity . . . 106
7.3 Matrix Viscoelastic Characterization . . . 107
7.3.1 Pure Silicone Samples . . . 108
7.3.2 Experimental Techniques . . . 108
7.3.3 Data Analysis . . . 109
7.3.4 Silicone Master Curve . . . 109
7.3.5 Epoxy Master Curve . . . 110
7.4 Modeling of Woven Viscoelastic Composites . . . 112
7.4.1 Model Description . . . 112

7.4.2 Results and Experimental Validation 112
7.5 Conclusion 115

8 Conclusions **116**
8.1 Contributions 118
8.2 Future Work 119

A Design Equations for Electromagnetic and Structural Performance Metrics **121**

B Interconversion Between Creep Compliance and Relaxation Modulus **125**

Bibliography **127**

List of Figures

1.1 (A) 1U CubeSat unit [1] (B) COTS CubeSat dipole antenna [2] (C) COTS CubeSat patch antenna [3] 1

1.2 (A) CubeSat dipole antenna deployed using a mechanical hinge [2] (B) Astromesh reflector [4] (C) Ultra-compact Ka-band parabolic deployable antenna [5] 2

1.3 (A) CubeSat tape-spring deployable antenna [6] (B) Helios UHF deployable antenna [7] (C) Deployable CubeSat mesh reflector with compliant ribs [8] (D) Skynet 4 UHF antenna [9] (E) Spring back reflector antenna [10] 3

1.4 Elastic fiber microbuckling on the compression side of a folded elastic memory composite [11] 4

1.5 (A) Schematic of folding of a dual-matrix composite hinge (B) Folding of an origami crane using carbon fiber composite reinforced with epoxy and silicone [12] (C) Concept for a conical antenna packaged using dual-matrix composites [13] 5

2.1 Generic antenna radiation pattern 2D slice 9

2.2 Geometry of antennas chosen for the present study 11

2.3 Packaging schemes for CubeSat antennas (A) Dipole packaged using mechanical hinge [2] (B) Dipole packaged using tape springs [6] (C) Helix packaged using helical pantograph [14] (D) Helix packaged using coilable conductors [7] (E) CLS packaged using dual-matrix composite shell [15] (F) Reflector packaged using hinged ribs [5] (F) Reflector packaged using mesh wrapping [8] 14

2.4 Algorithm for estimating antenna performance 15

2.5 Schematic of design charts for comparing antenna performance 16

2.6 Concept selection tool input screen © 2017 IEEE 17

2.7 Concept selection chart for the design of a high performance UHF antenna operating at 450 MHz that folds in a 3U CubeSat. The red and black dots indicate helix and CLS antenna performance, respectively, designed using numerical simulations © 2017 IEEE 19

2.8 Case study at f = 30 GHz. From left to right, the plots shows antenna height/diameter as a function of gain, bandwidth, structural frequency, and the packaged antenna dimensions. The shaded regions represent areas of the plots that meet imposed requirements. 22

3.1 CubeSat assembly with deployed antenna and feeding network 25
3.2 Steps in antenna deployment from CubeSat 26
3.3 Folding of dual-matrix antenna by flattening and z-folding 26
3.4 Geometry parameters of interest in the design of a CLS antenna 27
3.5 (A) Reflection coefficient of select antenna designs (B) Cut in the y-z plane of radiation pattern at 450 MHz 28
3.6 Geometry of flexible microstrip lines (A) Chebishev tapering (B) cross-section 29
3.7 Reflection coefficient of feed network 30
3.8 CLS antenna and CubeSat assembly mounted in anechoic chamber at the University of New Mexico for radiation pattern measurements 31
3.9 RF measurements of antenna prototype (A) reflection coefficient (B) radiation pattern cuts at 450 MHz (C) gain as a function of operating frequency 32
3.10 ABAQUS model of dual-matrix conical shell with free boundary conditions. 32
3.11 Mode shapes for the 3 first natural frequencies of the antenna (A) hinges unfolded (B) hinges with 40% of original stiffness 34
3.12 Experimental setup for vibration analysis 35
3.13 Experimental setup for vibration analysis 36
3.14 Frequency response function of antenna (A) top laser reading (B) bottom laser reading 37

4.1 Fabrication of a dual-matrix composite antenna (A) Masking of silicone hinges and epoxy transfer via heat (B) Stacking of plies and embedding of conductor (C) Impregnation of hinge regions with silicone (D) UV-cure of silicone (E) Epoxy cure in autoclave 42
4.2 Micrograph of the interface region between the AQ/epoxy and AQ/silicone composites 43
4.3 Indentation load curves with unloading slopes indicated for (A) epoxy (B) silicone . . 44
4.4 Micrograph at 10X magnification of the microstructure of a $[0_3]_{pw}$ AQ/epoxy composite 45
4.5 Micrograph at 10X magnification of the microstructure of a $[0_3]_{pw}$ AQ/silicone composite 46
4.6 Micrograph at 20X magnification of the microstructure of a $[\pm 30/0]_{s,pw}$ AQ/epoxy composite with embedded conductor 46
4.7 Notation for force and moment resultants in CLT 49
4.8 Unit cell used to approximate a plain-weave in the mosaic model 50
4.9 Setup used to measure in-plane stiffness 51

4.10 Setup used to measure bending stiffness . . . 52
4.11 Tension test data of AQ/epoxy composite (A) $[0]_{pw}$ (B) $[45]_{pw}$ (C) $[0_3]_{pw}$ (D) $[45_3]_{pw}$ 53
4.12 Tensions test data of AQ/silicone composite (A) $[0]_{pw}$ (B) $[45]_{pw}$ (C) $[0_3]_{pw}$ (D) $[45_3]_{pw}$ 54
4.13 Four-point bending test data of AQ/epoxy composite (A) $[0_3]_{pw}$ (B) $[45_3]_{pw}$ (C) $[45/0/45]_{pw}$ . . . 55
4.14 Four-point bending test data of AQ/silicone composite (A) $[0_3]_{pw}$ (B) $[45_3]_{pw}$ (C) $[45/0/45]_{pw}$ . . . 56
4.15 Bending stiffness of $[45/0/45]_{pw}$ AQ/silicone composite before folding (dashed lines) and after folding to 180° (solid lines) . . . 57

5.1 Geometry of dual-matrix hinges (A) definition of hinge geometric parameters (B) illustration of hinge folding . . . 60
5.2 Fabricated dual-matrix hinges (A) hinge with no slot (w_s = 0 mm) (B) hinge with a w_s = 50 mm slot . . . 60
5.3 (A) single tape spring geometry (B) equal-sense bending (C) opposite-sense bending. . 62
5.4 Predicted reaction moments (A) single tape-spring (B) combination of two tape-springs. 62
5.5 Cross-section of fold area of dual-matrix hinge. . . . 63
5.6 Experimental setup used to measure the moment response of the hinge during deployment 66
5.7 Experimentally measured moment response during deployment of hinges with various slot lengths . . . 66
5.8 Experimental DIC setup for metrology of folded hinge shape . . . 67
5.9 Longitudinal radius of curvature of outer tape-spring of dual-matrix hinge with w_s = 0 mm, for several deployment angles . . . 68
5.10 Longitudinal fold radius for dual-matrix hinge with w_s = 0 mm . . . 68
5.11 LS-Dyna model of the dual-matrix hinge . . . 70
5.12 Effects of contact penalty on deployed shape at $\theta = 60^o$of the hinge with w_s = 50 mm (A) LS-Dyna defaults - 'sticky' contact (B) `IGAP` = 2 – 'sticky' contact disabled (C) `SPS` = 0.01 – contact penalty reduced to 1% . . . 73
5.13 Comparison of analytic prediction of dual-matrix hinge fold radius and finite element simulation . . . 74
5.14 Comparison of finite element simulation and experimental results for a hinge with a 50 mm slot . . . 75
5.15 Dependence of deployment moment on the slot length in simulation - implicit model . 76
5.16 Simulated torsional stiffness of hinges with various slot widths . . . 77

6.1 Fiber arrangements used to homogenize composites in finite elements [16] (A) Real fiber arrangement and random RVE (B) Simplified uniform square (left) and hexagonal (right) fiber arrangements . . . 81
6.2 Unit cell model for composite tow with square fiber packing . . . 83
6.3 Unit cell model for plain-weave geometry modified from [17] (A) tow and resin pockets (B) full unit cell model with warp tows in yellow and weft tows in red . . . 85
6.4 Tow elastic constants as a function of tow fiber volume fraction for the AQ/epoxy composite – uniform finite element RVE and analytic predictions from Equation 6.3 . . . 88
6.5 Tow elastic constants as a function of tow fiber volume fraction – uniform finite element RVE and analytic predictions from Equation 6.3 . . . 89
6.6 Dependence of weave stiffness of a single ply on tow elastic constants – AQ/epoxy composite . . . 92
6.7 Dependence of weave stiffness of a single ply on tow elastic constants – AQ/silicone composite . . . 93
6.8 Sensitivity of the ABD matrix of a single ply of AQ/epoxy composite to the finite element weave geometry ($\xi_{E_2} = \xi_{G_{23}} = 2; \xi_{G_{12}} = 1$) . . . 95
6.9 Sensitivity of the ABD matrix of a single ply of AQ/silicone composite to the finite element weave geometry ($\xi_{E_2} = \xi_{G_{23}} = 2; \xi_{G_{12}} = 1$) . . . 96
6.10 Sensitivity of the ABD matrix of a single ply of AQ/silicone composite to the finite element weave geometry ($\xi_{E_2} = 1 \times 10^4; \xi_{G_{23}} = 1 \times 10^3; \xi_{G_{12}} = 1$) . . . 97
6.11 Sensitivity of the extensional and bending stiffness of AQ/epoxy laminates to the finite element weave geometry ($\xi_{E_2} = \xi_{G_{23}} = 2; \xi_{G_{12}} = 1$) (A) $[0_3]_{pw}$ (B) $[45_3]_{pw}$ . . . 98
6.12 Sensitivity of the extensional and bending stiffness of AQ/silicone laminates to the finite element weave geometry ($\xi_{E_2} = \xi_{G_{23}} = 2; \xi_{G_{12}} = 1$) (A) $[0_3]_{pw}$ (B) $[45_3]_{pw}$ . . . 98
6.13 Sensitivity of the ABD matrix of a single ply of AQ/epoxy composite to the composite and tow fiber volume fractions . . . 99
6.14 Sensitivity of the ABD matrix of a single ply of AQ/silicone composite to the composite and tow fiber volume fractions . . . 100
6.15 Schematic of the plain-weave stiffness optimization . . . 102

7.1 Creep test data for neat silicone samples . . . 110
7.2 Shift factors for silicone and WLF fit . . . 110
7.3 Prony series fit of silicone viscoelastic moduli (A) creep compliance (B) relaxation modulus . . . 111
7.4 Relaxation modulus of PMT-F4 epoxy resin, reproduced from [17] . . . 112

7.5 Finite element prediction of tow relaxation moduli (A) AQ/epoxy composite (B) AQ/silicone composite 113
7.6 Finite element prediction of time-dependent ABD stiffness for $[0]_{pw}$ (A) AQ/epoxy composite (B) AQ/silicone composite 114
7.7 Finite element prediction of D_{11} relaxation for $[45_3]_{pw}$ layup and comparison with experimental measurements (A) AQ/epoxy composite (B) AQ/silicone composite . . . 115

List of Tables

2.1 Summary of antenna and deployment architectures © 2017 IEEE 13
2.2 Design and optimization spaces for UHF case study © 2017 IEEE 18
2.3 Initial design and optimization spaces for Ka band case study 21

3.1 Antenna geometries in parametric study 28
3.2 Summary of key performance metrics for antenna geometries in parametric study . . . 28
3.3 Correlation observed between antenna position and performance metrics 29
3.4 Summary of vibration frequencies of antenna for unfolded and folded hinges 34
3.5 Experimentally measured natural frequencies of antenna prototype 37
3.6 Performance summary of antenna prototype RF and structural metrics 38

4.1 Material properties of Astroquartz II fibers and style 525 fabric [18] 40
4.2 Material properties of epoxy F4-B [19] and silicone LOCTITE 5055 [20] matrices . . . 41
4.3 Material properties of phosphor bronze mesh [21] 41
4.4 Measured matrix moduli as a function of distance from the interface 44
4.5 Measured plain-weave geometry for the AQ/epoxy and AQ/silicone composites 46
4.6 Fiber volume fractions of the AQ/epoxy and AQ/silicone composites 47
4.7 Summary of measured and predicted stiffness for various layups of AQ/epoxy composite 55
4.8 Summary of measured and predicted stiffness for various layups of AQ/silicone composite 56

5.1 Values for hinge geometric parameters, units are mm 60
5.2 Simulation parameters for explicit model 71
5.3 Summary of key values of deployment response of hinge with w_s = 50 mm. 75

6.1 Prediction of ABD stiffness of AQ/epoxy laminates using analytic and uniform RVE approaches 89
6.2 Prediction of ABD stiffness of AQ/silicone laminates using analytic and RVE approaches 90
6.3 Nominal plain-weave finite element geometry of AQ/epoxy and AQ/silicone composites 94
6.4 Optimal solution for optimization problem 103
6.5 Comparison of optimized finite element stiffness with measurements of AQ/epoxy composite 103

6.6 Comparison of optimized finite element stiffness with measurements of AQ/silicone composite . . . 104

7.1 Prony series representation of Loctite 5055 silicone creep compliance and relaxation modulus . . . 111
7.2 Prony series representation of PMT-F4 epoxy relaxation, reproduced from [17] . . . 111
7.3 Prony series representation of AQ/epoxy tow relaxation moduli . . . 113
7.4 Prony series representation of AQ/silicone tow relaxation moduli . . . 113

A.1 Design equations for electromagnetic performance metrics . . . 121
A.2 Design equations for structural performance metrics . . . 122

Chapter 1

Introduction

1.1 Motivation

The recent growth in low-cost access to space through nanosatellites is providing the impetus for increasing the capabilities of these platforms, for example by increasing the onboard power and downlink rates for applications such as Earth imaging. CubeSats are a very popular platform, available as commercial off-the-shelf (COTS) kits in sizes that are multiples of the 1U unit ($10 \times 10 \times 10$ cm^3 cube) (Figure 1.1A). The limited size of CubeSats imposes strict volume limitations on all subsystems, and particularly on low-frequency antennas, which have to be folded within the satellite body and deployed after launch. Common choices for CubeSat antennas are the monopole/dipole antenna and the non-deployable patch antenna, which are both available commercially (Figure 1.1B and C). However, the dipole/monopole antennas cannot meet the bandwidth and gain requirements imposed by high bit-rate applications and the patch antenna is of limited application as its size grows prohibitively large at the UHF frequency typically used by amateur CubeSats.

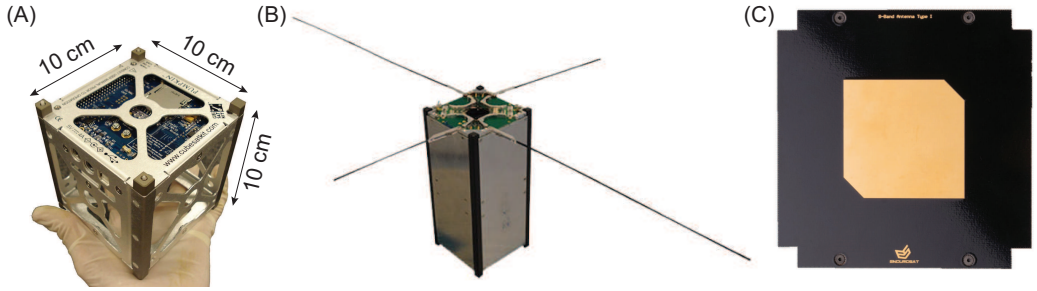

Figure 1.1: (A) 1U CubeSat unit [1] (B) COTS CubeSat dipole antenna [2] (C) COTS CubeSat patch antenna [3]

As with other deployable space structures, there exist several strategies for realizing deployable antennas both at the conventional satellite and CubeSat scales. One approach is through the use of stiff elements connected by mechanical hinges which are spring-loaded or driven by actuators such as motors. A simple example is a metallic rod used for a monopole antenna deployed via a single

hinge (Figure 1.2A). A more complex example is that of deployable mesh reflector antennas such as those developed by Lockheed Martin, Harris Corporation, and Astro Aerospace [22–24]. These contain a circular truss connected with mechanical hinges that is deployed to tension a set of cables supporting a metallic mesh radiating element (Figure 1.2B). Similarly, the Ultra-Compact Ka-Band Parabolic Deployable Antenna is a mesh reflector that has been developed for CubeSats at the Jet Propulsion Laboratory [5]. It consists of unfolding ribs which tension a metallic mesh when deployed (Figure 1.2C). This approach to deployable structure yields high deployed shape accuracy but may result in designs that are heavy and mechanically complex.

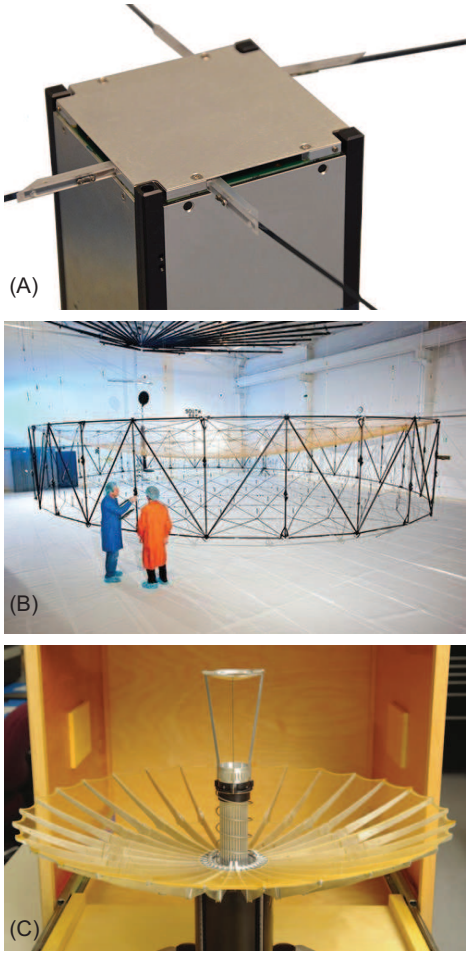

Figure 1.2: (A) CubeSat dipole antenna deployed using a mechanical hinge [2] (B) Astromesh reflector [4] (C) Ultra-compact Ka-band parabolic deployable antenna [5]

An orthogonal approach to deployable antennas is through the use of high-strain thin shell or wire elements, structures which can elastically achieve large configuration changes in order to package and are deployed via stored elastic strain energy. This approach yields lightweight structures without the need for heavy actuators to drive deployment but offers less precise deployed shapes. A simple example is a monopole antenna made of a folded metallic or composite tape spring which

allows the antenna to be wrapped around the satellite and deployed via a burn wire [6, 25] (Figure 1.3A). Furthermore, several designs using high-strain elements have been proposed for deployable helical antennas including the Helios deployable antenna [7] (Figure 1.3B), and a composite helical pantograph [14]. A reflector for a CubeSat where a conductive mesh is supported by coilable ribs has also been proposed by BDS Phantom Works [8] (Figure 1.3C). A deployable Yagi-Uda antenna from bistable tape springs has also been investigated [25]. This approach has also been used on larger satellites as illustrated by the UHF antenna on Skynet [9] (Figure 1.3D) and the spring-back reflector on TDRS [10] (Figure 1.3E).

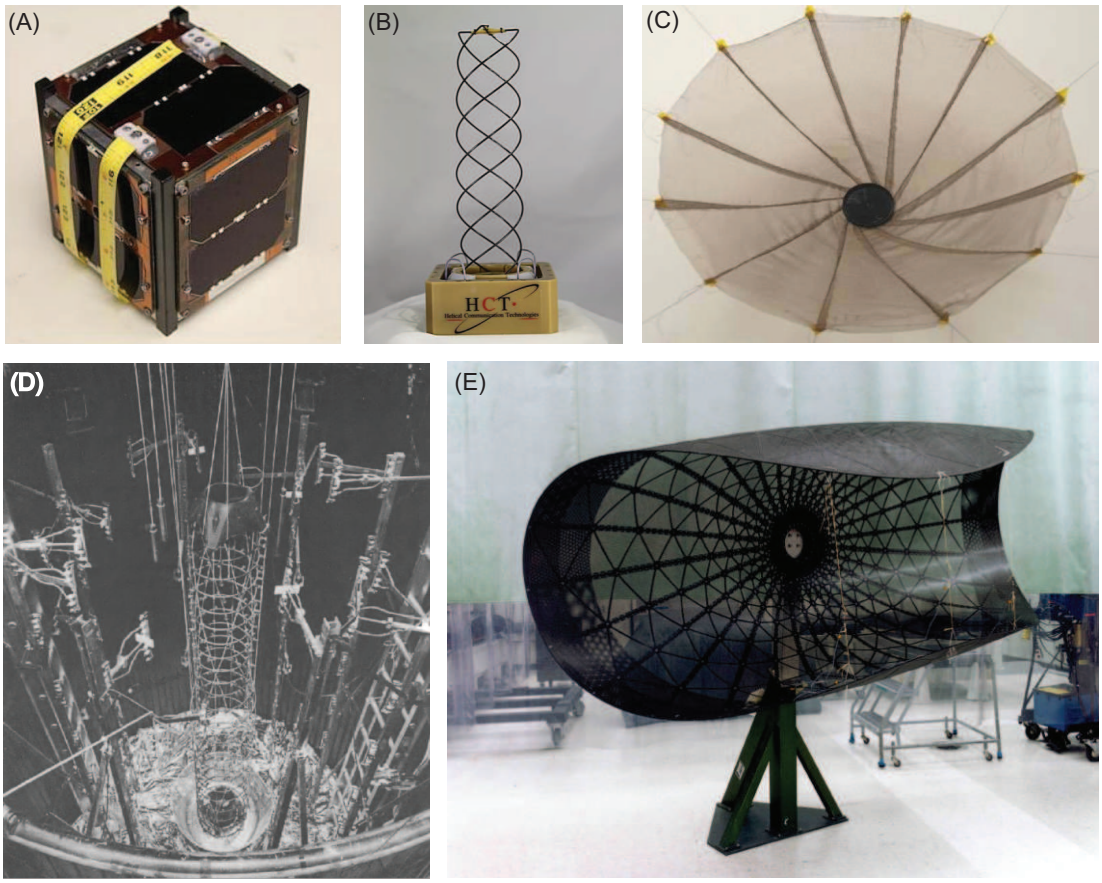

Figure 1.3: (A) CubeSat tape-spring deployable antenna [6] (B) Helios UHF deployable antenna [7] (C) Deployable CubeSat mesh reflector with compliant ribs [8] (D) Skynet 4 UHF antenna [9] (E) Spring back reflector antenna [10]

The packaging achieved using the high-strain element approach is limited by moderate allowable strains of a few percent (e.g., carbon fiber composites can achieve maximum strains of $1 - 1.5\%$ [13]), and so the fold radii of curvature which can be attained are limited. To address this issue researchers have explored elastomer matrix composites which can achieve much higher strains as fibers on the compression side of the fold can elastically microbuckle to avoid failure [11, 26] (Figure 1.4). Elastomer composites have been proposed for application in aerospace structures to realize deployable

reflectors [27] and morphing wings [28]. Their mechanical properties have been studied extensively in [13, 29].

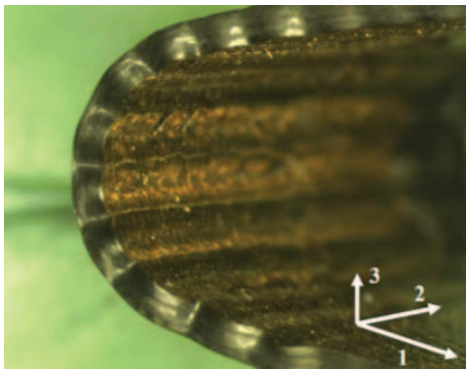

Figure 1.4: Elastic fiber microbuckling on the compression side of a folded elastic memory composite [11]

Elastomer matrix composites have lower than desired stiffness for structural applications, thus researchers at Caltech and L'Garde proposed that they are only used in localized areas where a small fold radius is required to form dual-matrix composites [12, 30, 31]. These are structures with a continuous woven fiber reinforcement, an elastomer matrix in localized hinge regions, and a stiff matrix elsewhere (Figure 1.5A). Combined with an origami folding scheme traced out by the elastomer hinges, these composites can be used to fold structures of complex geometries [12] (Figure 1.5B). A deployable conical antenna made of dual-matrix composites with an embedded metallic mesh conductor has been proposed in [13, 32] (Figure 1.5C). This concept is of interest for use in deployable structures as it can accommodate a variety of antenna topologies. However, studies in literature have been limited to proof-of-concept demonstrations of deployment capabilities [12, 13] and studies of material properties [11, 29, 31]. Little research exists regarding the performance of dual-matrix composites as a structure. Furthermore, modeling has focused on unidirectional composites and hence models for the prediction of the behavior of woven elastomeric composites are limited.

Dual-matrix composites are a promising extension of high-strain composites already used in deployable space structures with potential to achieve improved packaging and enable new antenna concepts. However, there is no easy way to compare their performance to existing designs. A trend with all of the antenna designs mentioned above is that they satisfy only specific mission requirements and cannot easily be scaled to other missions, in particular between large and small satellites. Furthermore, scaling relations between electromagnetic metrics (e.g., antenna gain, bandwidth, polarization) and structural performance (e.g., stiffness, packaging efficiency) are rarely explored making it difficult to adapt existing designs. Typically, when a deployable antenna is designed, its RF performance and packaging schemes are considered as separate design problems which eventually

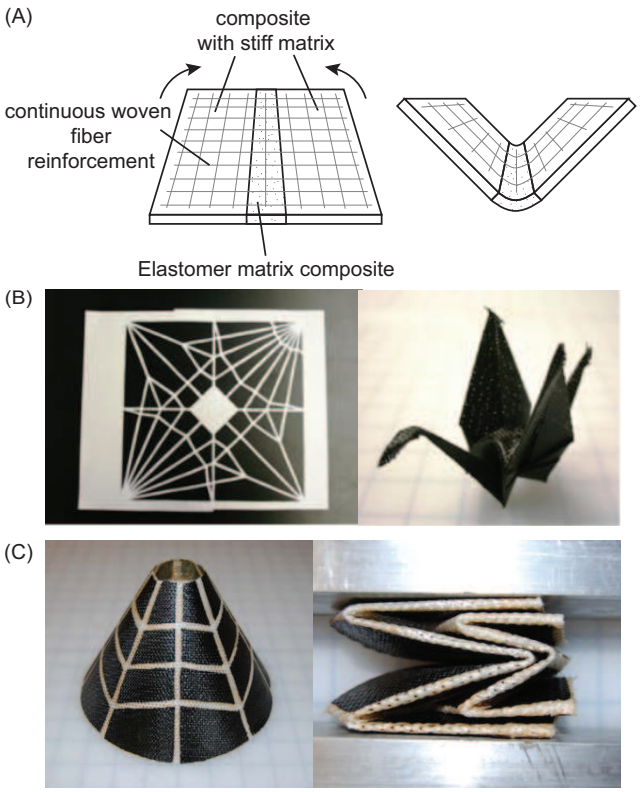

Figure 1.5: (A) Schematic of folding of a dual-matrix composite hinge (B) Folding of an origami crane using carbon fiber composite reinforced with epoxy and silicone [12] (C) Concept for a conical antenna packaged using dual-matrix composites [13]

converge through many design iterations, resulting in lengthy design procedures. Designing simultaneously to meet electromagnetic and structural requirements from the preliminary design stages can save significant cost and will allow new designs to be evaluated quickly through direct comparison to existing solutions.

1.2 Research Goals and Outline

The first objective of this research is to address the existing gap in multidisciplinary antenna design by developing scaling relations between an antenna's physical dimensions and its resulting RF and structural performance. This will allow to scale existing designs across many frequencies of operation and satellite scales. Furthermore, this research aims to use these relations in conjunction with a methodology to compare performance of various designs and select ones meeting RF and mechanical mission requirements simultaneously.

The second objective is the design, fabrication, and testing of a dual-matrix composite antenna for CubeSats. Verification of antenna structural and RF performance is critical to the proposed concept. In particular, an investigation of the effects of folding on antenna performance is of interest.

The third goal is to develop modeling and experimental techniques for studying the quasi-static deployment of dual-matrix composite structures, thus enabling the design of restraint mechanisms for these structures. The simulation of high deformations due to packaging and deployment of thin-shell deployable structures is a particular challenge associated with these techniques. While numerous examples of high-strain composite deployment simulations exist in literature [33–36], techniques are limited to explicit codes resulting in very high simulation times. Furthermore, accounting for fiber microbuckling in the folded configuration is of special interest.

Lastly, this research aims to develop models for woven elastomer composites. Existing analytic models for predicting material properties of woven composites significantly over-predict their stiffness, in particular for bending [37]. Furthermore, existing finite element methods for predicting these properties were tailored to traditional epoxy composites and are not accurate for elastomer matrices [17,35]. Hence, renewed effort is focused on simulation techniques for modeling elastic and viscoelastic properties of soft woven composites to enable the prediction of dual-matrix composite behavior in cases where experimental measurements are time consuming.

This work begins by proposing a methodology for antenna selection and preliminary design in Chapter 2. Existing antenna topologies and packaging schemes are parametrized in terms of their geometry and their performance is predicted using analytic expressions or experimental data. This approach yields a rapid way to predict antenna RF and mechanical performance across a wide set of dimensions. A graphical representation of the data is presented which allows direct comparison to mission requirements and allows one to easily compare concepts to each other and select design which can meet all requirements. Specific designs can be selected for further optimization using traditional finite element techniques. The proposed methodology is demonstrated for the design of two CubeSat antennas, one operating at UHF and one in the Ka-band.

The remainder of the thesis focuses on characterization of a specific deployable dual-matrix antenna selected through the case study in Chapter 2. Chapter 3 describes this design in detail. Follow-on optimization to the preliminary design is presented and its electromagnetic and structural performance is compared to simulated values[1]. It is demonstrated that this multi-functional design can operate both as an antenna and a structure. Furthermore, a design for integration of this antenna into the CubeSat is addressed, including a deployment strategy and antenna feeding.

Chapter 4 provides a summary of the fabrication procedures and material properties of the constituent composites of the antenna. The composites are characterized in tension and bending and results are compared to analytic models. Micrographs are used to investigate the composite micro-structure and the interface between the elastomeric and stiff matrices.

Chapter 5 presents analytic and simulation techniques for modeling the quasi-static deployment of dual-matrix structures. The specific case of a dual-matrix hinge used to separate the antenna

[1]This work was done in collaboration with Dr. Joseph Costantine at the University of New Mexico

from the satellite is studied using a minimum energy formulation and in the LS-Dyna finite element commercial software. Both explicit and implicit models are presented, and the numerical advantages of each are discussed. The results are compared to an experimental characterization of the structure for model validation.

Chapter 6 presents simulation techniques for modeling the behavior of the woven composites. Application of existing models for woven composites show poor agreement with measurements of the elastomer composites studied here. Homogenization techniques in Abaqus are adapted from existing literature and a novel homogenization technique for the woven composite tows is presented to account for the elastomer resin. Chapter 7 extends the proposed models for woven composites to prediction of viscoelastic properties. Master curves for the constituent matrices are constructed and used to predict the homogenized viscoelastic ABD stiffness matrix of the composites.

Finally, Chapter 8 concludes the work and discusses future research directions.

Chapter 2

Rapid Design of Deployable Antennas for Small Satellites

Sections 2.3, 2.4, and 2.5.1 have been reprinted with permission, from:
M. Sakovsky, S. Pellegrino, J. Costantine, *Rapid Design of Deployable Antennas for CubeSats*, IEEE Antennas and Propagation Magazine, DOI: 10.1109/MAP.2017.2655531, April 2017.

2.1 Introduction

In general, the design of deployable antennas requires optimization of performance subject to both electromagnetic and structural constraints. The estimation of electromagnetic performance is usually carried out with numerical simulators, such as Ansys Electronics Desktop [38], CST [39], and Feko [40]. Designer interfaces including a catalog of various antenna structures have been added to several simulation tools, such as the Antenna Magus tool [41], an add-on interface to CST and Feko, and the Ansys HFSS Antenna Design Kit [38]. Even with these aids, electromagnetic performance optimization and concept comparison must still be carried out manually.

Structural simulations are also necessary, usually carried out with finite element software such as Abaqus [42]. In the structures and materials community, existing databases of material properties allow mechanical engineers to quickly compare material performance. An example is the CES selector which compares materials by graphically representing their performance according to different metrics [43, 44]. However, no existing tools consider deployment concepts, which is a parameter critical to the present application. Furthermore, considering electromagnetic and structural requirements separately results in many iterations to complete the design.

These research gaps are the focus of the first research objective outlined in Section 1.2 and are addressed here through a novel methodology for coupled electromagnetic and structural design of deployable antennas, for the specific case of CubeSats. A technique for graphical representation

of antenna performance as a function of geometry using a set of two-dimensional plots is proposed which allows many antenna concepts to be directly compared. These plots allow designers to quickly narrow down the design space to antenna geometries that meet all requirements.

This methodology can be used to evaluate the performance of the proposed dual-matrix antenna concept relative to existing designs to demonstrate dual-matrix composites' ability to achieve efficient packaging, high stiffness, and good antenna performance.

2.2 Overview of Antenna Performance Metrics

Antennas capable of downlinking high amounts of data are desired for CubeSats to keep up with ambitious mission requirements. A 2D slice of a generic antenna radiation pattern is shown in Figure 2.1 to illustrate the parameters of interest to high-performance antennas. An isotropic antenna will distribute the radiated power equally in all directions. However, most antennas deviate from this behavior with power radiated directionally in lobes. A high performance antenna will typically have one narrow main lobe, with a good design minimizing side lobes, in order to achieve a high gain.

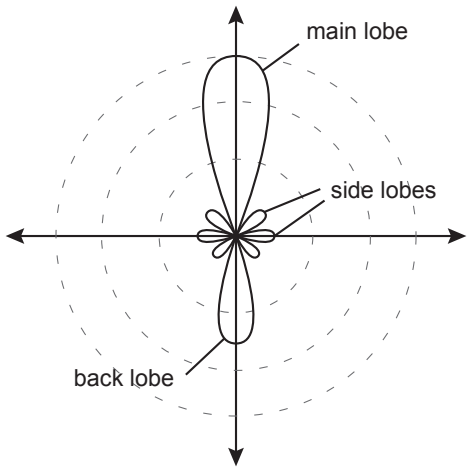

Figure 2.1: Generic antenna radiation pattern 2D slice

Another parameter of importance to maximizing bit rates is a high bandwidth – the range of frequencies over which the antenna is matched. This value is expressed as the fractional bandwidth given by,

$$BW = \frac{f_h - f_l}{f_c} \tag{2.1}$$

where f_h, f_l, f_c are the highest, lowest, and center frequencies of operation, respectively. The impedance matching of an antenna is measured using its reflection coefficient, s_{11}, which is a measure of how much power gets reflected at the antenna feed. The reflection coefficient can be computed as

follows,

$$s_{11} = \frac{Z_L - Z_0}{Z_L + Z_0} \tag{2.2}$$

where Z_0 is the characteristic impedance of the transmission line used to feed the antenna and Z_L is the antenna impedance. A general guideline is to achieve $s_{11} < -10$ dB to result in acceptable matching.

Finally, polarization is a parameter critical to CubeSat antennas. Antenna polarization is a measure of the direction of its electric field. To minimize losses during transmission the polarizations at the satellite end and the ground station should match. However, as CubeSats often have low pointing accuracy, it is advantageous to instead select an antenna with circular polarization to minimize losses.

2.3 Design Methodology

The proposed rapid design methodology consists of the following steps:

1. Identifying a set of antenna topologies relevant to the particular application of interest.
2. For each antenna type, identifying one or more structural architectures and packaging schemes.
3. Obtaining, for each antenna concept, design relationships between the geometry of the antenna and corresponding electromagnetic and structural performance parameters.
4. Generating graphical representations of the design space, through plots of each geometric design parameter vs. all performance parameters, including all considered antenna concepts.
5. Searching for a range of geometric design parameters that allows all requirements to be met, for each of the selected antenna concepts.

This methodology is presented for the specific case of antenna types and packaging schemes proposed for CubeSats, but can be extended beyond this application.

2.3.1 Antenna Types

The antenna types selected for demonstrating the methodology are schematically shown in Figure 2.2. The half-wavelength dipole has been selected for performance comparison, as it is already a widely used antenna on CubeSats [2,6] and can be considered as the fundamental antenna. The fixed patch antenna is a non-deployable reference also available commercially [3]. The helical and conical log spiral (CLS) antennas have been identified as potential concepts for CubeSats in [7,14] and exhibit

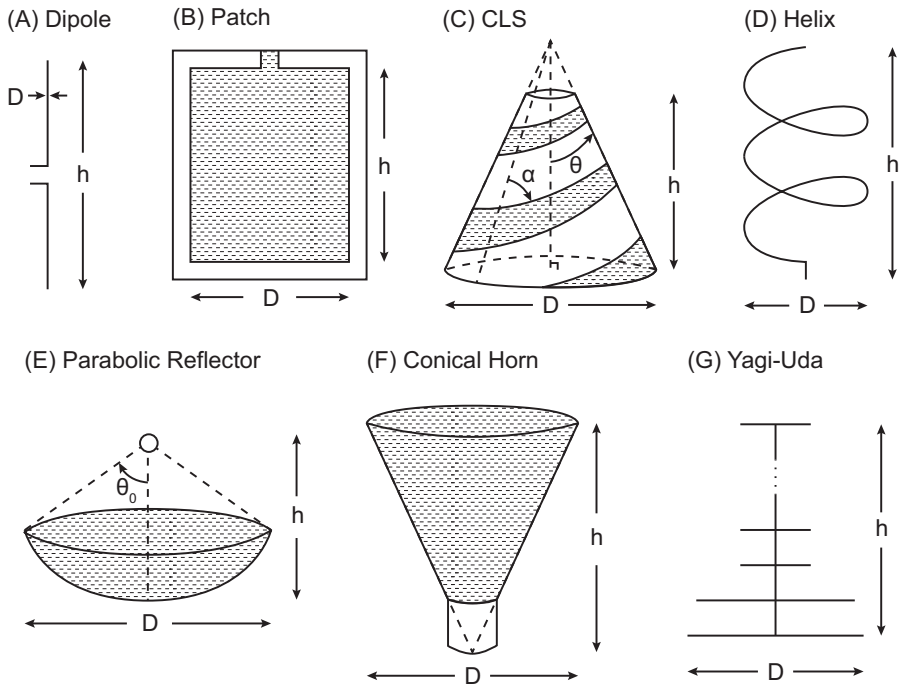

Figure 2.2: Geometry of antennas chosen for the present study

good electromagnetic and structural performance as shown in [13, 15]. The conical horn and Yagi-Uda antennas have been chosen for operation beyond the UHF frequency bands typically used on amateur CubeSats [45].

The space for the antenna design problem is defined here as the set of antenna geometries that result in acceptable electromagnetic performance at the desired operating wavelength, λ. Constraints on the design space are written as a function of antenna height, h, and diameter, D, as defined in Figure 2.2 for each antenna in this study. For the half-wavelength dipole, there is a unique design for each wavelength, λ, with the height, h, given by,

$$h = \frac{\lambda}{2} \tag{2.3}$$

The length of the dipole is referred to here as the dipole height, for consistency with other antenna types.

For the patch antenna, operation as a broad-side radiator requires that,

$$\{0.003\lambda < t < 0.05\lambda\} \cap \left\{\frac{\lambda}{3} < h < \frac{\lambda}{2}\right\} \tag{2.4}$$

where t is the patch thickness. Equivalent constraints on D result in a more complex expression.

For the CLS there are no explicit equations that define the range of acceptable geometries. Hence, the experimental data in [46], presented in terms of the cone angle, θ, and wrap angle of

the conductors around the cone, α, is used. Typical constraints on these parameters, to achieve a directional radiation pattern, are,

$$\{2^\circ < 2\theta < 45^\circ\} \cap \{45^\circ < \alpha < 90^\circ\} \tag{2.5}$$

Given θ and α, the upper and lower radii of the cone, and its height can then be interpolated from experimental data.

Constraints for the helix are derived from desired operation in the end-fire mode with circular polarization [47]. Operation at a given wavelength depends on the diameter, conductor pitch, and number of turns of the helix, which can be re-expressed in terms of the diameter and height only,

$$\left\{D = \frac{\lambda}{\pi}\right\} \cap \left\{\frac{3\lambda}{4}\tan 12^\circ < h < 20\lambda \tan 14^\circ\right\} \tag{2.6}$$

Geometries for the conical horn antenna and the parabolic reflector are defined to minimize antenna losses [47]. For the horn,

$$\left\{\tan 5^\circ < \frac{D}{2h} < \tan 30^\circ\right\} \cap \left\{h^2 = \left(\frac{D^2}{3\lambda}\right)^2 - \left(\frac{D}{2}\right)^2\right\} \tag{2.7}$$

For the reflector,

$$\{0.65 < \epsilon_{ap} < 0.80\} \cap \{2\lambda < D < 50\lambda\} \tag{2.8}$$

where ϵ_{ap} is the aperture efficiency, used here as explicit constraints on reflector height are too complex.

Finally, to achieve a directional radiation pattern, the Yagi-Uda array is typically designed such that [48],

$$\{0.45\lambda < D < 0.49\lambda\} \cap \{0.3\lambda < h < 6\lambda\} \tag{2.9}$$

2.3.2 Structural Architectures and Packaging Schemes

Structural architectures that allow efficient packaging exist for all of the above antennas as described in Section 1.1. Here, we focus on several schemes developed specifically for CubeSats in order to demonstrate the methodology. A simple architecture, suitable for the dipole antenna, is a *single mechanical hinge* supporting a stiff conducting element (Figure 2.3(A)). The hinge allows the conducting element to be folded parallel to the wall of the CubeSat. A simpler and popular alternative is the *metallic tape-spring* (i.e., a structure similar to a tape measure) that is elastically bent near the root to fold the rest of the tape spring parallel to the CubeSat, as in [25] (Figure 2.3(B)). Tape springs can also be used to fold linear arrays including Yagi-Uda antennas [49].

A more complex architecture, suitable for the helix antenna, is a cylindrical lattice of non-

conducting structural helices connected to conducting helices by scissor joints. This structure behaves as a *helical pantograph* [14], and hence has a soft deformation mode that allows axial compaction (Figure 2.3(C)). Alternatively, helical conductors can be supported at the base and compacted axially via rotation, resulting in *coiling of the conductors* around the base, as in [7, 50] (Figure 2.3(D)). Another approach uses *dual-matrix composite shells*, made from laminated thin sheets of continuous quartz fibers embedded in two different plastic materials – a stiff epoxy resin and a soft elastomer – that support a set of embedded conducting elements [15]. The regions with soft elastomer matrix form hinges arranged according to an origami fold pattern that allows the shells to be folded tightly without damaging the fibers. Compaction in a single direction can be achieved using the *z-folding* pattern (Figure 2.3(E)) and compaction in two directions using the *Miura-Ori* origami pattern.

Parabolic reflector antennas require unique packaging schemes due to the doubly curved surface of the main dish. Typically these consist of a mesh conductor shaped by supporting curved ribs. The ribs can be *rigid with several hinges* allowing them to fold alongside a central hub supporting the antenna feed (Figure 2.3(F)) [5]. Alternatively, the ribs can be elastic, allowing the *mesh to wrap* around the central hub using an origami packaging scheme (Figure 2.3(G)) [8].

Table 2.1 summarizes the antenna concepts used in the present study.

	Hinge	Tape-springs	Helical Pantographs	Z-Folded Shells	Miura-Ori Shells	Coilable Conductors	Hinged Ribs	Wrapped Mesh
Dipole	X	X						
Helix			X	X	X	X		
CLS				X	X			
Horn				X	X			
Patch								
Reflector							X	X
Yagi-Uda		X						

Table 2.1: Summary of antenna and deployment architectures © 2017 IEEE

2.3.3 Predicting Antenna Performance

Having parametrized the geometry of the chosen antennas in terms of two common parameters, h and D, the performance of each antenna can be predicted. The electromagnetic performance is characterized by three metrics, as described in Section 2.2: maximum antenna gain, fractional bandwidth, and polarization. These metrics can be computed from analytic equations [47] and

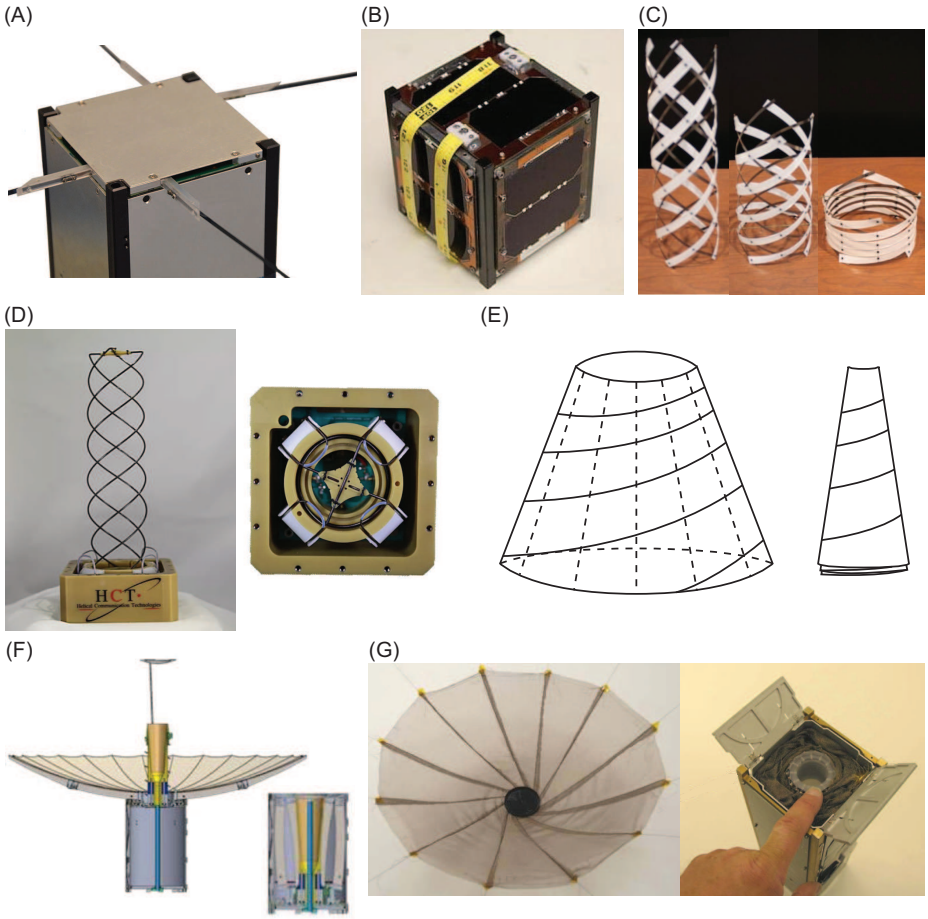

Figure 2.3: Packaging schemes for CubeSat antennas (A) Dipole packaged using mechanical hinge [2] (B) Dipole packaged using tape springs [6] (C) Helix packaged using helical pantograph [14] (D) Helix packaged using coilable conductors [7] (E) CLS packaged using dual-matrix composite shell [15] (F) Reflector packaged using hinged ribs [5] (F) Reflector packaged using mesh wrapping [8]

experimental data [46]. The fractional bandwidth for the horn is derived from the performance range of commercially available antennas. The results are summarized in Table A.1 in Appendix A.

It is important to note that the electromagnetic performance of the chosen antennas depends also on non-geometric parameters, including material properties, feeding technique, and various other factors. However, in an initial design it is acceptable to predict performance based only on geometry; making specific, although preliminary, assumptions about these various effects is sufficient.

The key metric for structural performance of a deployable antenna is its ability to achieve and maintain its deployed configuration, which is best captured by the stiffness of the deployed structure in its softest mode of deformation. The fundamental frequency of vibration in the deployed configuration captures this effect and hence is a key design metric. Furthermore, the packaging performance associated with a given folding scheme, is characterized by the dimensions of the envelope of the folded structure. In addition, a packaging ratio is introduced to measure the ratio of enclosed

volumes in the deployed and folded configurations.

A summary of the equations used to compute structural performance is presented in Table A.2 in Appendix A. The fundamental frequency of vibration of each antenna has been approximated using analytic equations available in [51]. The packaged lengths and packaging ratios have been derived from [14], or computed directly. The structural metrics depend on the geometry as well as material parameters for which specific assumptions have been made based on existing antenna prototypes. These include the Young's modulus, E, Poisson's ratio, ν, linear/areal density, ρ, the number of panels in the origami packaging schemes, i and j, along the axis and the circumference of the antenna, and the Miura-Ori panel angle, ϕ, the conductor diameter, D_{wire}, and the central hub diameter, D_{hub}.

2.3.4 Plots of Performance Metrics

The design problem is formulated as follows. Given a desired operating frequency for the antenna one calculates the corresponding wavelength. Then a set of n antenna concepts is selected, and m performance metrics of interest are computed for them within nested `for` loops as a function of h and D, as illustrated in Figure 2.4. The limits h_{min}, h_{max}, D_{min}, and D_{max} are computed for each antenna concept using constraints in Section 2.3.1, and the metrics are evaluated using equations in Tables A.1 and A.2. Note that this is a brute-force approach, which can be sped up only through coarser discretization of the range of h and D for each antenna. A more efficient algorithm can be developed in the future to accommodate larger design spaces.

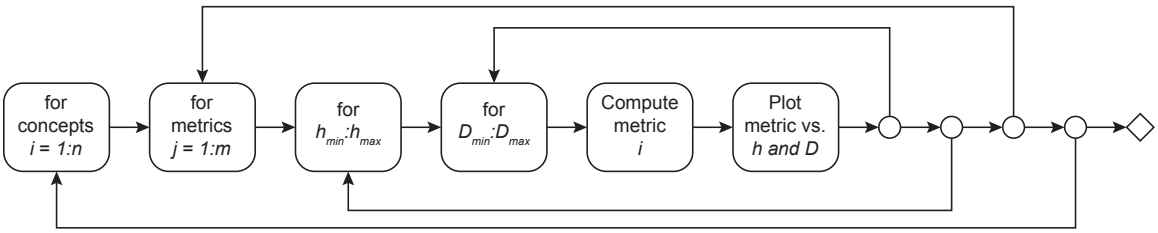

Figure 2.4: Algorithm for estimating antenna performance

The algorithm in Figure 2.4 generates the set of plots following the schematic shown in Figure 2.5; the layout of which is inspired by Ashby's quad-charts [43]. The plots in the top row show the range of each performance metric that can be achieved, for each antenna, by varying the antenna height. Similarly, the plots in the bottom row show the effects of varying the antenna diameter. For each antenna concept, the locus of performance is shown as an ellipse, although the region may be non-convex or disjoint.

Moving across Figure 2.5, the y-axis value remains constant, whereas moving down, the x-axis remains constant. This allows tracking a particular design of a chosen antenna across the whole chart, as illustrated by means of red stars in Figure 2.5. In each plot, shaded rectangles identify the

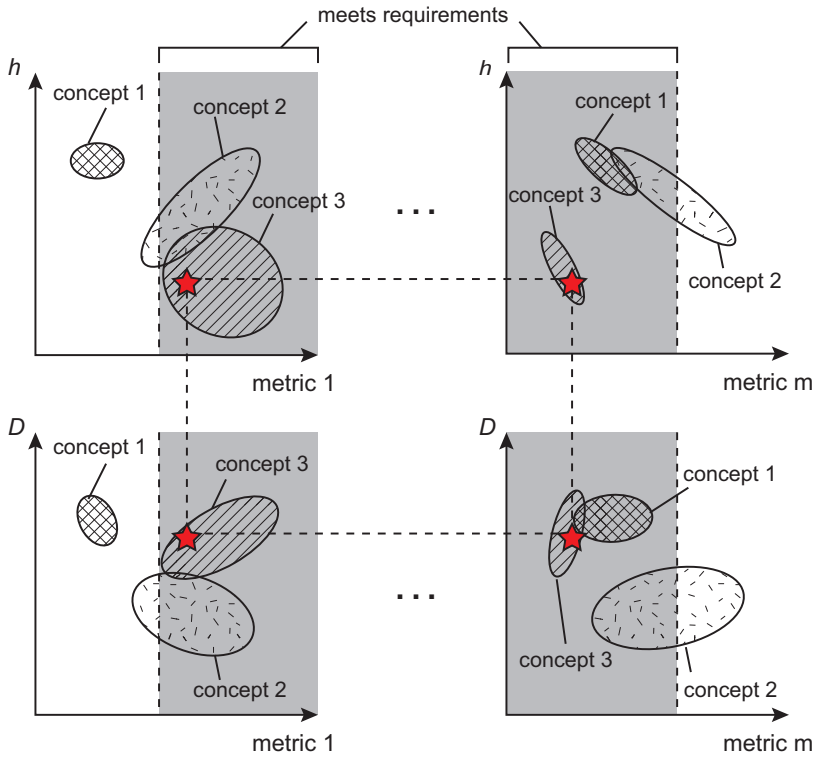

Figure 2.5: Schematic of design charts for comparing antenna performance

region of antenna performance that satisfies requirements prescribed for that metric. Those parts of the elliptical loci that lie within the shaded region represent design geometries that satisfy the requirements for that metric. By looking across several plots, as well as up and down, designers can find subsets of the design space that meet the requirements on all metrics. Thus, the final result is a set of antenna geometries, parameterized in terms of h and D, that are capable of meeting all requirements. This set can be used for a follow-on, detailed optimization. Furthermore, the design charts can be used to compare the performance of various antenna concepts to each other across a wide range of metrics.

2.4 Preliminary Design Tool

A design interface has been developed in order to implement the proposed methodology in Matlab. The tool allows one to enter the requirements for the design problem and the antenna concepts to be compared, as shown in Figure 2.6, and automatically generates a design chart. The user can compare different antenna types or a single antenna packaged using several schemes, for an arbitrary number of parameters. The tool allows designers to select and compare various antenna topologies against multiple deployment approaches, before selecting an optimal solution that will then be modeled using any of the numerical simulators available for detailed radiation characteristic

and electromagnetic performance evaluation. Thus, the tool reduces the selection and comparison time in the preliminary design stages.

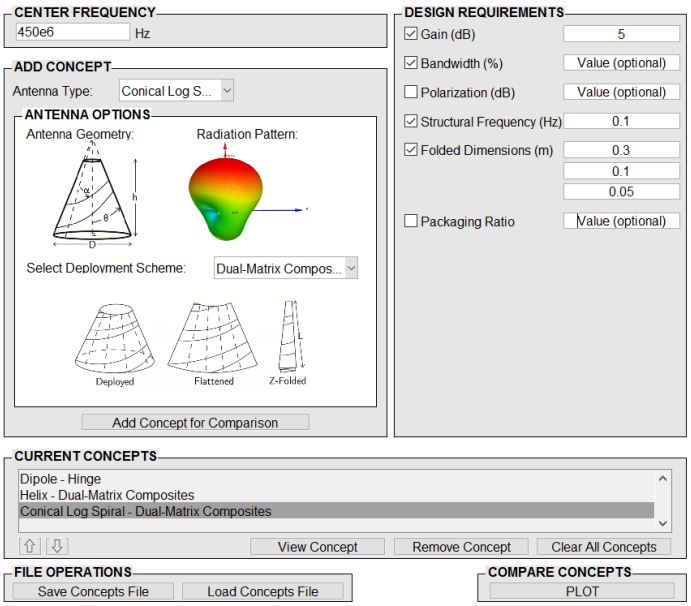

Figure 2.6: Concept selection tool input screen © 2017 IEEE

2.5 Case Studies

Several case studies of the design of deployable CubeSat antennas are presented here to demonstrate the advantages of the proposed methodology.

2.5.1 UHF Antenna Design

A case study of a UHF antenna operating at 450 MHz is presented to demonstrate the methodology. Furthermore, this case study is used to compare the performance of several concepts packaged using dual-matrix composites against COTS antennas. The antenna concepts compared are:

1. Dipole packaged using a mechanical hinge
2. Helix packaged using coiling of conductors
3. CLS packaged using z-folding of dual-matrix shells
4. Horn packaged using z-folding of dual-matrix shells

The following requirements are prescribed on the design:

1. Gain in excess of 5 dB

2. Fundamental structural frequency higher than 0.1 Hz

3. Packaged antenna fitting in a $\frac{1}{2}$ 3U CubeSat volume ($30 \times 10 \times 5$ cm^3)

4. Maximized bandwidth

The requirements define a coupled electromagnetic and structural design problem appropriate for the methodology presented above. The geometric constraints on height and diameter are calculated from Equations 2.3, 2.6, 2.7, and 2.5, respectively, for the four antennas and are given in column 2 of Table 2.2. The gain, fractional bandwidth, fundamental frequency, and packaged dimensions are computed from the equations in Tables A.1 and A.2 for this range of geometric parameters. These metrics are plotted against the antenna geometry as described in Section 2.3.4 and the result is shown in Figure 2.7.

Concept	Original Design Space (m)	Optimization Space (m)
Dipole	$h = 0.33$ and $D = 0.025$	Does not meet requirements
Single Helix	$0.012 < h < 3.32$ and $D = 0.21$	$0.22 < h < 0.27$ and $D = 0.21$
Conical Horn	$1.73 < h < 65.53$ and $2.00 < D < 11.47$	Does not meet requirements
CLS	$0.18 < h < 23.40$ and $0.13 < D < 2.27$	$0.18 < h < 0.27$ and $0.20 < D < 0.30$

Table 2.2: Design and optimization spaces for UHF case study © 2017 IEEE

To select specific antenna architectures that meet all requirements, one starts from plot A1, top-left in Figure 2.7. This plot identifies designs meeting the gain requirement; hence the region with gain higher than 5 dB (3.16 dimensionless) is shaded gray in the plot. The locus for the dipole antenna (which is a single point) falls outside the shaded area, indicating that it does not meet the gain requirement. Note also that the entire locus for the conical horn antenna falls inside the shaded area, hence it meets the gain requirement. Regarding the loci for the single helix and the CLS, only subsets fall within the shaded area. The height ranges corresponding to these subsets identify viable CLS antennas, with any height, and helical antennas with $0.22 < h < 3.32$ m.

Moving to the right from plot A1, the same process can be repeated for plots A2–6. Plot A2 imposes no new constraints on the design as no requirement is specified for the bandwidth. However, it can be seen that the CLS maximizes the fractional bandwidth. In plot A3, it is found that only conical horn antenna heights in the range $1.4 < h < 3.2$ m meet the structural frequency requirement, whereas there is no limitation on the helical and CLS antennas. Proceeding to plot A4, introducing a constraint on the largest packaged length of 0.3 m, eliminates the conical horn antenna (indicating that the chosen packaging scheme is not acceptable). Of the remaining two viable concepts, the length requirement is met by helical antennas with $0.012 < h < 0.27$ m and CLS antennas with $0.18 < h < 0.27$ m. Similarly plot A5 imposes that $0.18 < h < 10.0$ m for the CLS. No additional

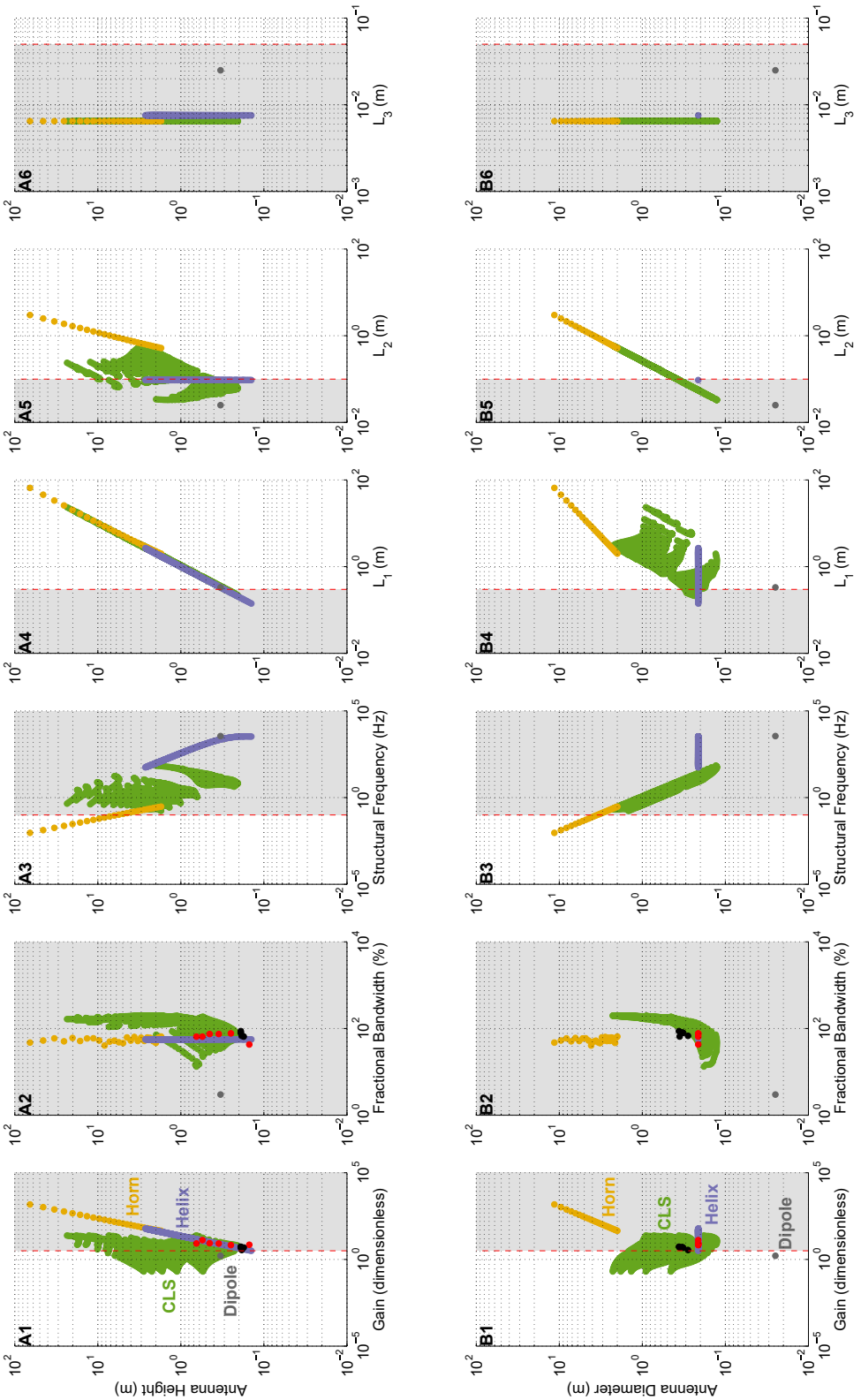

Figure 2.7: Concept selection chart for the design of a high performance UHF antenna operating at 450 MHz that folds in a 3U CubeSat. The red and black dots indicate helix and CLS antenna performance, respectively, designed using numerical simulations © 2017 IEEE

constraints are given by plot A6.

Analysis of the first row of plots in Figure 2.7 has led to the conclusion that the dipole and conical horn cannot meet all requirements. At this point, an analysis similar to that described above, but using the bottom row of plots in Figure 2.7, provides the range of viable diameters for the helix and CLS. The outcome of the analysis is the h and D ranges meeting all requirements, presented in column 3 of Table 2.2. It can be observed that these ranges are orders of magnitude smaller than the original design space. At this point detailed simulations can be carried out to complete the design optimization.

Antenna designs generated independently via numerical simulations in ANSYS HFSS for this case study are denoted by red and black markers in Figure 2.7 for the helix and CLS antennas, respectively. A good agreement is seen between the performance of these and the designs that are proposed by the methodology here.

This case study has demonstrated that dual-matrix composites can enable the packaging of a CLS antenna in small CubeSat volumes, a concept not previously implemented. Furthermore, plots A2 and B2 in Figure 2.7 show that the CLS packaged using dual-matrix composites can achieve higher bandwidths. Therefore, it has been shown that dual-matrix composites can outperform existing concepts and should be studied further.

2.5.2 Ka-Band Case Study

A second case study demonstrating the preliminary design of a deployable antenna operating at 30 GHz (Ka-band) is shown here. The Ka-band has the potential for higher bit rates and smaller antenna sizes and would be appropriate for deep space CubeSats [5]. However, it is also known to be susceptible to rain attenuation and requires higher surface accuracy than antennas designed for the commonly used UHF-band for low earth orbit CubeSats. The case study illustrates the use of the proposed concept selection methodology to explore a new design space and identify constraint satisfying concepts. The antenna concepts compared are:

1. Helix packaged using helical pantographs
2. CLS packaged using z-folding of dual-matrix shells
3. Horn packaged using z-folding of dual-matrix shells
4. Parabolic reflector packaged using hinged ribs

The following constraints are placed on the design:

1. Maximum gain above 20 dB
2. Fundamental frequency higher than 0.1 Hz

3. Packaged antenna fits in a 1/2 1U CubeSat volume ($10 \times 10 \times 5$ cm^3)

4. Design maximizes bandwidth

Following the methodology described in Section 2.3, design space limits are computed using Equations 2.5 – 2.8 and the performance is estimated using Tables A.1 and A.2. The results of the case study are generated using the tool in Section 2.4 and are plotted in Figure 2.8. Starting from the top left corner of the chart (plot A1), one can select antenna heights for each concept which meet the gain requirement (i.e., ones in the shaded region with gain greater than 20 dB). It is evident that the entire loci of performance for both the helix and CLS antennas lie outside this region and hence cannot meet the gain requirements. However, from the performance loci for the horn and reflector one can see that there are designs that achieve the desired gain. In particular, horn antennas with $h > 6.0$ cm and reflectors with $h > 1.1$ cm meet the requirement.

Moving to the right, one can repeat the same process for plots A2–A6, obtaining designs that meet the bandwidth, frequency, and packaged volume requirements. As no quantitative requirement has been specified on the bandwidth, no new constraints can be derived from plot A2. However, out of the remaining concepts, it can be seen that the horn maximizes bandwidth. From plot A3, it is evident that all concepts lie in the shaded region and can meet the fundamental frequency requirements. Plots A4 – A6 show that not all horn and reflector designs can be packaged in the required volume. From plot A4, one can get that $h < 9.5$ cm for the horn and $h < 16.0$ cm for the reflector. Plot A6 imposes a further constraint that $h < 14.5$ cm for the reflector. A similar process is repeated with the bottom row of the chart (plots B1 – B6) to find antenna diameters that meet all requirements. This results is a narrow set of constraint-satisfying geometries as summarized in Table 2.3. The initial design space has been reduced by at least an order of magnitude and the helix and CLS antennas have been ruled out as possible concepts as they cannot meet gain requirements.

Concept	Initial Design Space (cm)	Optimization Space (cm)
Helix	$0.2 < h < 4.0$ and $D = 0.3$	Does not meet requirements
CLS	$0.3 < h < 35.2$ and $0.2 < D < 3.4$	Does not meet requirements
Horn	$2.6 < h < 98.3$ and $3.0 < D < 17.2$	$6.0 < h < 9.5$ and $4.4 < D < 5.4$
Reflector	$0.6 < h < 31.0$ and $2.0 < D < 99.9$	$1.1 < h < 14.5$ and $4.0 < D < 50.0$

Table 2.3: Initial design and optimization spaces for Ka band case study

A horn antenna operating at the Ka-band has not previously been proposed in literature for deployment from CubeSats. However, Figure 2.8 shows that it is a feasible concept for this design problem. The horn has less structural complexity than the reflector but can still achieve very high gains over a good bandwidth.

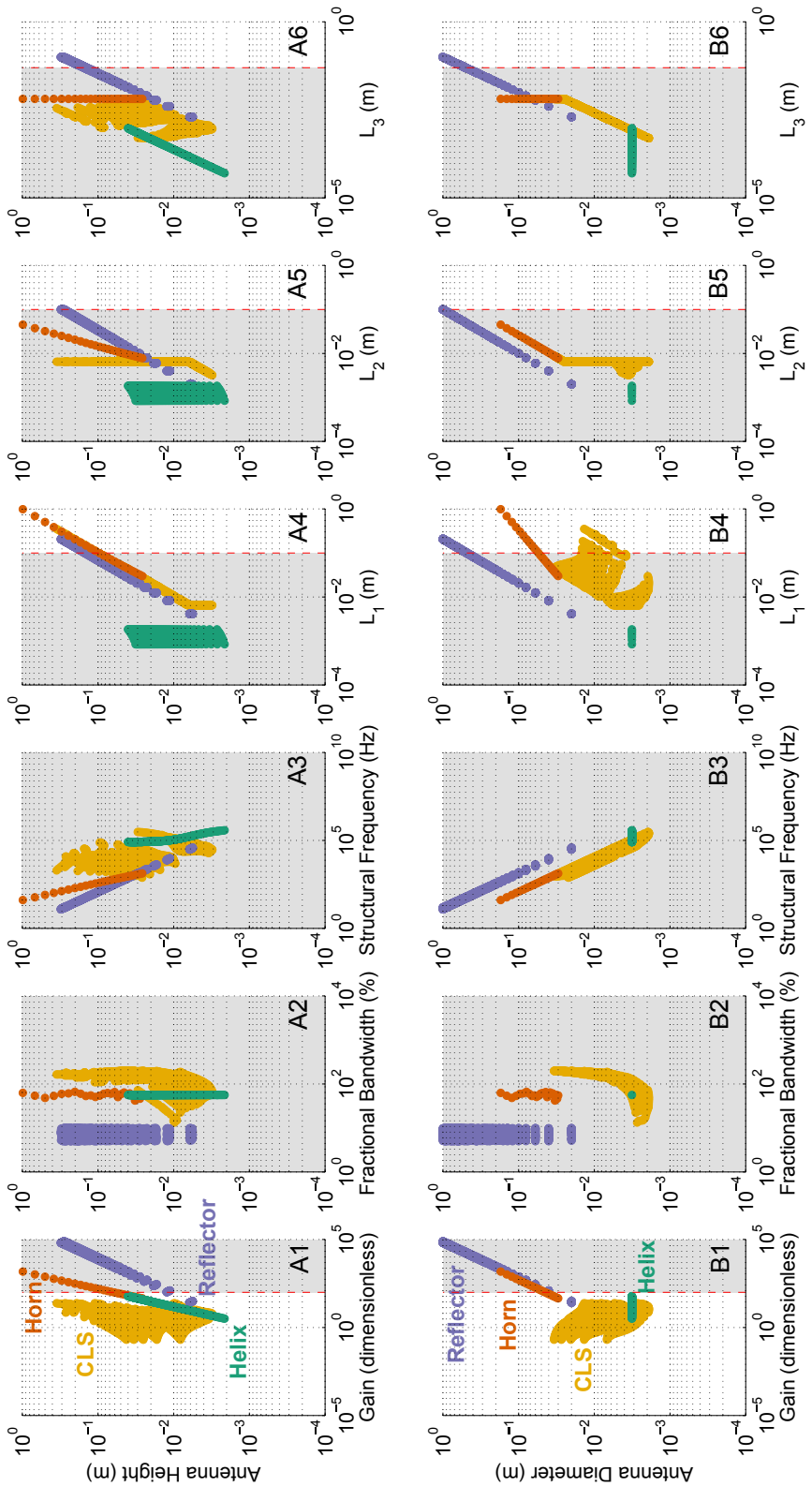

Figure 2.8: Case study at $f = 30$ GHz. From left to right, the plots shows antenna height/diameter as a function of gain, bandwidth, structural frequency, and the packaged antenna dimensions. The shaded regions represent areas of the plots that meet imposed requirements.

The next step in the design would involve detailed numerical simulations of the horn and reflector designs in the optimization space in Table 2.3. This would be a much shorter process than if one started simulations from the initial design space without knowing if a particular concept could meet all requirements.

2.6 Conclusion

A methodology for the rapid preliminary design of deployable antennas for CubeSats aimed at reducing design times of deployable antenna problems was proposed. Using a novel visual representation method of antenna performance consisting of a coordinated set of plots of antenna performance metrics against the antenna geometric parameters, it can easily address coupled electromagnetic and structural design problems. This approach enables direct comparison of antenna concepts and allows the designer to rapidly identify concepts which meet requirements and to narrow down the design space, before tackling the problem with detailed numerical simulations.

The design of an antenna operating at 450 MHz and another operating at 30 GHz is used to demonstrate the method. The technique eliminates antenna designs unable to meet requirements, thus achieving a reduction of the original design space by several orders of magnitude. The results agree well with antenna designs optimized using numerical simulations. Furthermore, this tool is capable of identifying concepts not previously considered for use on CubeSats – the CLS and horn antennas packaged using dual-matrix composites for the UHF and Ka-band, respectively.

The methodology is demonstrated using a relatively small number of antenna types, packaging schemes, and performance metrics. However, the method itself is quite general and can be extended further. For example, an antenna mass performance metric and material selection can be incorporated in the tool. The software tool that has been developed could also be combined with existing databases of antenna and structural performances, to provide rapid comparison over much larger design spaces.

Chapter 3

Dual-Matrix Composite Antenna Prototype

3.1 Introduction

The design strategy devised in the last chapter allowed the preliminary evaluation of dual-matrix composites as a packaging scheme for CubeSat antennas. It was shown that, at least theoretically, these materials can be used to design very high gain, broadband antennas capable of fitting into small CubeSat volumes. Moreover, the versatility of the packaging scheme was demonstrated. Dual-matrix composites can be used to package a variety of antenna topologies – from the helix to the conical horn – and appeared to scale well from one operating frequency (UHF) to another (Ka-band). These are promising results, however, the functionality of a prototype antenna must be verified to validate these results in practice.

To demonstrate functionality, this thesis focuses on a dual-matrix antenna operating at UHF with its design subject to the requirements in the case study in Section 2.5.1. The UHF band was chosen as it is the predominant choice for amateur CubeSats in low Earth orbit. Furthermore, working at higher frequencies would require the fabrication of very small antennas. The UHF case study in the previous chapter identified the CLS as an antenna topology capable of meeting the specified requirements and at the same time maximizing bandwidth over the helix. The design chart in Figure 2.7 placed the following constraints on the CLS geometry such that all requirements are met,

$$0.18 < h_{CLS} < 0.27 \text{ m} \ \cap \ 0.20 < D_{CLS} < 0.30 \text{ m} \tag{3.1}$$

For a more rigorous follow-on analysis to the preliminary design tool, finite element simulations of the antenna performance were done for several designs around this geometry range in order to select an optimal constraint satisfying design. Furthermore, the design of the antenna to CubeSat interface was considered as it affects antenna performance.

In order to validate the dual-matrix approach as applied to the deployable antenna problem, the following chapter demonstrates antenna RF and structural functionality. Furthermore, experimental results are compared to simulations to enhance the accuracy of numerical models to be used for design of such structures in the future. Most importantly, the antenna's capability to meet requirements prior to and after folding and instantaneous deployment is assessed.

3.2 Antenna-CubeSat Assembly

An assembly of the prototype antenna with a 6U CubeSat structure in which it can be stowed is shown in Figure 3.1. The antenna consists of a shell with Astroquartz II (AQ)/epoxy panels and AQ/silicone hinges. The antenna functionality is achieved by embedding a thin phosphor bronze mesh in the composites shell. The composites laminates are made of a 6 ply $[\pm 30/0]_{s,pw}$ layup, where the *pw* subscript indicates that each ply is plain-weave. A detailed overview of material properties is given in Chapter 4. When deployed, the antenna is supported outside of the CubeSat by a dual-matrix hinge (studied in detail in Chapter 5). The feeding network for the antenna is also shown with a balun circuit used to split the 50 Ω input to two 100 Ω feeds attached to the two arms of the antenna. Furthermore, traditional co-axial cables have been replaced by custom-designed flexible microstrip lines to enable folding of the feed cables within the antenna. The feed lines are soldered to the conductors at the apex of the cone and then clamped between 3D printed plastic parts conforming to the curvature of the antenna. Likewise, the antenna is attached to the deployable hinge via screws with curved 3D printed washers.

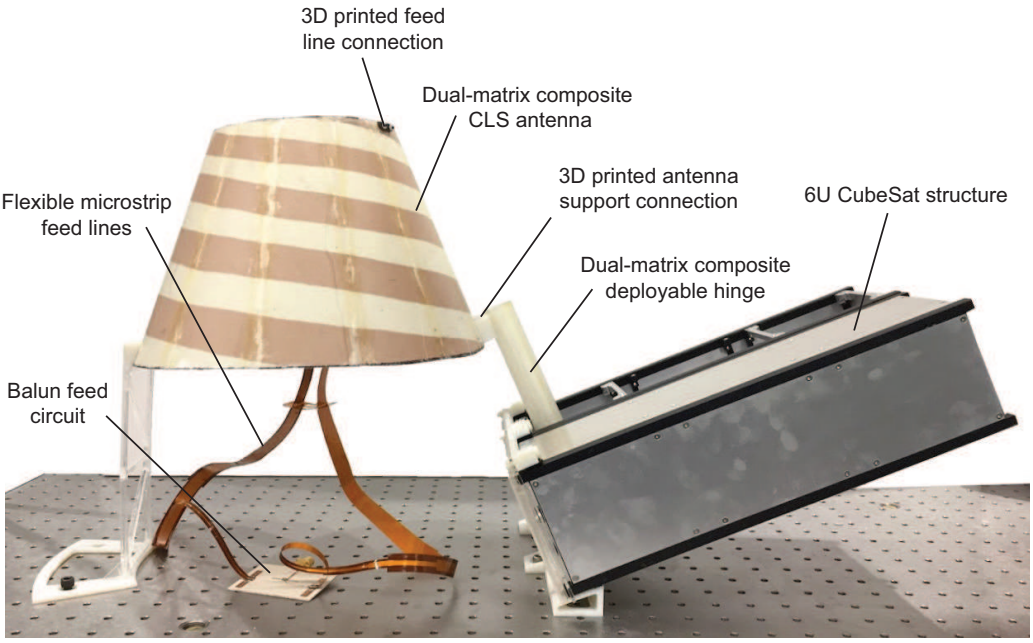

Figure 3.1: CubeSat assembly with deployed antenna and feeding network

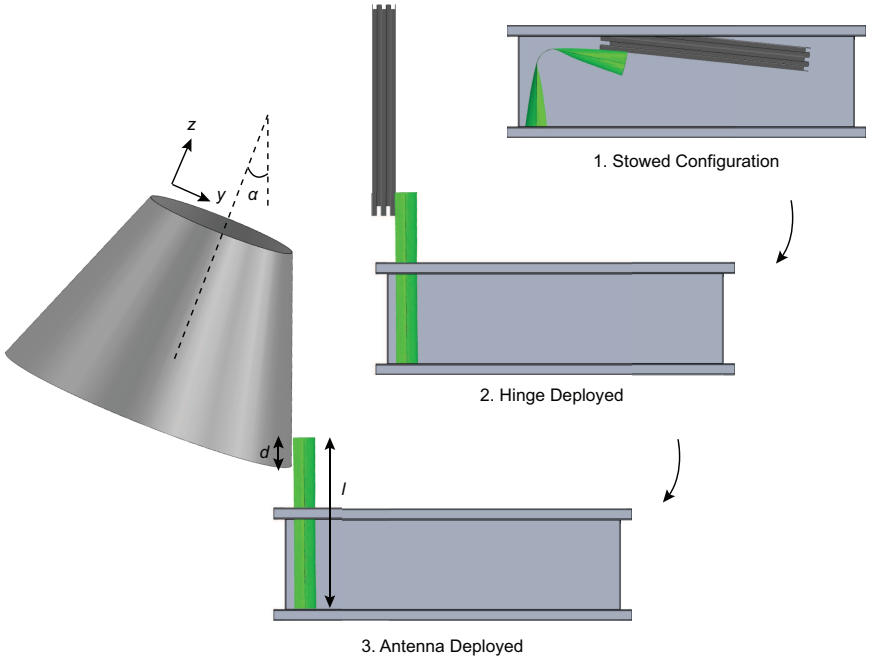

Figure 3.2: Steps in antenna deployment from CubeSat

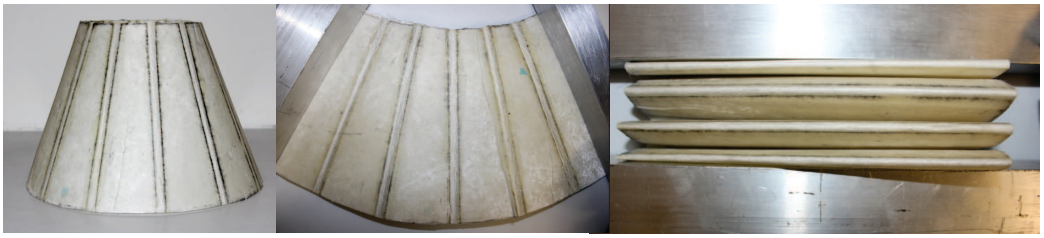

Figure 3.3: Folding of dual-matrix antenna by flattening and z-folding

A schematic illustrating the antenna deployment is shown in Figure 3.2. It can be seen that the antenna deployment has been decoupled from the hinge deployment for simplicity and to improve the reliability of antenna deployment without jamming.

Figure 3.3 shows the folding process of the antenna prototype. The cone is folded using 12 AQ/silicone hinges running along its height. The antenna is first flattened and the z-folded to package inside of the CubeSat.

3.3 Prototype RF Performance

The work in this section was done in collaboration with Dr. Joseph Costantine at the University of New Mexico.

3.3.1 Antenna Geometry Optimization

A parametric study was conducted using the ANSYS HFSS finite element software to optimize antenna performance independent of the CubeSat. The parameters of interest of the CLS geometry are illustrated in Figure 3.4, where h is the height of the cone, D and D_0 are the lower and upper diameters of the cone, respectively, θ is the cone angle, and α is the conductor wrap angle. The CLS antenna has two identical conductors rotated 180^o with respect to the cone central axis. For clarity, only a single conductor is shown in the figure.

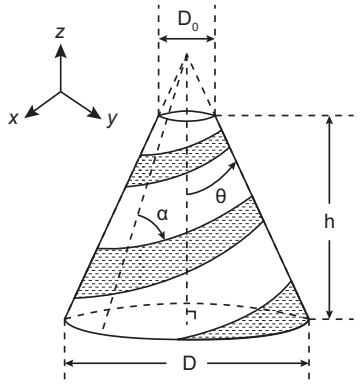

Figure 3.4: Geometry parameters of interest in the design of a CLS antenna

In Chapter 2, the geometry has been parameterized in terms of h and D only, and this is sufficient to describe the geometry. For a given h and D, the upper diameter (or equivalently θ) and conductor wrap angle are selected to minimize loses [46]. The cone geometry and conductor geometry are related by,

$$D = D_0 \exp\left(\frac{\phi}{2\pi} \ln EF\right) \tag{3.2}$$

where $\frac{\phi}{2\pi}$ is the number of conductor turns and the expansion factor for the conductor, EF, is defined as,

$$EF = \exp\left(\frac{2\pi \sin\theta}{\tan\alpha}\right) \tag{3.3}$$

The expansion factor was kept constant in this study at $EF = 1.75$, selected using design data in [46]. A parametric study varying h and D was done independently of the preliminary design given in Section 2.5.1. Table 3.1 summarizes the geometry of a few of the designs considered.

Figure 3.5 shows the variation of the reflection coefficient as well as a slice of the radiation pattern (y-z plane) with the geometry of the antenna. Table 3.2 summarizes the key RF performance metrics for these designs. It can be seen that as the antenna diameter increases for a fixed height, higher gains and bandwidths are seen. This occurs as the antenna becomes more directional and the back lobe is minimized. Antenna design 4 was the final design selected for the prototype as its geometry was within the range given by Equation 3.1 and so the antenna would violate packaging constraints.

Parameter	Antenna 1	Antenna 2	Antenna 3	Antenna 4
h (cm)	19.0	19.0	17.5	18.5
D (cm)	32.2	33.2	35.5	28.2
D_0 (cm)	16.0	16.0	16.0	14.0
$\phi/2\pi$	1.25	1.3	1.5	1.5
s	20.7	20.6	20	19.6

Table 3.1: Antenna geometries in parametric study

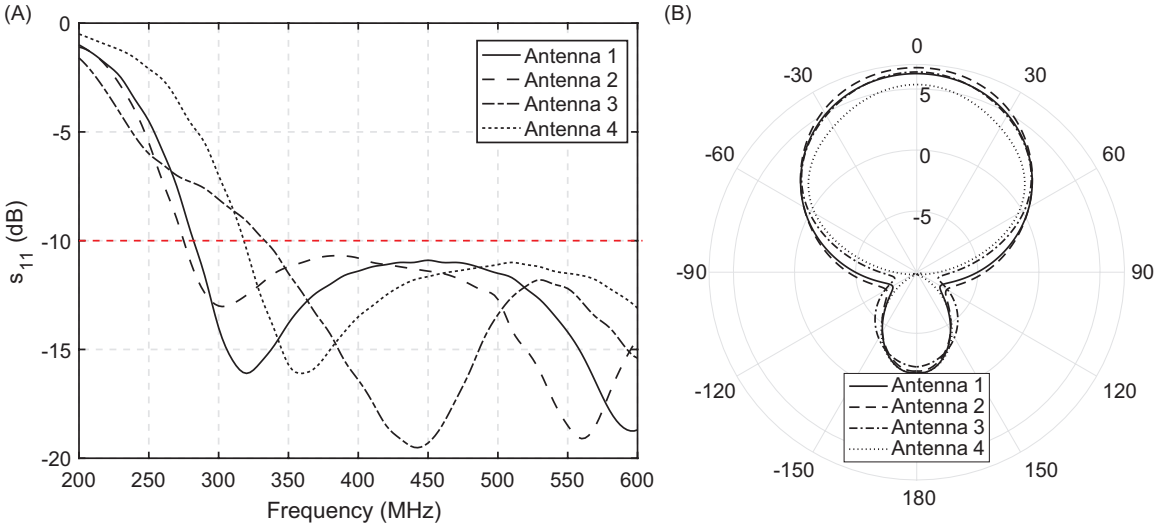

Figure 3.5: (A) Reflection coefficient of select antenna designs (B) Cut in the y-z plane of radiation pattern at 450 MHz

Parameter	Antenna 1	Antenna 2	Antenna 3	Antenna 4
$BW(\%)$	79	81	65	69
G (dB)	6.78	7.15	6.88	5.36

Table 3.2: Summary of key performance metrics for antenna geometries in parametric study

3.3.2 Antenna Position Optimization

Having optimized antenna performance, the interaction of the antenna with the metallic CubeSat was investigated. The following parameters were investigated, illustrated schematically in Figure 3.2, to determine their effects of the antenna gain, backlobe radiation, and axial ratio (a measure of polarization): the angle of the antenna axis with respect to the satellite, α, the overlap length of the antenna and the hinge, d, and the presence of solar panels on the CubeSat. A summary of the variable dependences observed in simulations is shown in Table 3.3.

Using the simulation data a specific design for the interface was selected. An angle of $\alpha = 22^o$

Parameter	Range	Axial Ratio	Gain	Backlobe Radiation
d	2 cm $< d <$ 6 cm	Proportional	Inverse	Inverse
α	$10^o < \alpha < 50^o$	Inverse	Proportional	Inverse
Solar Panels	N/A	Proportional	Inverse	Inverse

Table 3.3: Correlation observed between antenna position and performance metrics

was selected such that the antenna cone generator is parallel to the CubeSat edge. In order to maximize gain and reduce backlobe radiation, an overlap of d = 2 cm was selected. Furthermore, a boom length of l = 20 cm was selected to fit the antenna into the CubeSat.

3.4 Antenna Feeding Network

The feeding network consists of a 50/200 Ω Anaren B0205F50200AHF surface mountable balun, to balance a 50 Ω input into the two arms of the CLS antennas, and two 100 Ω transmission lines. The micrstrip lines have been designed to have 100 Ω impedance over the entire antenna bandwidth. This was achieved by using a Chebishev tapering pattern for the microstrip conductor and ground lines. The geometry of the design is shown in Figure 3.6. The feed lines were manufactured by San Francisco Circuits. A 1 oz. copper conductor was patterned onto both sides of a 125 µm Kapton layer to function as the ground plane and conductive strip. Both sides were then covered by a 25 µm polyimide coverlay to prevent oxidation of the copper.

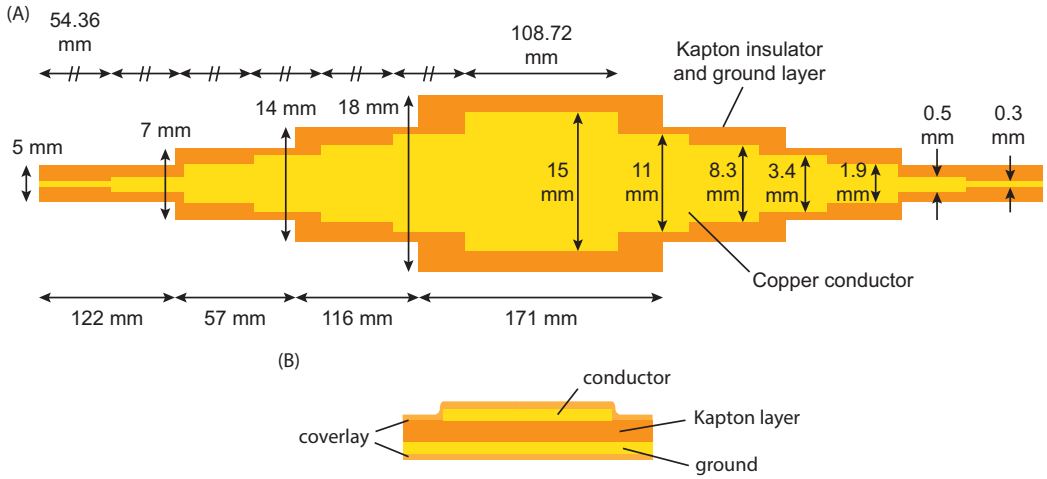

Figure 3.6: Geometry of flexible microstrip lines (A) Chebishev tapering (B) cross-section

The reflection coefficient of both the balun circuit and the flexible feed lines was measured to ensure operation of the feeding network over the antenna bandwidth. The measurements are shown in Figure 3.7. The balun shows good operation with $s_{11} < -10$ dB over the entire antenna bandwidth

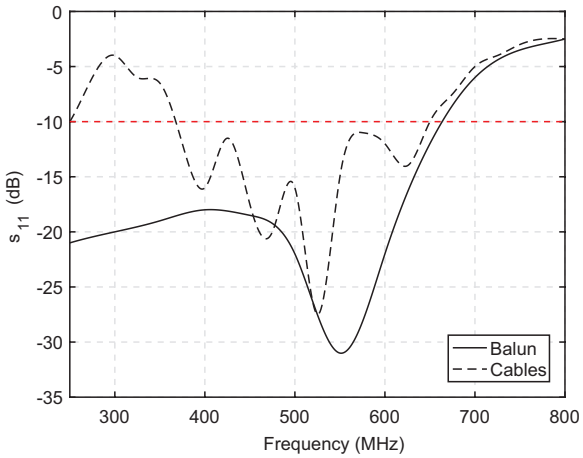

Figure 3.7: Reflection coefficient of feed network

while the cables have a slightly narrower bandwidth of 360 - 650 MHz, and may impede antenna operation at the lower frequencies.

3.4.1 RF Testing

The electromagnetic performance of the antenna prototype was measured at the Antennas and RF Lab facilities at the University of New Mexico. The reflection coefficient was measured using the PNA-X 5247A vector network analyzer from Keysight. Radiation pattern cuts and gain measurements were done in a 5.33×2.59×2.13 m^3 anechoic chamber. A photograph of the CubeSat assembly under test in this chamber is shown in Figure 3.8. Unfortunately, the existing chamber was designed for measurements above 1 GHz and is too small for UHF applications. As a result, the radiation pattern measurements are not entirely in the farfield of the antenna but are sufficient to verify performance with small error.

Figure 3.9 compares the measured reflection coefficient and radiation patterns to those predicted in finite element simulations. When the antenna is fed using co-axial cables, the reflection coefficient shows good agreement with simulations and it can be seen that antenna operation is achieved between 300-650 MHz. No change in s_{11} was observed after folding and deploying the antenna. Also shown is the reflection coefficient when the antenna is fed with the flexible microstrip lines. The reflection coefficient curve is significantly impacted and as predicted antenna operation is lost at lower frequencies. However, the antenna still shows good operation between 354 - 407 MHz and 425 - 650 MHz.

The measured 2D radiation pattern cuts in the y-z plane (measured with co-axial cables) show that the antenna achieves a maximum gain of 5.57 dB at 450 MHz, comparable to the predicted gain of 5.36 dB. Furthermore, Figure 3.9 shows the measured maximum gain as a function of antenna frequency, illustrating that the prototype meets the 5 dB gain requirement across its entire band-

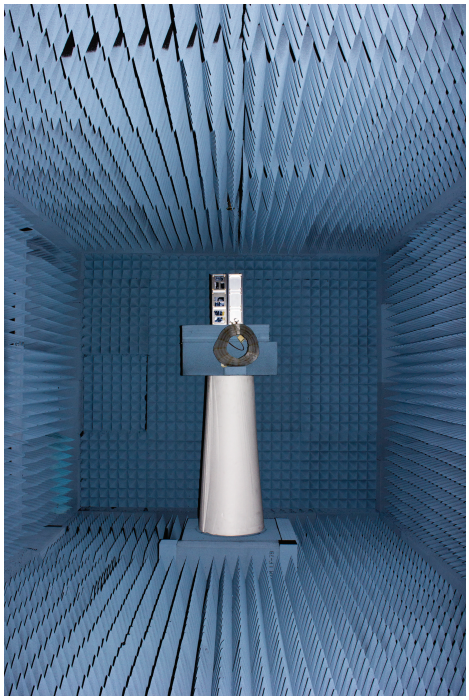

Figure 3.8: CLS antenna and CubeSat assembly mounted in anechoic chamber at the University of New Mexico for radiation pattern measurements

width. No change in performance was observed after the antenna was folded and instantaneously deployed.

3.5 Prototype Structural Performance

3.5.1 Prediction of Vibration Modes

One of the first steps of spacecraft structural design is to investigate the natural frequencies of vibration of the structure to ensure that the natural modes of vibration are away from environmental forcing frequencies. Hence, a requirement that the fundamental frequency of the antenna must be higher than 0.1 Hz has been specified to prevent excitation of the structure by spacecraft maneuvers.

The natural frequencies of the selected antenna designed in Section 3.3 have been computed using ABAQUS/Standard with free boundary conditions. Reduced integration quadrilateral elements (S4R) have been used with a mesh size of 1 mm in the hinge regions and 5 mm elsewhere, for a total of ~19,000 elements (Figure 3.10). A linear elastic laminated plate material model was implemented using the `*Shell General Section` keyword which allows direct input of the composite shell properties for a given shell thickness. The in-plane stiffness matrices of the two composites are

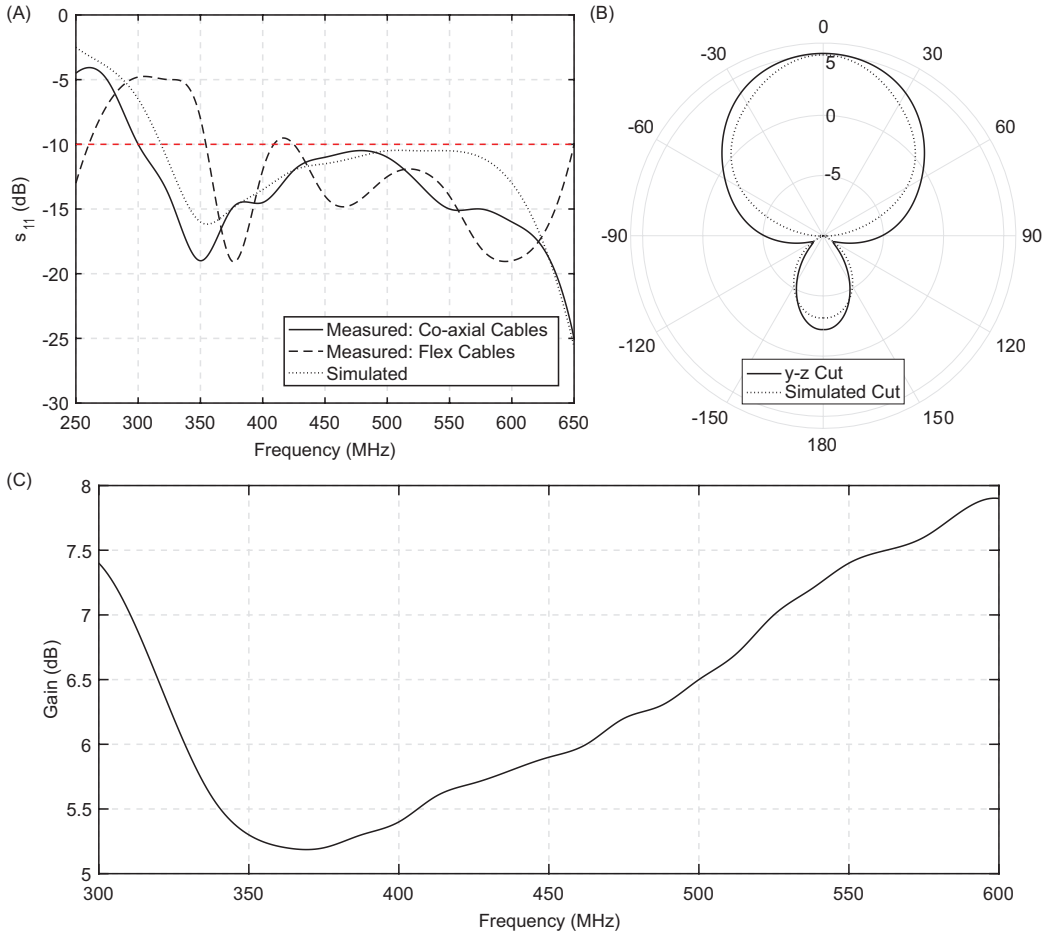

Figure 3.9: RF measurements of antenna prototype (A) reflection coefficient (B) radiation pattern cuts at 450 MHz (C) gain as a function of operating frequency

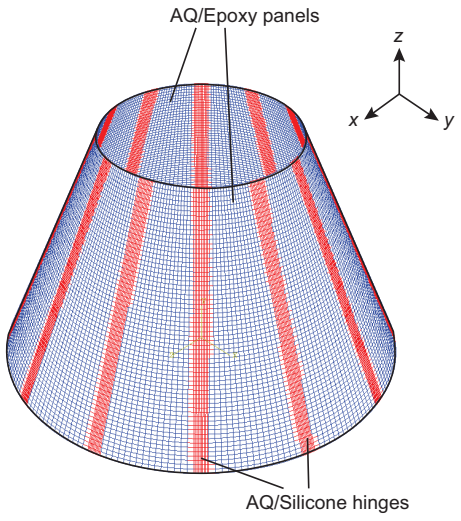

Figure 3.10: ABAQUS model of dual-matrix conical shell with free boundary conditions.

given by,

$$\boldsymbol{A_e} = \begin{bmatrix} 7356 & 2502 & 0 \\ 2502 & 7356 & 0 \\ 0 & 0 & 3114 \end{bmatrix} \text{ N/mm} \tag{3.4}$$

$$\boldsymbol{A_s} = \begin{bmatrix} 4460 & 1491 & 0 \\ 1491 & 4460 & 0 \\ 0 & 0 & 1495 \end{bmatrix} \text{ N/mm} \tag{3.5}$$

where $\boldsymbol{N} = \boldsymbol{A\varepsilon}$, $\boldsymbol{N}$ are the force resultants per unit width of the composite, $\boldsymbol{\varepsilon}$ are the mid-plane strains, and the e and s subscripts refer to the epoxy and silicone composites respectively. The out-of-plane bending stiffness of the composites is given by,

$$\boldsymbol{D_e} = \begin{bmatrix} 110 & 44 & 0 \\ 44 & 110 & 0 \\ 0 & 0 & 44 \end{bmatrix} \text{ N/mm} \tag{3.6}$$

$$\boldsymbol{D_s} = \begin{bmatrix} 79 & 45 & 0 \\ 45 & 79 & 0 \\ 0 & 0 & 45 \end{bmatrix} \text{ N/mm} \tag{3.7}$$

where $\boldsymbol{M} = \boldsymbol{D\kappa}$, $\boldsymbol{M}$ are the moment resultants per unit width of the composites, and $\boldsymbol{\kappa}$ are the mid-plane strains. The values are predicted using classical lamination theory in combination with the mosaic model as described in Section 4.6. The areal density of the composites is specified to ensure an accurate mass for the model. The eigenfrequencies of the antenna are obtained using a linear perturbation step with the Lanczos eigensolver. The conductor is not included in the analysis as its effects on the stiffness of the structure are negligible.

The effect of a folding and instantaneous deployment cycle on the antenna performance is modeled through a reduction of bending stiffness of the silicone composite to 40% of its original value. After folding and deployment some fibers may show residual deformation. Hence, the next time the antenna is folded the fibers microbuckle at lower curvatures, resulting in reduced stiffness. Experimental measurements illustrating this effect are given in Section 4.8.1. It is not expected that forced vibration of the antenna will be enough to induce this microbuckling, however, the softer material properties can give a lower bound for the fundamental frequency of the antenna.

Table 3.4 summarizes the results of the simulations. Frequencies are quoted for the unfolded hinges, where the full bending stiffness of the AQ/silicone composite is used, as well as for hinge bending stiffness of 40% of the original. The corresponding mode shapes for the full and reduced stiffness are shown in Figure 3.11.

	f_0 (Hz)	f_1 (Hz)	f_2 (Hz)
Unfolded	11.54	12.09	29.73
40% Stiffness	6.44	6.54	17.86

Table 3.4: Summary of vibration frequencies of antenna for unfolded and folded hinges

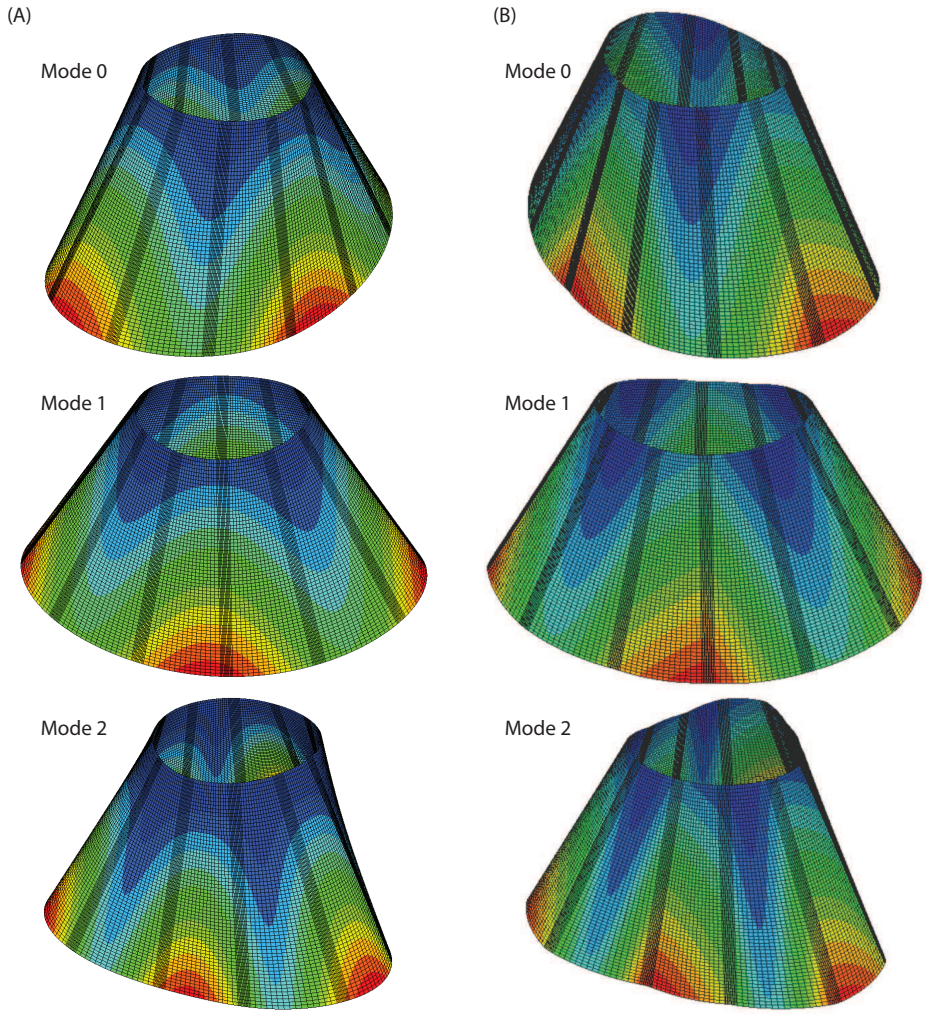

Figure 3.11: Mode shapes for the 3 first natural frequencies of the antenna (A) hinges unfolded (B) hinges with 40% of original stiffness

Simulations show that the antenna has significantly higher fundamental frequency than the 0.1 Hz requirement. With a hinge stiffness of 40% of the pre-fold stiffness, the frequencies are reduced to ~60% of their original values as the antenna is much softer transverse to the shell surface. From the mode shapes in Figure 3.11, it can be seen that the first three modes are all bending modes with an increasing number of waves across the circumference and hence a reduced bending stiffness of the hinges results in a large knockdown in frequencies. However, even with this worst-case lower-bound

on the frequencies, the stiffness requirement is still met.

3.5.2 Measured Vibration Modes

A vibration test on the manufactured antenna prototype was conducted to verify the vibration frequency simulations and to confirm that the stiffness meets requirements. The experimental setup used is photographed in Figure 3.12. The setup was placed on a granite table to reduce vibrations from the environment with the antenna suspended using strings made of Spectra fibers to simulate free boundary conditions. The suspension resembled a double pendulum with string lengths adjusted such that the natural frequency of the suspension was well below the expected frequencies of the antenna. The chosen lengths were 32 cm for the upper suspension and 12 cm for the lower suspension, resulting in a frequency of 1.5 Hz.

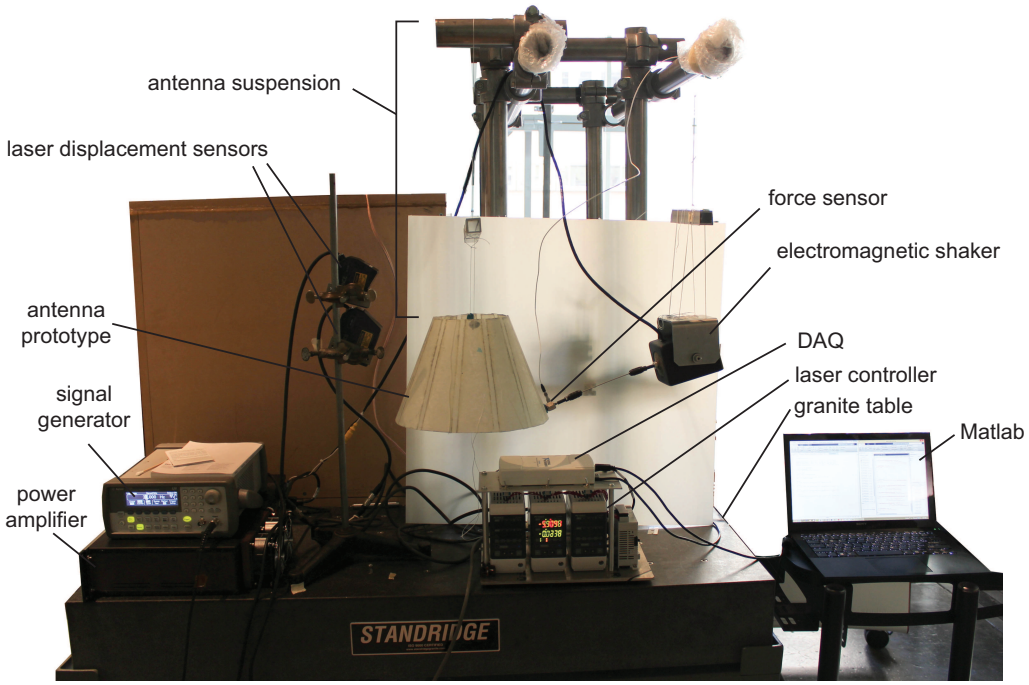

Figure 3.12: Experimental setup for vibration analysis

The excitation was provided by a Labworks Inc. ET-132 electromagnetic shaker. A sinusoidal sweep ranging from 3-30 Hz over 450 s was produced using an Agilent 33250A waveform generator and was routed through a Labworks Inc. pa-138 power amplifier to the shaker. The shaker transmitted the excitation to the antenna using a 19.5 cm long stinger. The force applied to the antenna was measured using a PCB Piezotronics ICP 208C01 force sensor attached to the end of the stinger at one end and to the prototype using wax at the other end.

The output response of the antenna was measured by two laser displacement sensors. A Keyence LK G157 laser measured the displacement at the top of the prototype opposite the applied excitation,

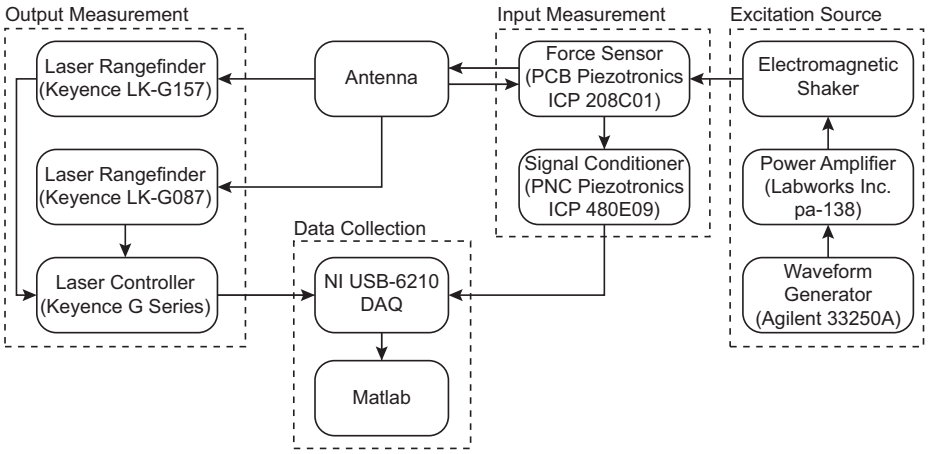

Figure 3.13: Experimental setup for vibration analysis

and a Keyence LK G087 laser measured the displacement at the bottom of the prototype. The displacements were measured at multiple points in order to capture the different vibration modes. All analog signals were wired as differential inputs into an NI USB 6210 data acquisition system and the data was collected and analyzed using the Matlab software. Figure 3.13 shows a schematic of the instrumentation with all connections.

The measured force and displacement signals were filtered using a high pass Butterworth filter (stopband frequency of 2.8 Hz, passband frequency of 3 Hz, stopband attenuation of 60 dB, and 1 dB of ripple allowed in the passband) to eliminate low frequency oscillations observed in the force sensor data. Welch's method was used to determine the power spectral density of each signal. In this scheme, the signal is divided into overlapping sections, each of which is windowed, and a discrete Fourier transform of each is performed. This method has the advantage of significantly reducing noise in the signal at the cost of reduced frequency resolution. Here, 30 sections with 50% overlap were used with a resolution of 0.01 Hz achieved. The ratio of antenna displacement to input force was used as the frequency response function used to extract the natural frequencies of the system [52].

The measured frequency response functions of the antenna prior to folding and after folding and instantaneous deployment are shown in Figures 3.14. The peaks in the response corresponding to the first three natural frequencies can be seen clearly in both laser readings. However, as the bottom laser measures larger displacements, a cleaner signal is seen, in particular for the fundamental frequency.

A summary of the measured natural frequencies and their comparison to simulation predictions is given in Table 3.5. Note that the simulated frequencies quoted here account for the mass of the force sensor using the `*Mass` keyword in ABAQUS. The mass of the force sensor is 26 g, a significant fraction of the antenna mass of 79 g, and hence becomes a part of the excited system.

The experimentally measured frequencies agree with simulations within 6% for the fundamental frequency and within 20% for higher frequencies. Any discrepancies are likely due to the fabrication

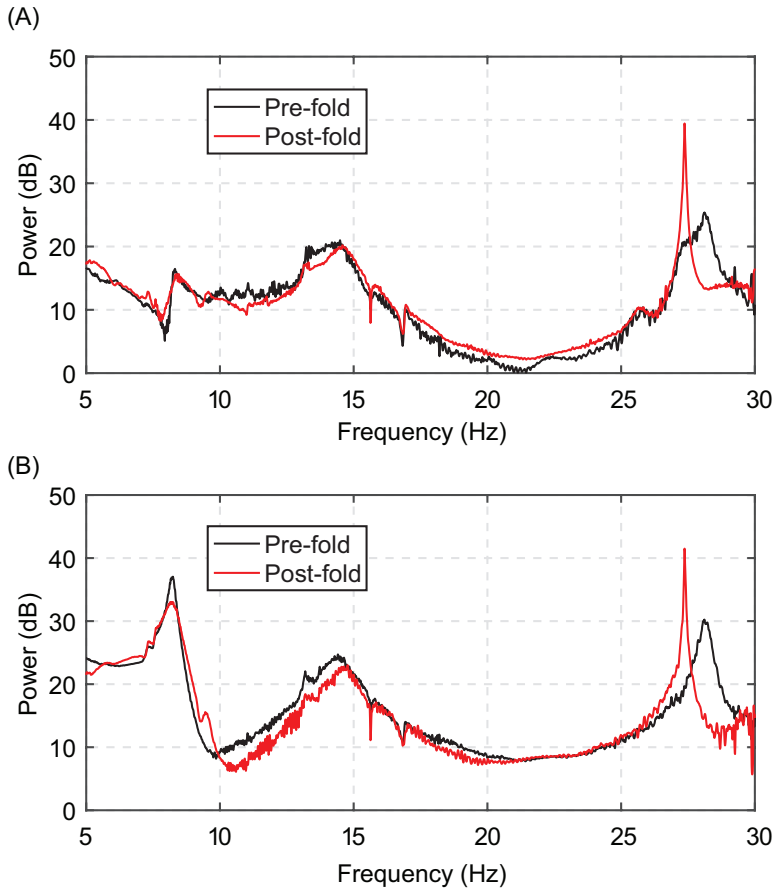

Figure 3.14: Frequency response function of antenna (A) top laser reading (B) bottom laser reading

	f_0 (Hz)	f_1 (Hz)	f_2 (Hz)
Pre-folded Antenna	8.24	14.41	28.09
Post-folded Antenna	8.23	14.77	27.37
Simulation	8.74	11.06	23.43

Table 3.5: Experimentally measured natural frequencies of antenna prototype

process which resulted in imperfections such as wrinkles and non-uniform thickness distribution. In addition, errors can result from inaccuracies in prediction of composite stiffness given in Equations 3.4 – 3.7. Most importantly, the post-fold frequencies show little change from the shell as manufactured, with the fundamental frequency changing by only 0.1%. As predicted in Section 3.5.1, the forced vibration is not enough to trigger early microbuckling after a folding cycle and hence the bending stiffness of the hinge regions remains unchanged. The slight shift in higher frequencies is likely a result of the antenna having to be re-suspended after folding, resulting in a shift of the symmetry-breaking imperfections relative to the setup.

3.6 Conclusion

Although, the design methodology in Chapter 2 showed dual-matrix composites to be a promising, versatile packaging scheme for CubeSat antennas, no experimental data existed to demonstrate this in practice. Hence a specific prototype was designed and tested here. A specific point design for a dual-matrix composite CLS antenna was optimized for RF performance starting from the design derived from the preliminary design tool in Chapter 2.

A summary of the predicted and measured antenna performance, both before and after a folding and deployment cycle, is given in Table 3.6. It can be seen that the prototype antenna meets all requirements, its performance agrees with predictions from numerical simulations, and most significantly its performance is unaffected by packaging indication that after deployment the antenna has sufficient shape accuracy. Note that the packaged dimensions were predicted using equations in Table A.2 and measured experimentally by folding the antenna prototype.

Performance Metric	Requirement	Predicted	Measured Before Folding	Measured After Folding
Gain (dB)	> 5	5.36	5.57	5.57
Bandwidth (MHz)	Maximize	318 - 650	300 - 650	300 - 650
Packaged Dimensions (cm^3)	$< 30 \times 10 \times 5$	$19.6 \times 7.4 \times 1.2$	$19.7 \times 8.2 \times 1.5$	N/A
Fundamental Frequency (Hz)	> 0.1	8.74	8.24	8.23

Table 3.6: Performance summary of antenna prototype RF and structural metrics

The antenna was deployed instantaneously in this study to detect damage during folding. However, another factor which can have an effect on antenna performance is viscoelasticity of the polymer matrices. To gage the effects of viscoelasticity, the antenna should be folded and stored for long times or at elevated temperatures. This is investigated further in Chapter 7.

Chapter 4

Fabrication and Material Characterization

4.1 Introduction

For any composite material, the microstructure is of interest for modeling the homogenized macroscopic material behavior. This is true in the case of the dual-matrix composites studied in this work as well. Many investigations have been conducted to study the microstructure of unidirectional elastomeric composites by Francis [11], Maqueda [13, 31], and Lopez-Jimenez [29, 53]. In addition, these studies have looked at macroscopic behavior and damage mechanism. However, there exist little research on woven elastomeric composites which have advantages in terms of fabrication and damage mitigation. Such studies are of particular importance to deployable structures which use stored strain energy as the deployment mechanism. Knowledge of the macroscopic stiffness of the composites is required for accurate prediction of the deployment behavior.

In this chapter, the experimental aspects of composite material characterization are addressed. The constituent material properties of the composites studied are presented. Fabrication techniques for dual-matrix composites are outlined and an investigation of the interface region between the epoxy and the silicone composites is presented. The microstructure of the dual-matrix composites is studied using optical microscopy, focusing on the differences between epoxy and silicone composites. Furthermore, the homogenized material properties of the composites are measured experimentally and compared to predictions from the mosaic model, a popular analytic tool. Information about the homogenized stiffness of the composites is used for deployment studies in Chapter 5. Furthermore, knowledge of the microstructure is used to develop finite element homogenization models in Chapters 6 and 7.

4.2 Constituent Materials

The selection of constituent materials used for all prototypes and modeling in this thesis was driven by the antenna application in Chapter 3 as well as fabrication considerations. The conical shell must act as a dielectric with conductivity only in the regions specified by Equation 3.2. Astroquartz II (AQ) fibers were selected as the reinforcement material over the much stiffer carbon fiber due to their superior dielectric properties. The AQ was procured as a dry plain-weave fabric from JPS composites (style 525) [18]. A woven fabric was selected for the reinforcement for ease of handling. Another advantage of a woven reinforcement is mitigation of damage due to fiber and matrix debonding from loads transverse to the fibers, as observed in [53]. The properties of the quartz fibers are listed in Table 4.1. The fibers are of high purity, with a silica content of 99.9% [18], resulting in high tensile strength as well as a low dielectric constant.

Astroquartz II Fibers	
Modulus, $E_{1,f} = E_{2,f}$ (GPa)	72
Poisson's Ratio, ν_f	0.16
Tensile Strength (GPa)	6.0
Density, ρ_f (g/cm^3)	2.2
Fiber Diameter, D_f (µm)	9.0
Dielectric Constant (at 1 MHz)	3.7
Style 525 Fabric	
Areal Density (g/m^2)	68
Warp Count (fibers per in.)	50
Fill Count (fibers per in.)	50
Thickness (µm)	65

Table 4.1: Material properties of Astroquartz II fibers and style 525 fabric [18]

The F4-B epoxy resin from Patz Material Technologies [19] was used to form the stiff composite panels. The resin was provided on a paper backing to be transferred to the fabric using heat. The LOCTITE 5055 UV-cure silicone [20] was selected for the flexible hinge areas. The chosen silicone can achieve strains up to 300% before yielding. The AQ fibers are UV transparent, enabling the use of this silicone here instead of addition-cure silicones which require long cure times. However, the UV-cure silicone cannot easily be cured under pressure resulting in a thicker composite with lower fiber volume fractions. The particular silicone was chosen for its low viscosity, allowing it to fully infiltrate the AQ fabric during fabrication. A summary of the mechanical properties of the matrices are given in Table 4.2.

A thin phosphor bronze mesh from TWP Inc. was embedded [21] in the conductive regions of the

	Epoxy	Silicone
Modulus, E_m (GPa)	3.39	0.002 - 0.004
Tensile Strength (MPa)	65.5	9.3
Density, ρ_m (g/cm^3)	1.23	0.98
Poisson's Ratio, ν_m	0.35	0.48

Table 4.2: Material properties of epoxy F4-B [19] and silicone LOCTITE 5055 [20] matrices

shell. Table 4.3 provides a summary of the mesh properties. The mesh was selected to be sufficiently thin and flexible for embedding within the composite shell and not breaking/kinking when folded. However, the mesh thickness must be greater than 5δ, where δ is the skin depth of the conductor at the lowest frequency of operation. The skin depth was computed using,

$$\delta = \sqrt{\frac{\rho}{\pi f \mu_0 \mu_R}} \tag{4.1}$$

where ρ is the conductor resistivity, f is the lowest frequency of operation, μ_R is the relative permeability, and $\mu_0 = 4\pi \cdot 10^{-7}$ Vs/Am is the vacuum permeability. For this material, the skin depth at 250 MHz is δ = 4.1 µm and hence the mesh wire diameter of 35.6 µm meets this requirement. Furthermore, in order for the gaps in the mesh to have a negligible impact on performance, their size must be less than $\lambda/10$ at the highest frequency of operation. The mesh has a gap size of 0.04 mm which is significantly less than a tenth of the wavelength at 650 MHz of 4.6 cm.

Phosphor Bronze Mesh	
Wire diameter (µm)	35.6
Wires per in.	325
Opening size (mm)	0.04
Areal density (g/m^2)	290

Table 4.3: Material properties of phosphor bronze mesh [21]

4.3 Dual-Matrix Composite Fabrication Techniques

The fabrication of dual-matrix composites is described for the antenna prototype presented in Chapter 3. The prototype was fabricated starting with dry AQ fabric which was impregnated with each resin in the desired locations. The epoxy resin was transferred to the fabric using heat while the hinge regions were masked with Kapton (Figure 4.1(A)). The composite plies were stacked by aligning the hinges and the mesh conductor was embedded at the mid-plane of the composite (Figure 4.1(B)).

The inner plies of the antenna were cut at the apex of the antenna to expose the conductor for connecting the feed lines. The silicone was then transferred to the hinge regions by injecting small amounts with a syringe and allowing the resin to flow until the fabric is fully impregnated. A cotton swab was used to spread the silicone evenly and remove any excess, if required (Figure 4.1 (C)). The silicone layup was debulked under vacuum for 15 mins to evacuate the air bubbles from the silicone and consolidate the layup. This ensures a good cure of the silicone resin as it is inhibited by oxygen. The silicone was prevented from spreading past the hinge areas by the epoxy resin already in place. The silicone was then degassed and cured between two acrylic plates under a UV lamp (Spectroline UV Lamp XX-15A operating at 365 nm) with an irradiance of 40 mW/cm^2 at a distance of 35 mm (Figure 4.1(D)). The layup was wrapped around a conical mold, with a cone angle matching that of the antenna, and vacuum bagged. The epoxy was cured in a traditional autoclave cure at 120^{o}C for 2 hours (Figure 4.1(E)).

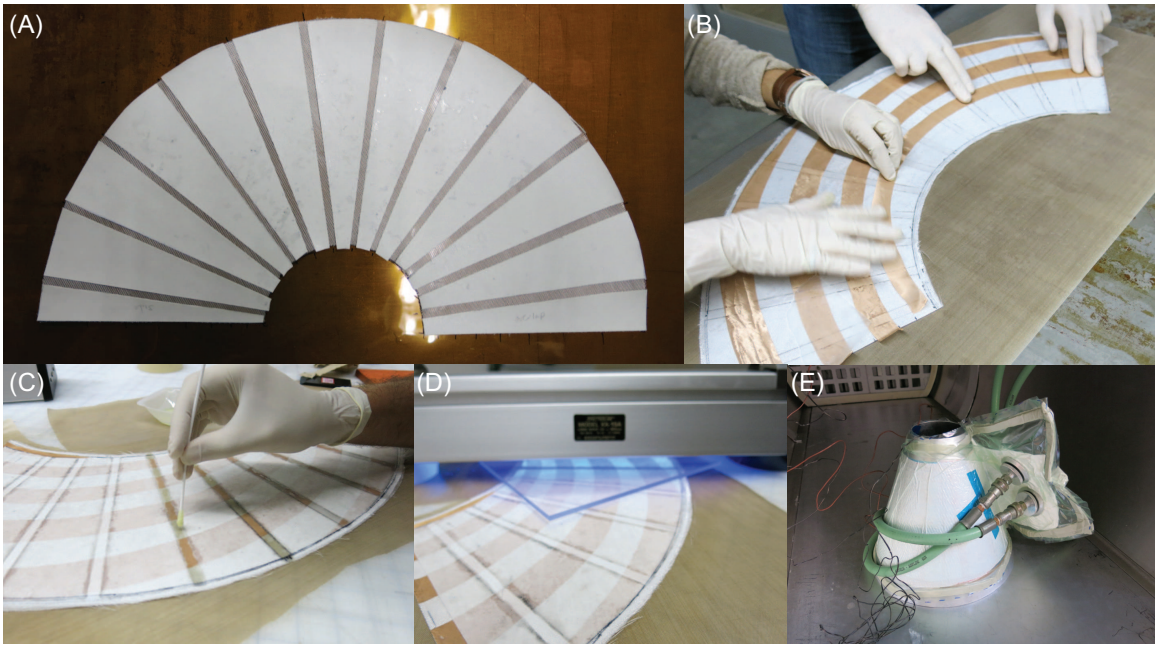

Figure 4.1: Fabrication of a dual-matrix composite antenna (A) Masking of silicone hinges and epoxy transfer via heat (B) Stacking of plies and embedding of conductor (C) Impregnation of hinge regions with silicone (D) UV-cure of silicone (E) Epoxy cure in autoclave

The silicone used undergoes a condensation cure producing water and methanol as byproducts which diffuse out of the composite over time. A heat-treatment of 48 hrs at 140^{o}C under vacuum was found to be sufficient to bake-out these byproducts and stabilize the mass of the composite. This step prevents the volatiles from diffusing out of samples during testing, causing the silicone to shrink and affect test results.

4.4 Interface Characterization

The interface region between the AQ/epoxy and AQ/silicone composites is shown in Figure 4.2. A non-planar interface approximately 0.5 mm across is seen between the two composites, resulting from flow of the silicone resin before cure due to its low viscosity. The extent of the region is limited by impregnating the fabric with the epoxy resin first. The modulus of the matrices across this interface was measured to determine the presence of uncured resin.

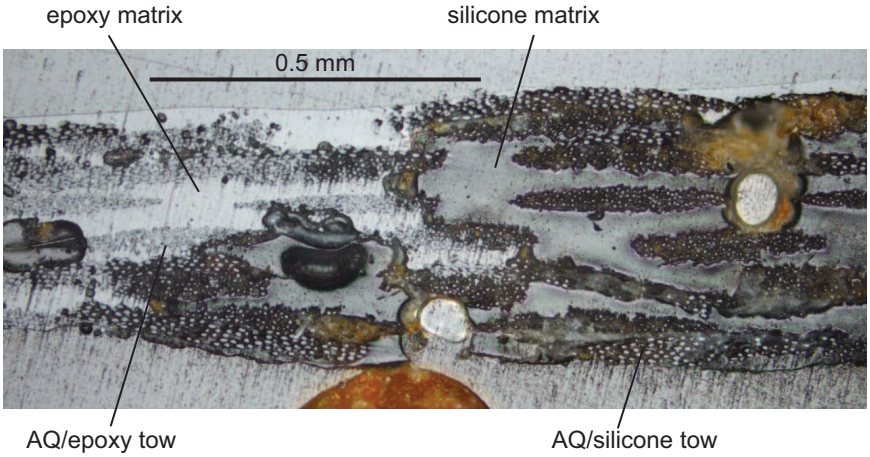

Figure 4.2: Micrograph of the interface region between the AQ/epoxy and AQ/silicone composites

The moduli were measured at precise distances from the interface using the nanoindentation technique, with measurements carried out using the Hysitron TI 950 Triboindenter from Burker [54]. This instrument precisely measures the load, P, as a function of the indent depth, h, at the nanoscale. Nanoindentation tests were required to avoid indenting the AQ fibers. A typical indentation profile consists of a displacement applied linearly, held constant, and then removed. The modulus of the material can then be computed from,

$$\frac{1}{E_r} = \frac{1-\nu^2}{E} + \frac{1-\nu_i^2}{E_i} \tag{4.2}$$

where E is the Young's modulus of the matrix, ν is the Poisson's ratio of the matrix, and the subscript i indicates indenter properties [55]. The reduced modulus, E_r, is computed from the unloading slope and the indenter geometry,

$$E_r = \frac{dP}{dh}\frac{1}{2\beta}\sqrt{\frac{\pi}{A}} \tag{4.3}$$

where β is a geometric factor obtained from finite element analysis, and A is the area of the indenter [55]. The analysis presented here is valid for bulk materials and can be applied to the composites in this case as the indentation depth is much smaller than the ~200 μm composite thickness and the matrices are indented far away from the fibers.

For the tests here, a Berkovich indenter was used, a three sided pyramid with a half-angle of 65.27^o. For this indenter, $\beta = 1.034$ and for an ideal indenter, $A(h) = 24.5h^2$ [55]. In practice, the area function is calibrated using,

$$A(h) = C_0 h^2 + C_1 h + C_2 \sqrt{h} \tag{4.4}$$

where the constants have been measured to be $C_0 = 23.7501$, $C_1 = 1.515 \times 10^3$, and $C_2 = 2.1513 \times 10^3$ by indenting a fused silica sample with known properties.

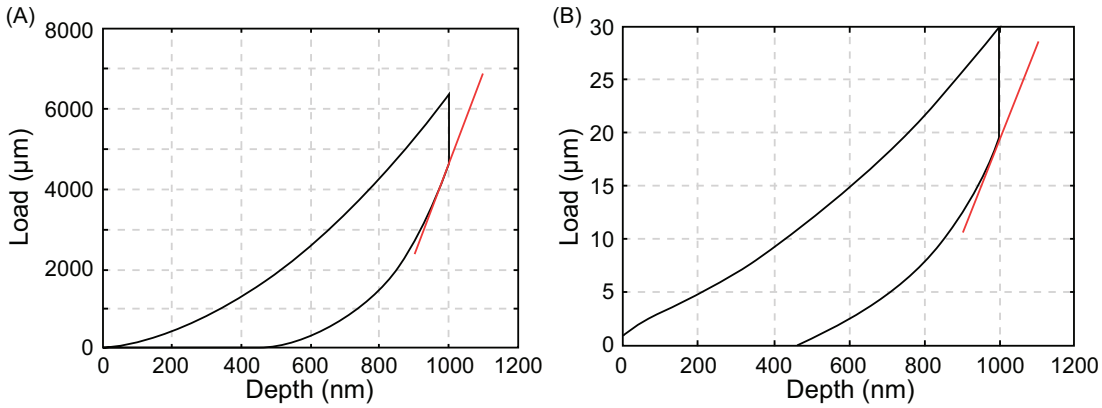

Figure 4.3: Indentation load curves with unloading slopes indicated for (A) epoxy (B) silicone

Several values of dwell time and indent depth were investigated. A dwell time that is too short would show results significantly impacted by the initial viscoelastic relaxation of the matrices. Selecting an indent depth too shallow would yield inaccurate results but a depth too large may be affected by AQ fibers. The final profile selected was an indent depth of 1 μm applied at a loading/unloading rate of 33.3 nm/s, and a dwell time of 2 mins. The measured loads, with the unloading slopes marked in red, for the epoxy and silicone are shown in Figure 4.3.

In order to obtain accurate readings, the rms surface roughness must be an order of magnitude less than indent depth. In this case, the composite was embedded in potting epoxy and polished to a target rms roughness of 50 – 100 nm. The surface was successively polished with 600 grit sandpaper, 9/6/3/1 μm Buehler MetaDi diamond polishing paste, and 0.05 μm Buehler MicroPolish Aluminua suspension. The achieved surface roughness was 0.30 nm rms for the epoxy and 0.55 nm rms for the silicone.

Distance to Interface (mm)	0.03	2.0	5.0
Epoxy Modulus (GPa)	3.30	3.49	3.74
Silicone Modulus (MPa)	1.42	1.61	1.60

Table 4.4: Measured matrix moduli as a function of distance from the interface

The measured moduli for the epoxy and silicone matrices as a function of distance from the interface are summarized in Table 4.4. It can be seen that the modulus changes sharply across the interface, with the modulus of the epoxy and silicone rising 12% and 15% away from the interface, respectively. The measured values compare well with the datasheet values of 3.39 GPa for the epoxy and 2 MPa for the silicone. The lower measured value of the silicone is due to viscoelastic relaxation of the material during the dwell period. Overall, these results show that both matrices are sufficiently cured at the interface and are not inhibited by each other's presence.

4.5 Microstructure Characterization

Investigating the microstructure of the AQ/epoxy and AQ/silicone composites can give insight into modeling these materials and may give clues on whether existing models for traditional composites are appropriate for the silicone composites. Previous literature has investigated microstructure only for unidirectional elastomeric composites [13, 29, 31, 53]. Extending the study to woven silicone composites adds levels of complexity: including two levels of microstructure (the tow and the weave), and accurate prediction of out-of-plane properties of the tow for successful modeling of the 3D weave.

4.5.1 Micrographs

Micrographs of the plain-weave microstructure of the AQ/epoxy and the AQ/silicone composites are shown in Figures 4.4 and 4.5, respectively. These were obtained using a Nikon Eclipse LV150N optical microscope by potting samples in epoxy and polishing them flat. The micrographs show the fibers are contained in lenticularly shaped tows. The undulation of these tows in the fiber direction can be observed by looking at the in-plane tows. It is also observed that the tows can be in-phase or out-of-phase with those of the neighboring plies. This effect is observed in both composites and may have a significant effect on bending stiffness as suggested by Soykasap [37]. Finally, a variation is observed in the composite thickness, following the shape of the tows.

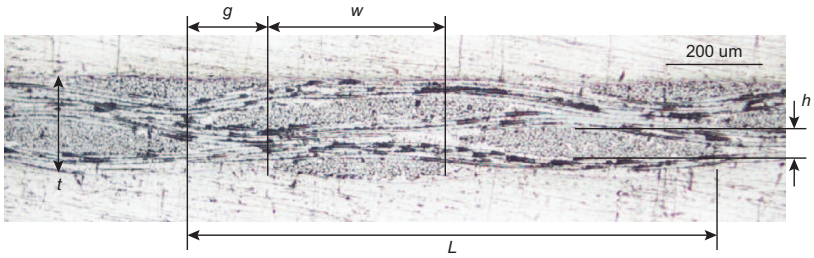

Figure 4.4: Micrograph at 10X magnification of the microstructure of a $[0_3]_{pw}$ AQ/epoxy composite

Figure 4.6 shows a micrograph of the $[\pm 30/0]_{s,pw}$ layup used for the antenna prototype in Chapter 3. The conductive mesh can be seen embedded at the mid-plane of the composite. It can be

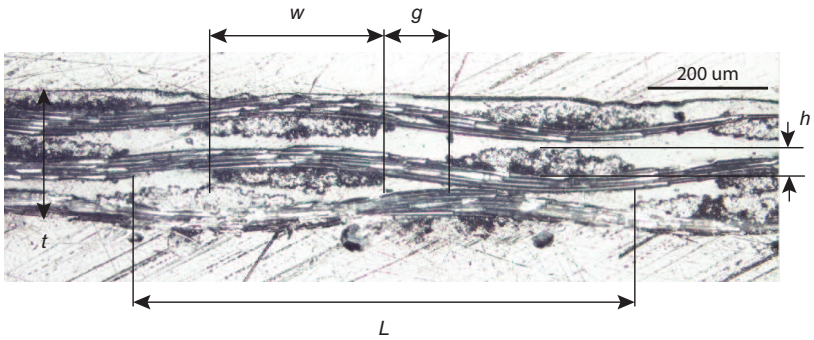

Figure 4.5: Micrograph at 10X magnification of the microstructure of a $[0_3]_{pw}$ AQ/silicone composite

observed that there are no voids surrounding the conductor and that the epoxy resin impregnated the mesh fully during cure.

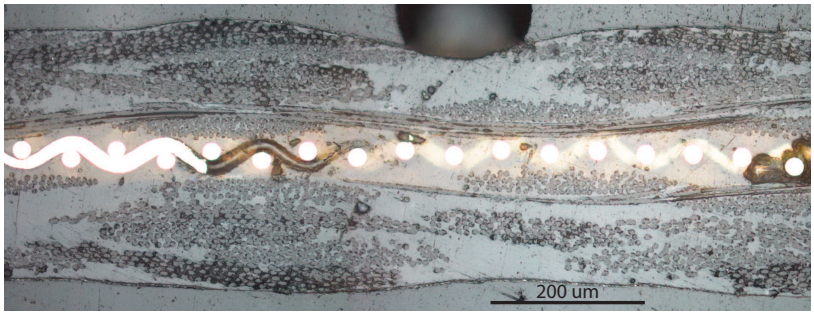

Figure 4.6: Micrograph at 20X magnification of the microstructure of a $[\pm 30/0]_{s,pw}$ AQ/epoxy composite with embedded conductor

4.5.2 Plain-Weave Geometry

The geometry of the plain-weave can be described using the parameters indicated in Figures 4.4 and 4.5, namely the wavelength of the unit cell, L, the tow width, w, the tow height, h, the tow spacing, g, and the composite thickness, t. The wavelength, tow width, and tow spacing are not independent with $L = 2(w + g)$.

Parameter	L		w		g		h		t	
	Mean	St. Dev.	Mean	St. Dev.	Mean	St. Dev.	Mean	St. Dev.	Mean	St. Dev.
AQ/epoxy (µm)	1032	28	364	16	152	15	42.1	3.2	75.2	3.9
AQ/silicone (µm)	1068	38	374	21	106	24	47.1	4.5	92.8	5.1

Table 4.5: Measured plain-weave geometry for the AQ/epoxy and AQ/silicone composites

Table 4.5 summarizes the mean values for these parameters each averaged over 80 measurements from 4 different samples. It can be seen that the silicone composite has a looser weave and larger tow

heights, as it was not cured under pressure like the epoxy composite. This is particularly evident by the large difference in composite ply thickness, where the epoxy plies are only 81% as thick as the silicone ones. Furthermore, for the epoxy composite $t << 2h$ as the tows are not stacked directly on top of each other, particularly when neighboring plies are out-of-phase. For the silicone composite $t \approx 2h$ due to the lack of pressure during cure. This difference of thickness relative to the tow height is critical to capture in homogenization models as the thickness significantly impacts fiber volume fraction and stiffness.

4.5.3 Composite Fiber Volume Fraction

The composite fiber volume fraction is critical to the homogenized stiffness of the composite and was computed here by measuring the dry fabric mass, m_f, and the final composite mass, m_{tot}. The mass of the matrix is then,

$$m_m = m_{tot} - m_f \tag{4.5}$$

The fiber volume fraction cannot be computed directly as only the areal and not volumetric density of the AQ is known. Instead, the matrix volume fraction is computed using,

$$V_m = \frac{m_m/\rho_m}{V_{tot}} \tag{4.6}$$

where ρ_m is the volumetric density of the matrix, and V_{tot} is the volume of the composite, with the thickness obtained from micrographs. The fiber volume fraction, neglecting the effects of fiber sizing and voids, is given by,

$$V_f = 1 - V_m \tag{4.7}$$

The fiber volume fractions of the AQ/epoxy and AQ/silicone composites are summarized in Table 4.6 for 1-ply and 3-ply composites. It can be observed that the volume fraction of the 3-ply composites is higher than that of the 1-ply composites by as much as 40%. This difference is especially noticeable for the epoxy composite as the autoclave pressure causes tows from upper plies to fill the resin pockets of lower plies, pushing out excess resin. In the case of the silicone, this effect is not as noticeable as there is only the vacuum pressure applied during degassing. Overall, the fiber volume fraction of the 3-ply epoxy composite is 35% higher than that of the 3-ply silicone composite, as reflected in the thickness disparity between the two composites.

Ply Count	1	3
AQ/epoxy	0.38	0.54
AQ/silicone	0.37	0.40

Table 4.6: Fiber volume fractions of the AQ/epoxy and AQ/silicone composites

4.5.4 Tow Fiber Volume Fraction

From the micrographs, it can be observed that the volume fraction of the tows is much higher than than of the composite. The tow fiber volume fraction was computed by examining 0.7× 0.18 mm^2 sections of the tows and counting the number of fibers with a known fiber diameter of 9 µm using the Matlab function `imfindcircles`. The tow fiber volume fraction is given by,

$$V_{f,tow} = \frac{\pi D^2 n}{4A} \tag{4.8}$$

where D is the fiber diameter, n is the number of fibers in the section, and A is the total area of the section. The volume fraction was measured in 5 sections for the epoxy composite and averaged.

For the silicone composite, polishing causes the matrix to shear and cover the fibers. Hence, the use of the circle detection algorithm in Matlab was not possible. Instead, it was assumed that the silicone tows contain the same amount of fibers as the epoxy tows, since the dry fabric is the same. The fiber tow volume fraction was then computed from the ratio of areas of the two tows,

$$V^s_{f,tow} = V^e_{f,tow} \frac{w^e h^e}{w^s h^s} \tag{4.9}$$

where the e and s superscripts refer to the epoxy and silicone composite properties respectively.

The resulting tow fiber volume fractions are,

$$V^e_{f,tow} = 0.75 \tag{4.10}$$

$$V^s_{f,tow} = 0.65 \tag{4.11}$$

It can be seen that the tow fiber volume fractions are significantly larger than those of the composite itself reported in Table 4.6. Accurate values for both volume fractions are required to representatively model the distribution of fibers and matrix in the composites.

4.6 Analytic Predictions of Stiffness

The stiffness of a composite laminated plate is generally characterized through its ABD matrix [56],

$$\begin{bmatrix} \boldsymbol{N} \\ \boldsymbol{M} \end{bmatrix} = \begin{bmatrix} \boldsymbol{A} & \boldsymbol{B} \\ \boldsymbol{B} & \boldsymbol{D} \end{bmatrix} \begin{bmatrix} \boldsymbol{\varepsilon} \\ \boldsymbol{\kappa} \end{bmatrix} \tag{4.12}$$

where $\boldsymbol{N}$ are the force resultants, $\boldsymbol{M}$ are the moment resultants, $\boldsymbol{A}$ is the in-plane stiffness, $\boldsymbol{B}$ is the in-plane/flexural coupling stiffness, $\boldsymbol{D}$ is the out-of-plane stiffness, $\boldsymbol{\varepsilon}$ are the mid-plane strains, and $\boldsymbol{\kappa}$ are the mid-plane curvatures. The resultant directions are defined in Figure 4.7.

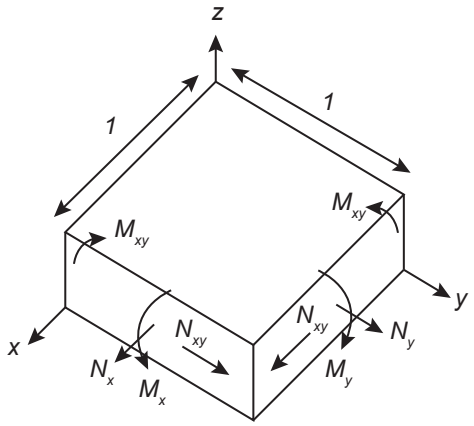

Figure 4.7: Notation for force and moment resultants in CLT

The stiffness matrices for a laminate of n plies are defined in terms of the ply stiffness, $\bar{\boldsymbol{Q}}$, which includes information about the fiber orientation in the ply,

$$\boldsymbol{A} = \sum_{i=1}^{n} \bar{\boldsymbol{Q}}_{\boldsymbol{i}}(z_{i+1} - z_i) \tag{4.13}$$

$$\boldsymbol{B} = \frac{1}{2} \sum_{i=1}^{n} \bar{\boldsymbol{Q}}_{\boldsymbol{i}}(z_{i+1}^2 - z_i^2) \tag{4.14}$$

$$\boldsymbol{D} = \frac{1}{3} \sum_{i=1}^{n} \bar{\boldsymbol{Q}}_{\boldsymbol{i}}(z_{i+1}^3 - z_i^3) \tag{4.15}$$

In Classical Lamination Theory (CLT), it is assumed that each ply is orthotropic with respect to the fiber direction and homogeneous through thickness and hence the ply stiffness can be calculated from in-plane properties. However, for woven composites, the ply is no longer homogeneous through thickness and this approach cannot be used. The mosaic model [37] proposes a modification to CLT to account for the plain-weave. It is proposed that each ply is modeled as a repeating unit cell consisting of two layers of alternating tiles of warp and weft yarns as illustrated in Figure 4.8.

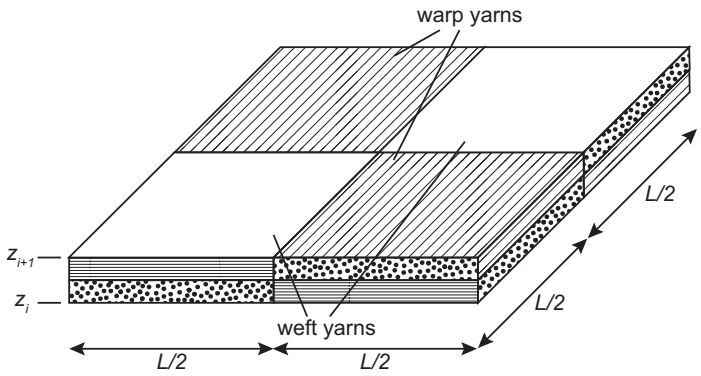

Figure 4.8: Unit cell used to approximate a plain-weave in the mosaic model

The ABD stiffness matrices can be computed as follows for the unit cell,

$$\boldsymbol{A} = \sum_{i=1}^{n} \frac{1}{2} \left(\bar{\boldsymbol{Q}}_{\boldsymbol{i}}^{\,\boldsymbol{0^o}} + \bar{\boldsymbol{Q}}_{\boldsymbol{i}}^{\,\boldsymbol{90^o}} \right) (z_{i+1} - z_i) \tag{4.16}$$

$$\boldsymbol{B} = 0 \tag{4.17}$$

$$\boldsymbol{D} = \frac{1}{3} \sum_{i=1}^{n} \frac{1}{2} \left(\bar{\boldsymbol{Q}}_{\boldsymbol{i}}^{\,\boldsymbol{0^o}} + \bar{\boldsymbol{Q}}_{\boldsymbol{i}}^{\,\boldsymbol{90^o}} \right) (z_{i+1}^3 - z_i^3) \tag{4.18}$$

where $\boldsymbol{B} = 0$ due to symmetry. By comparison with Equations 4.13 – 4.15, it can be seen that the lamina stiffness, $\bar{\boldsymbol{Q}}$, is given by the average of the warp and weft tile stiffnesses.

This approximation neglects the undulation in the yarns and introduces discontinuities i the fibers. It is generally found that the in-plane stiffness is approximated well by this theory, particularly for thicker layups, whereas the bending stiffness can have errors as large as 100% [37].

4.7 Experimental Techniques for Stiffness Measurement

4.7.1 Tension Tests

Tension tests were conducted on 10×1 in.^{2} composite samples to determine their extensional stiffness, $\boldsymbol{A}$. The samples were clamped between grips mounted to an Instron 5569 load frame, with sandpaper between the samples and grips to prevent slipping. An extension was applied to the samples at 1 mm/min. The force, F_x, was measured using Instron 2525 series static load cells, and the displacements parallel and perpendicular to the load direction, d_x and d_y, were measured using LE-01 and LE-05 laser extensometers from Electronic Instrument Research using reflective tape strips mounted on the samples. The test setup is illustrated in Figure 4.9.

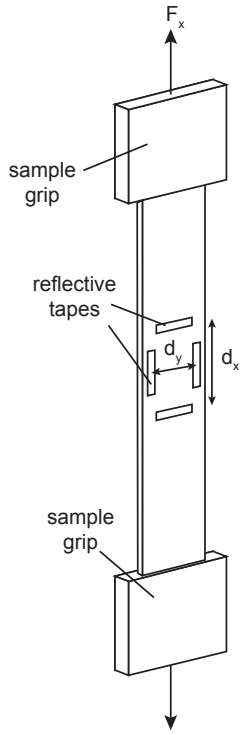

Figure 4.9: Setup used to measure in-plane stiffness

The components of the inverse of the in-plane stiffness matrix, $\boldsymbol{a} = \boldsymbol{A}^{-1}$, can be computed directly from the data,

$$a_{11} = \frac{N_x}{\varepsilon_x} = \frac{F_x/w}{(d_x - d_{x,0})/d_{x,0}} \tag{4.19}$$

$$a_{12} = \frac{N_x}{\varepsilon_y} = \frac{F_x/w}{(d_y - d_{y,0})/d_{y,0}} \tag{4.20}$$

where $d_{x,0}$ and $d_{y,0}$ are the initial distances between the reflective tapes.

If the layup is quasi-isotropic, then $a_{22} = a_{11}$. Otherwise, a tension test in a perpendicular direction must be run to compute a_{22},

$$a_{22} = \frac{N_y}{\varepsilon_y} = \frac{F_y/w}{(d_y - d_{y,0})/d_{y,0}} \tag{4.21}$$

The in-plane stiffness is found by inversion of $\boldsymbol{a}$.

4.7.2 Four-Point Bending Tests

The bending stiffness of the composite samples was measured by performing four-point bending tests on rectangular $2\times1/2$ in.^{2} samples. Four-point bending grips were configured according to the setup shown in Figure 4.10. The bottom grip was the CU-FL-96 4 point bending test grip from Wyoming Test Fixtures and the top grip was 3D printed to reduce mass and accommodate load measurement

with the Instron 2525 series 10 N load cell to reduce noise in measured data. The displacement at the middle of the sample, d, was measured with the laser extensometer.

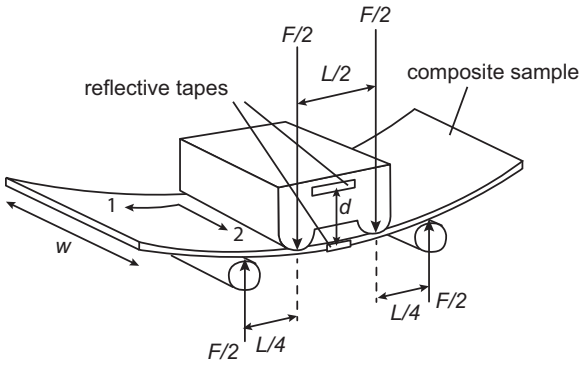

Figure 4.10: Setup used to measure bending stiffness

The four-point bending test results in a constant moment in the center section. This moment per unit width is given by,

$$M = \frac{FL}{8w}$$

The corresponding curvature is,

$$\kappa = \frac{M}{EI} = \frac{FL}{8EIw} \tag{4.22}$$

where E is the modulus of the material, and I is the second moment of area of the sample. The maximum deflection of the sample, $\delta = d - d_0$, where d_0 is the initial distance between the tapes, can be calculated by treating the middle section as a cantilever beam with an applied moment,

$$\delta = \frac{FL^3}{32 \times 8EI} = \frac{L^2}{32}\kappa \tag{4.23}$$

where the second equality is obtained by substituting Equation 4.22. The bending stiffness in the test direction is,

$$D_{11} = \frac{M}{\kappa} = \frac{FL^3}{256w\delta} \tag{4.24}$$

4.8 Comparison of Experimental and Analytic Stiffness

Tension and bending tests were conducted for several layups and the results are summarized here and compared to mosaic model predictions.

Figures 4.11 and 4.12 show tension test of 1- and 3-ply AQ/epoxy and AQ/silicone samples with the weave oriented at 0° and 45° to the loading direction. The load curves of the epoxy composite are linear, with the initial non-linearity when loading in the 45° direction associated with flattening of the undulations of the weave. The load curves of the silicone in Figure 4.12 are also linear when

loading in the weave direction. Although silicone is often modeled as hyperelastic with the Gent model [13, 53], the homogenized composite behavior is linear. However, loading at 45° to the weave shows softening behavior, likely caused by fiber-matrix debonding. This effect was also observed in tests by Lopez-Jimenez and Pellegrino [53] on unidirectional silicone composites when loading transverse to the fibers.

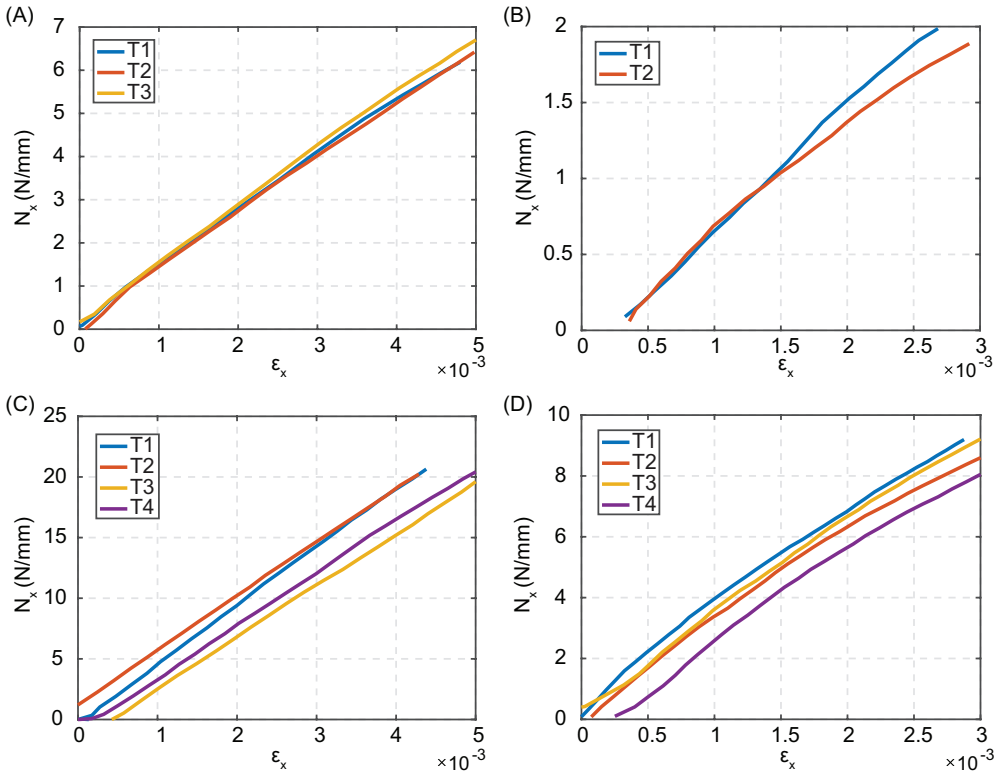

Figure 4.11: Tension test data of AQ/epoxy composite (A) $[0]_{pw}$ (B) $[45]_{pw}$ (C) $[0_3]_{pw}$ (D) $[45_3]_{pw}$

The extensional stiffness, A_{11}, is extracted from the slopes and summarized in the second row of Tables 4.7 and 4.8 for the AQ/epoxy and AQ/silicone composites, respectively. The silicone 1-ply composite stiffness in the 45° direction is taken as the initial slope (up to 0.1% strain). Mosaic model predictions are given in the third rows. There is excellent agreement at 0° between measurements and theory, within 10% for both epoxy and silicone composites. The stiffness at 45^o is over-predicted by the mosaic model for both composites. The prediction is reasonable (~20% error), and results from an over-prediction of the in-plane shear stiffness of a single 0° ply, Q_{33}, which is then propagated through CLT. The error is significantly higher for the 1-ply silicone composite due to damage in the samples. This is reflected in the softening behavior in the data and the relatively high standard deviation in the tests. These results show that in-plane stiffness is predicted sufficiently well by the mosaic model in the absence of damage. However, improvement could be made to the shear stiffness predictions.

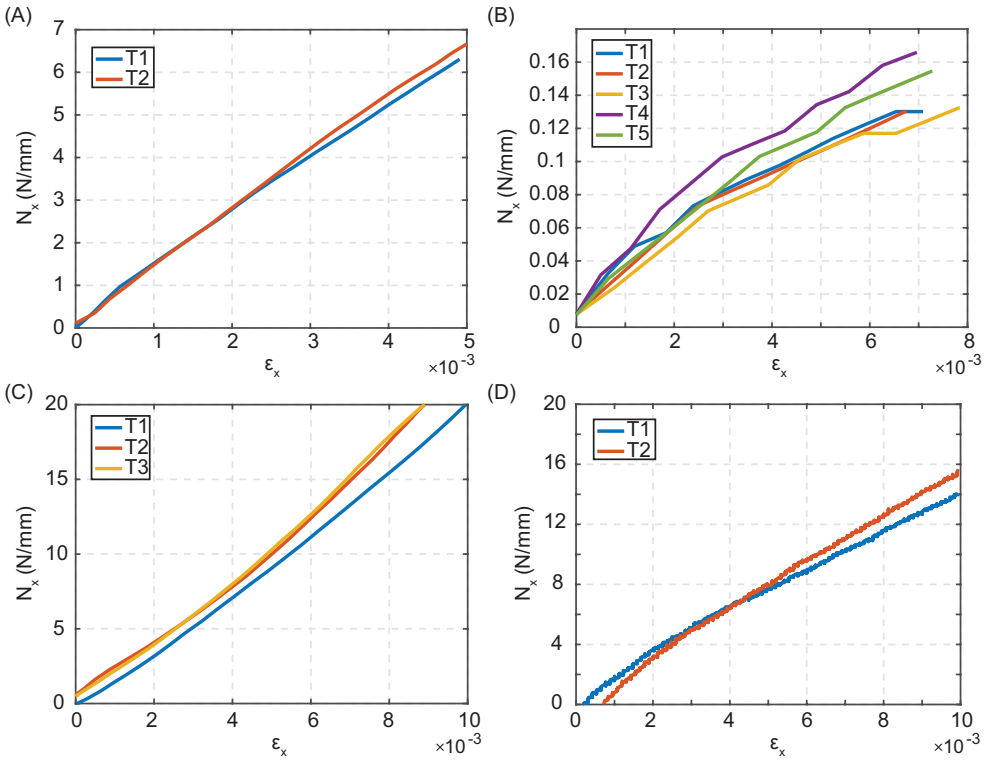

Figure 4.12: Tensions test data of AQ/silicone composite (A) $[0]_{pw}$ (B) $[45]_{pw}$ (C) $[0_3]_{pw}$ (D) $[45_3]_{pw}$

Figures 4.13 and 4.14 show bending data of AQ/epoxy and AQ/silicone samples with the weave oriented at 0° and 45° to the applied curvature direction. The bending tests are also shown for a $[45/0/45]_{pw}$ composite used to construct the dual-matrix hinge in Chapter 5. All behavior in bending is linear, with initial non-linearities associated with slight misalignments of the sample in the test grips. Unloading curves are also shown for the case of the $[45/0/45]_{pw}$ AQ/silicone composite, demonstrating significant hysteresis due to viscoelasticity. This effect will be further explored in Chapter 7.

Comparison to mosaic model predictions to measured values in Tables 4.7 and 4.8 shows that in-plane stiffness predictions are quite accurate but bending stiffness differs significantly from experimental values. For the AQ/epoxy composite the largest error of 38% in bending stiffness occurs for the $[45_3]_{pw}$ laminate. For the AQ/silicone composite, the largest error of 98% occurs also for the $[45_3]_{pw}$ laminate. This highlights the need for more accurate analytic or finite element techniques to predict bending stiffness of woven composites. A more detailed study is presented in Chapter 6.

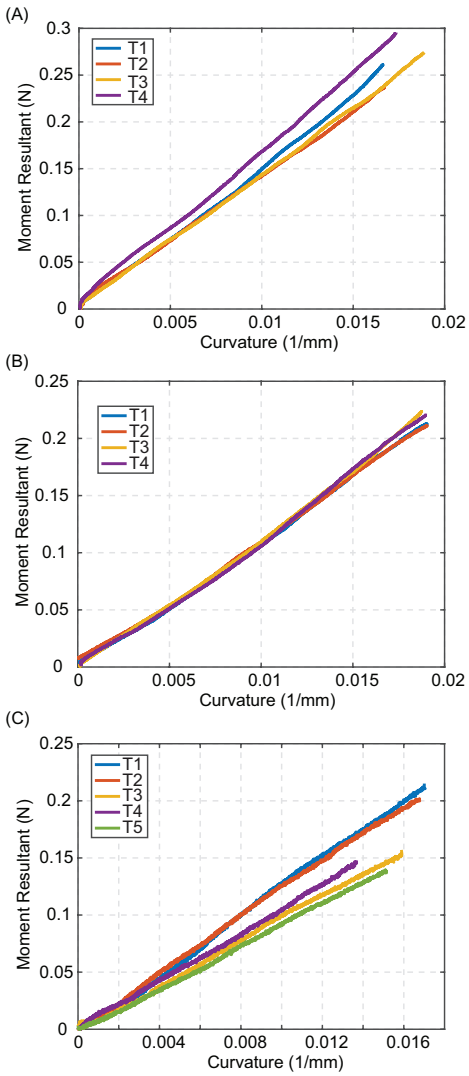

Figure 4.13: Four-point bending test data of AQ/epoxy composite (A) $[0_3]_{pw}$ (B) $[45_3]_{pw}$ (C) $[45/0/45]_{pw}$

Layup	$[0]_{pw}$		$[45]_{pw}$		$[0_3]_{pw}$		$[45_3]_{pw}$		$[45/0/45]_{pw}$	
	Mean	Std. Dev.	Mean	Std. Dev.	Mean	Std. Dev.	Mean	Std. Dev.	Mean	Std. Dev.
A_{11} Experimental (N/mm)	1221	6.3	722	114	4350	75	2727	134	-	-
A_{11} Mosaic Theory (N/mm)	1304	N/A	951	N/A	4473	N/A	3308	N/A	3696	N/A
D_{11} Experimental (N·mm)	-	-	-	-	15.2	1.4	12.1	0.5	12.3	1.3
D_{11} Mosaic Theory (N·mm)	0.49	N/A	0.36	N/A	10.1	N/A	7.5	N/A	7.6	N/A

Table 4.7: Summary of measured and predicted stiffness for various layups of AQ/epoxy composite

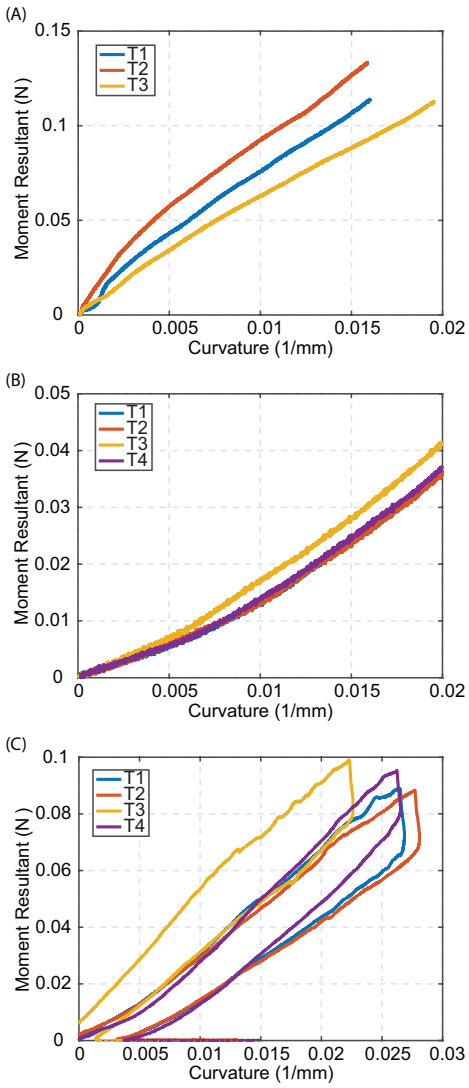

Figure 4.14: Four-point bending test data of AQ/silicone composite (A) $[0_3]_{pw}$ (B) $[45_3]_{pw}$ (C) $[45/0/45]_{pw}$

Layup	$[0]_{pw}$		$[45]_{pw}$		$[0_3]_{pw}$		$[45_3]_{pw}$		$[45/0/45]_{pw}$	
	Mean	Std. Dev.	Mean	Std. Dev.	Mean	Std. Dev.	Mean	Std. Dev.	Mean	Std. Dev.
A_{11} Experimental (N/mm)	1054	177	146	44	2453	76	1419	182	-	-
A_{11} Mosaic Theory (N/mm)	933	N/A	467	N/A	2799	N/A	1401	N/A	1867	N/A
D_{11} Experimental (N·mm)	-	-	-	-	5.71	0.8	2.57	0.1	3.61	0.4
D_{11} Mosaic Theory (N·mm)	0.38	N/A	0.19	N/A	10.3	N/A	5.1	N/A	5.3	N/A

Table 4.8: Summary of measured and predicted stiffness for various layups of AQ/silicone composite

4.8.1 Effects of Fiber Microbuckling

Research by Maqueda [13] has shown that the bending stiffness of silicone composites can be significantly reduced after folding of the sample to high curvatures. A similar test is executed in this study to measure the reduction for the [45/0/45] AQ/silicone composite which is used for deployment studies in Chapter 5. The samples are subjected to a four-point bending test, then are folded to 180° and instantaneously unfolded, and the bending tests are repeated. The bending data is shown for samples before and after folding to 180° in Figure 4.15, in dashed and solid lines respectively. It can be seen that the post-fold curves follow the pre-fold curves initially, but then show significant softening, associated with early onset of fiber microbuckling in the composite. This occurs as after folding, a small amount of the fibers remain deformed triggering microbuckling at lower curvatures that next time the sample is folded. The prefold stiffness is D_{11} = 3.61 N·mm, while the postfold stiffness is D_{11} = 1.45 N·mm, only 40% of the original. This reduction must be accounted for in deployment studies as will be demonstrated in Chapter 5. However, as shown in Section 3.5.2, this softening does not influence the stiffness of deployed dual-matrix composite structures as the initial stiffness is unaffected.

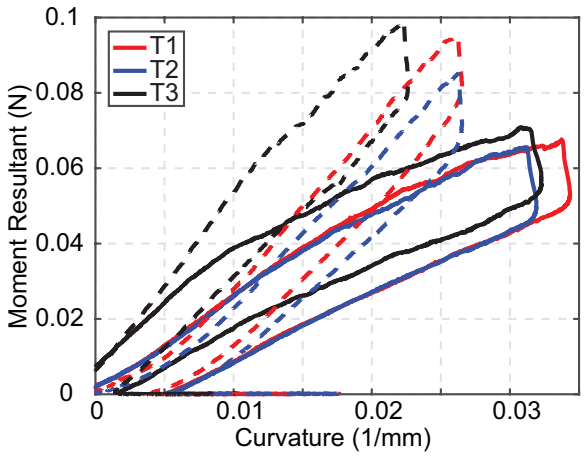

Figure 4.15: Bending stiffness of $[45/0/45]_{pw}$ AQ/silicone composite before folding (dashed lines) and after folding to 180° (solid lines)

4.9 Conclusion

This chapter outlined fabrication techniques used for dual-matrix composites. It was demonstrated that to prevent the flow of the low viscosity silicone past the hinges, it is critical to embed the epoxy matrix first which has a high viscosity at room temperature. Analysis of the matrix interface using nanoindentation tests revealed 0.5 mm transition regions and showed sharp changes of matrix stiffness across the interface, indicating that all polymers have been fully cured.

Furthermore, a detailed study of the microstructure of the AQ/epoxy and AQ/silicone composites was conducted using optical microscopy. The use of UV-cure silicone made it difficult for the silicone composite to be cured under very high pressures, resulting in a thicker composite with a looser weave. Most significantly, the ratio of thickness to the tow height of the silicone composite was much higher than the ratio for epoxy composites. This is a critical aspect to consider when modeling woven elastomer composites.

Finally, extensional and bending properties of the two composites were measured experimentally and compared to mosaic model predictions. The analytic approach yielded excellent predictions for in-plane stiffness of both composites. The agreement was best when loading in the fiber direction, with larger errors loading at 45°. In contract, the predictions for bending stiffness showed error as high as 100% relative to experimental measurements for both composites and highlight the need for an accurate homogenization model for predicting out-of-plane properties when experimental measurements are not feasible. The issue of softening in bending after folding to large curvatures was also addressed experimentally.

Chapter 5

Quasi-Static Deployment of Dual-Matrix Composite Hinges

In this chapter, a closed cross-section dual-matrix composite hinge is used as a means to study the quasi-static deployment mechanics of dual-matrix composites. This study develops a set of tools to examine the quasi-static deployment behavior experimentally, analytically, and through finite element simulations. The study is meant to enable the analysis of more complex structures such as booms, trusses, and even the antenna structure in Chapter 3. In particular, the analysis enables the design of deployment restraints for dual-matrix composites by developing the tools to predict deployment moments and folded shapes.

5.1 Dual-Matrix Hinge

5.1.1 Hinge Geometry

A schematic of the hinge is shown in Figure 5.1. The hinge is composed of a cylindrical fiber reinforced polymer composite tube of diameter, D, and length, L, with two diametrically opposite elastomer composite strips of width, h_c, along the length. The hinge can be folded by means of a single fold with an angle, θ, as illustrated in Figure 5.1B. Slots of length, w_s, are introduced into the elastomer composite strips to alleviate stresses in the fold region where high Gaussian curvature are introduced in the small region where the longitudinal folds meet with the transverse fold.

5.1.2 Hinge Fabrication

The geometry of the particular hinge prototypes in this study is summarized in Table 5.1. The hinges are fabricated from the same AQ fibers and epoxy and silicone matrices as outlined in Chapter 4. Tables 4.1 and 4.2 summarize the constituent material properties. The hinge has a 3-ply quasi-isotropic layup of $[45/0/45]_{pw}$.

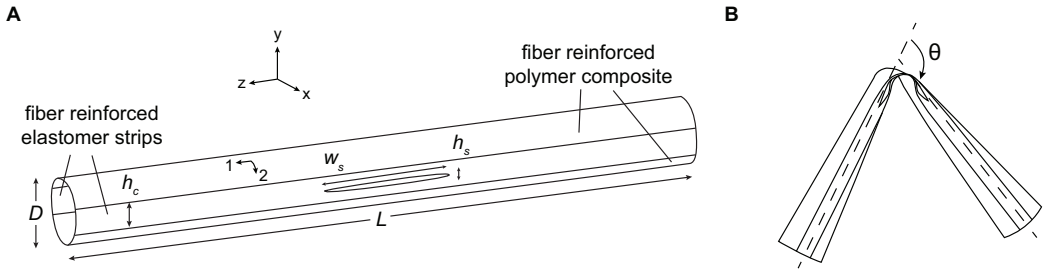

Figure 5.1: Geometry of dual-matrix hinges (A) definition of hinge geometric parameters (B) illustration of hinge folding

	L	D	h_c	h_s	w_s
Value	250	25.4	8	2	0, 10, 40, 50

Table 5.1: Values for hinge geometric parameters, units are mm

The fabrication process of the hinge prototypes is analogous to that of the antenna in Section 4.3. The only change is the omission of a conductor at the midplane of the layup and the used of heat shrink tubing over the hinge layup prior to vacuum bagging to prevent wrinkles in the hinge. Figure 5.2 shows the fabricated hinge prototypes with various slot lengths.

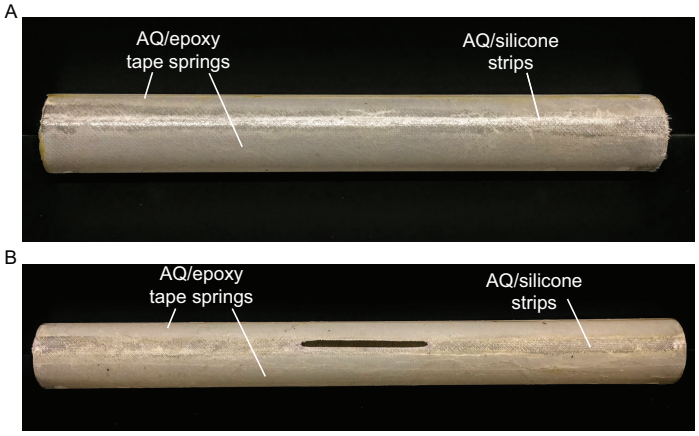

Figure 5.2: Fabricated dual-matrix hinges (A) hinge with no slot (w_s = 0 mm) (B) hinge with a w_s = 50 mm slot

5.1.3 Composite Stiffness

Accurate values of the composite thickness and fiber volume fractions were obtained from optical micrographs presented in Chapter 4. This ensured good estimates of the stiffness of the composites.

The deployment of dual-matrix composites is driven by the strain energy stored upon folding of the structure. Hence, an accurate constitutive model for the composites used is required for predicting deployment moments of the hinge. The composite stiffness is characterized by the ABD matrix

(Equation 4.12), and can be computed for a woven reinforcement using CLT and the mosaic model as described in Section 4.6. Comparison of these predictions to experimental data in Section 4.8 has shown that prediction of the in-plane stiffness, $\boldsymbol{A}$, is very accurate for woven composites, whereas prediction of the out-of-plane stiffness, $\boldsymbol{D}$, shows very large errors.

Hence, the axial stiffness matrix, $\boldsymbol{A}$, in the local coordinate frame indicated by axes 1 and 2 in Figure 5.1A are predicted using mosaic theory and are given by,

$$\boldsymbol{A_e} = \begin{bmatrix} 3696 & 1228 & 0 \\ 1228 & 3696 & 0 \\ 0 & 0 & 1332 \end{bmatrix} \text{ N/mm} \tag{5.1}$$

$$\boldsymbol{A_s} = \begin{bmatrix} 1867 & 866 & 0 \\ 866 & 1867 & 0 \\ 0 & 0 & 860 \end{bmatrix} \text{ N/mm} \tag{5.2}$$

where the e and s subscripts indicate AQ/epoxy and AQ/silicone composite properties, respectively.

The bending stiffness in the axial direction of the hinge was measured using four-point bending tests in Section 4.8. Furthermore, experimental studies on the bending of silicone reinforced composites have shown a significant decrease in the bending stiffness occurring when folding to large curvatures as a result of fiber microbuckling [13]. The post-buckling stiffness was measured in Section 4.8.1 for the hinge layup, showing that it is only 40% of the original. As a result, the bending stiffness of the silicone composite in the circumferential direction of the hinge, D_{22}, is reduced compared to that in the axial direction, D_{11}, to account for the high curvature of the material in that direction (illustrated in Figure 5.1B).

The remaining coefficients of the bending stiffness matrices not measured experimentally, were predicted by the mosaic model and scaled by $D_{11,exp}/D_{11,mm}$, where the exp and mm subscripts indicate measured values and mosaic model predictions, respectively. The bending stiffness for the two composites is given by,

$$\boldsymbol{D_e} = \begin{bmatrix} 12.31 & 5.25 & 0 \\ 5.25 & 12.31 & 0 \\ 0 & 0 & 7.30 \end{bmatrix} \text{ N} \cdot \text{mm} \tag{5.3}$$

$$\boldsymbol{D_s} = \begin{bmatrix} 3.61 & 1.34 & 0 \\ 1.34 & 1.45 & 0 \\ 0 & 0 & 2.46 \end{bmatrix} \text{ N} \cdot \text{mm} \tag{5.4}$$

Due to the symmetric layup of the composite, the stretch-bending coupling, $\boldsymbol{B}$, is zero.

5.1.4 Analytic Model

A simple model of two AQ/epoxy tape springs that are connected at the edges and are assumed to bend together is used to gain insight into the deployment behavior of the dual-matrix hinge. A single tape-spring has the geometry in Figure 5.3A. The tape-spring can be folded either in equal- or opposite-sense bending, as illustrated in Figure 5.3B and C, respectively.

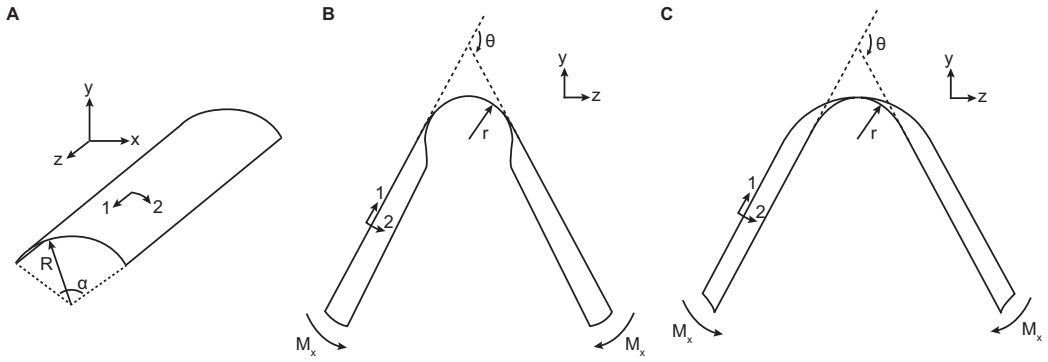

Figure 5.3: (A) single tape spring geometry (B) equal-sense bending (C) opposite-sense bending.

For small relative rotation angles, θ, the reaction moment, M_x, increases linearly until the tape spring buckles to form a localized fold. Past this angle, the tape-spring produces a constant reaction moment. The response is similar for both equal- and opposite-sense bending, but equal-sense bending results in lower reaction moments [57, 58]. This behavior is illustrated in Figure 5.4A, where the *es* and *os* subscripts indicate equal- and opposite- sense bending, respectively.

The mechanics of two connected tape-springs, one undergoing equal- and one opposite-sense bending, are analogous and can be predicted through superposition of the separate cases considered above. However, due to the connection between the two tape-springs, the folding angle of the outer tape spring is less than that of the inner tape spring during folding. Therefore, two distinct moment peaks are expected with the inner tape-spring buckling first upon folding. The response should be identical in either direction of folding of the hinge. This behavior is illustrated in Figure 5.4B.

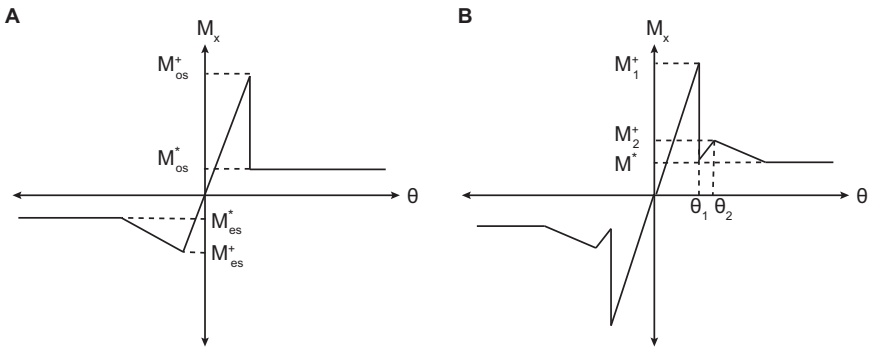

Figure 5.4: Predicted reaction moments (A) single tape-spring (B) combination of two tape-springs.

The mechanics of tape-springs can be analyzed using an energy approach [59], for which the fold radius of a single or two unconnected tape springs can be achieved. Here, the analysis is extended to consider the energy contribution of the AQ/silicone strips. Only the bending energy in the fold region of the hinge is considered, as the energies in the transition regions are independent of the fold radius.

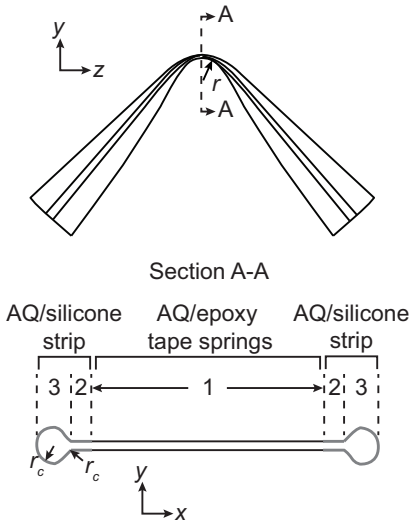

Figure 5.5: Cross-section of fold area of dual-matrix hinge.

The folded shape of the dual-matrix hinge has been sketched in Figure 5.5, with the cross-section at the fold region shown in the lower part of the figure. This cross-section can be divided into 3 regions: the flattened AQ/epoxy tape springs, the flattened portions of the AQ/silicone strips, and the approximately circular AQ/silicone connections at the end of radius r_c. In region 3, we assume that $r_c = 0.5t$ due to self-contact of the material, where t is the thickness of the material. Due to very high curvatures in the circumferential direction, the fibers microbuckle resulting in increased material thickness in region 3, forming a circular cross-section. We consider contributions to the bending strain energy from the deformation in regions 1 and 3. Region 2, as well as the transition between regions 2 and 3, are comparatively small and their contribution to the energy is neglected.

The AQ/epoxy tape-springs in region 1 undergo the following principal curvature changes,

$$[\boldsymbol{\kappa_e}]^T = [\Delta\kappa_{x,e} \ \Delta\kappa_{z,e}] = \left[\mp\frac{1}{r} \ \frac{1}{R}\right] \tag{5.5}$$

for opposite- and equal-sense bending respectively. The corresponding moments are given by,

$$[\boldsymbol{M_e}] = \begin{bmatrix} M_{x,e} \\ M_{z,e} \end{bmatrix} = \begin{bmatrix} D_{11,e}\kappa_{x,e} + D_{12,e}\kappa_{z,e} \\ D_{12,e}\kappa_{x,e} + D_{22,e}\kappa_{z,e} \end{bmatrix} \tag{5.6}$$

The total strain energy in the two AQ/epoxy tape-springs (region 1) is therefore,

$$U_1 = R\theta\alpha r[\boldsymbol{\kappa_e}]^T[\boldsymbol{M_e}] = \theta\alpha\left[\frac{RD_{11,e}}{r} + 2D_{12,e} + \frac{rD_{22,e}}{R}\right] \tag{5.7}$$

The AQ/silicone connections in region 3 undergo a large curvature change about the z-axis to form two cylindrical tubes of radius r_c connected to the edges of the AQ/epoxy tape-springs shown in Figure 5.5. Furthermore, these beams are curved around the x-axis to form the dual-matrix hinge fold region of radius r. For bending around the z-axis, the energy can be computed from the curvature changes,

$$\Delta\kappa_{z,s} = \left(\frac{1}{r_c} - \frac{1}{R}\right) \tag{5.8}$$

The energy contribution from this deformation is,

$$U_{3,z} = 2\pi r_c r\theta D_{22,s}\left(\frac{1}{r_c} - \frac{1}{R}\right)^2 \tag{5.9}$$

The AQ/silicone cylindrical shell in region 3 undergoes the same curvature change along the x-axis as the AQ/epoxy tape-springs,

$$\Delta\kappa_{x,s} = \frac{1}{r} \tag{5.10}$$

The moment per unit length of the fold can be computed from,

$$M_{x,s} = \frac{12(1-\nu_s^2)\kappa I}{2\pi r_c t_s^3} D_{11,s} \tag{5.11}$$

where $I = \pi/4[(r_c + t_s)^4 - r_c^4]$ is the area moment of inertia for a hollow circular tube, t_s is the thickness of the AQ/silicone composite, and ν_s is the Poisson's ratio of the AQ/silicone composite. In computing the moments, the bending stiffness for a quasi-isotropic AQ/silicone composite plate is used.

Hence, the total energy contribution from bending of the circular tube is,

$$U_{3,x} = \frac{12(1-\nu_s^2)\theta I D_{11,s}}{r t_s^3} \tag{5.12}$$

Adding the three energy contributions in Equations 5.7, 5.9, and 5.12 and minimizing with respect to the fold radius, r,

$$r = \sqrt{\frac{R\alpha D_{11,e} + [12(1-\nu_s^2)I/t_s^3]D_{11,s}}{[\alpha/R]D_{22,e} + 2\pi r_c(1/r_c - 1/R)^2 D_{22,s}}} \tag{5.13}$$

This equation is valid only for $D_{11,s} = D_{22,s}$ due to the assumption of a quasi-isotropic AQ/silicone layup. The use of this equation when $D_{11,s} \neq D_{22,s}$, for example to account for fiber microbuckling, can only be used to predict trends in the fold radius.

There are several insights to draw from Equation 5.13. First, if the bending stiffness of the AQ/silicone strips tends to zero (i.e., no connection between the two tape-springs), we recover the fold radius expected for two tape springs given in [59],

$$r = \sqrt{\frac{D_{11,e}}{D_{22,e}}} R \tag{5.14}$$

For a quasi-isotropic tape-spring layup, where $D_{11,e} = D_{22,e}$, as for the AQ/epoxy composite used here, this simplifies to the well known result [59],

$$r = R \tag{5.15}$$

Hence, for quasi-isotropic unconnected tape-springs the fold shape is entirely controlled by the tape-spring geometry and is independent of material properties.

Second, if we assume the material properties of the AQ/epoxy tape-springs to be fixed, chosen to control the overall stiffness of the structure, it is predicted that the fold radius of the dual-matrix hinge can be controlled by modifying the bending stiffness of the AQ/silicone strips. Increasing the bending stiffness, $D_{11,s} = D_{22,s}$, decreases the fold radius. Reducing the circumferential bending stiffness to account for fiber microbuckling, will result in a larger fold radius compared to the quasi-isotropic case. This is of significance, as the fold radius of the dual-matrix hinge can be controlled even with a quasi-isotropic layup for both composites, which is not possible for two unconnected tape springs as indicated by Equation 5.15.

The steady-state moment, M^*, for the dual-matrix hinge can be obtained by substituting Equations 5.5 and 5.13 into the x-component of Equation 5.6. By superposition, M^* is the sum of moments from one tape-spring undergoing equal-sense bending and the other undergoing opposite-sense bending. The moments imparted by the AQ/silicone connection have a negligible contribution to M^*.

5.1.5 Quasi-static Deployment Experiments

The hinge deployment was characterized experimentally by measuring the quasi-static reaction moment for varying fold angles, θ, with the experimental setup in Figure 5.6. A small section at each end of the hinge was attached rigidly to a thick cylindrical hub whose rotation was controlled via gears. One hub was fixed while the other was allowed to slide on a linear bearing. The moment response was measured using strain gages attached to each hub. The hinge was pinched by hand at the center, folded to $\theta = 100^o$, and then deployed in small steps. The moment was measured every 5^o for $40^o < \theta < 100^o$ and every 2^o for $\theta < 40^o$ to capture the peak moments.

The dependence of the moment on the fold angle of the hinge is shown in Figure 5.7 for several

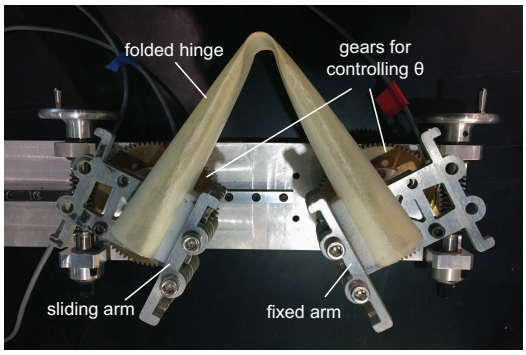

Figure 5.6: Experimental setup used to measure the moment response of the hinge during deployment

slot lengths, w_s. The experimental error stemming from the resolution of the strain gages is shown only for the case of w_s = 50 mm, for clarity. Qualitatively, the response for all w_s matches well the theoretical prediction illustrated in Figure 5.4B. Instead of the two distinct deployment peaks a broad region of increased moment for $\theta < 40^o$ is observed. This is due to the tendency of the hinge to self deploy, making it difficult to capture the exact moment peak experimentally. Furthermore, $M_x > 0$ for all θ indicating that the hinge can self-deploy.

No correlation between the slot length and the deployment moments is observed. This can be expected as the deployment moment is driven mostly by the strain energy stored in the AQ/epoxy tape springs as the AQ/silicone strips are much softer and smaller in extent. The measured steady state moment, defined experimentally as the average moment for $40^o < \theta < 100^o$, is between 40–50 N·mm, a good agreement with M^* = 47.7 N·mm predicted using Equations 5.5, 5.6, and 5.13. The 15% variation in peak moments between hinges with different slot lengths arises as it is difficult to maintain the hinge in its configuration just before snap back. Any remaining deviations are due to statistical variations in material properties and the fabrication process, as a similar variation was observed during testing of multiple samples with the same slot length.

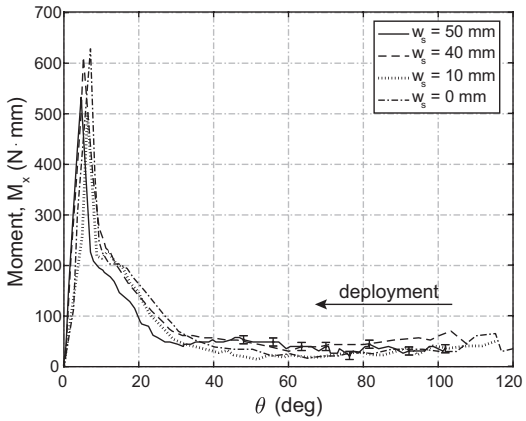

Figure 5.7: Experimentally measured moment response during deployment of hinges with various slot lengths

To further characterize the deployment behavior, the folded shape was measured as a function of the fold angle using digital image correlation (DIC) for the hinge with $w_s = 0$ mm. The setup is illustrated in Figure 5.8. A pair of Grasshopper 50S5M-C cameras from Point-Grey Research with Xenoplan f/1.9-35 mm lenses from Schneider-Kreuznach were positioned 50 cm from the hinge to measure the shape of the fold region in the outer tape spring. The stereo angle was set at 40° to minimize the correlation error for a 35 mm lens [60]. A narrow f/16 aperture was used to achieve a focused image across all θ. The strains and curvatures during deployment were computed using the Vic3D software from Correlated Solutions.

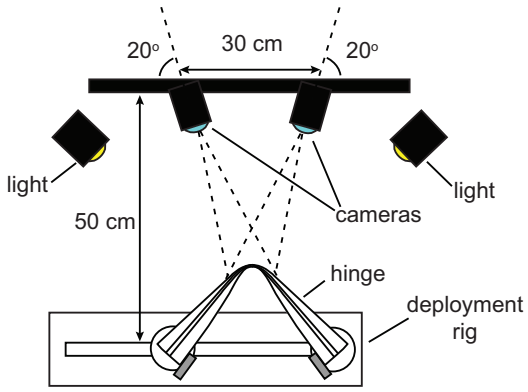

Figure 5.8: Experimental DIC setup for metrology of folded hinge shape

Plots of the longitudinal radius of curvature at different fold angles are shown in Figure 5.9 for the hinge with $w_s = 0$ mm. The fold radius was computed by averaging the radius of curvature in a 12×5 mm^2 region centered on the apex of the fold (Figure 5.10). It can be seen that a steady-state fold radius of 10.0 mm is approached at high angles. As predicted by the model developed in Equation 5.13, the addition of the silicone strips connecting the quasi-isotropic AQ/epoxy tape springs lowers the fold radius from that for two unconnected AQ/epoxy tape-springs of $r = 12.7$ mm (Equation 5.15). The effects of the AQ/silicone strip bending stiffness are further studied via finite element simulations in Section 5.3.2.

5.2 LS-Dyna Finite Element Simulations

The application of dual-matrix composites to space structures requires reliable and efficient simulation techniques for predicting the deployment behavior of these structures. In particular, quasi-static simulations can yield deployment moments to be used in the design of the deployment restraints for more complex structures. Previous studies have developed simulation techniques for deployable composite booms with an open cross-section [36, 61], booms with cutouts in the fold region to make localized hinges [33, 35], and booms with a fully closed cross-section [62, 63]. Explicit solvers have been used to avoid convergence issues associated with modeling large deformation in thin shells using

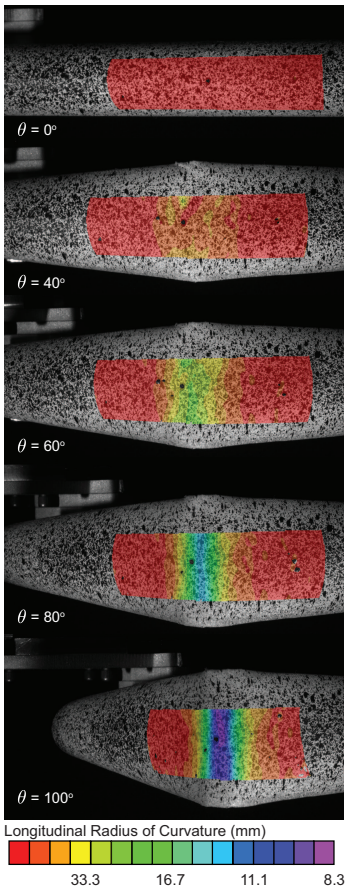

Figure 5.9: Longitudinal radius of curvature of outer tape-spring of dual-matrix hinge with w_s = 0 mm, for several deployment angles

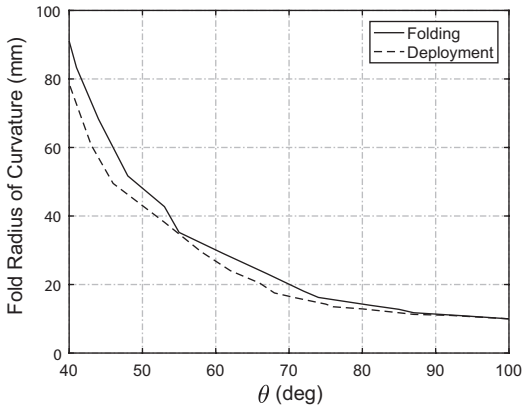

Figure 5.10: Longitudinal fold radius for dual-matrix hinge with $w_s = 0$ mm

shell elements, resulting in high computational costs to obtain quasi-static solutions. Solutions via implicit solvers for quasi-static deployment have been limited to boom geometries with large slots or open cross-sections.

Preliminary studies of the deployment of dual-matrix hinges were done using the Abaqus/Explicit

finite element code in [63, 64]. However, a detailed investigation of the material properties of the dual-matrix composites was not done during those studies, resulting in large discrepancies between simulations and measurements. Previous work by the present authors found extreme sensitivity of the solution to numerical parameters such as damping, making it difficult to obtain accurate quasi-static results [64]. Furthermore, high frequency oscillations were observed in the reaction moments despite numerical damping and required filtering [63, 64].

In this study, LS-Dyna was chosen for modeling the deployment of the dual-matrix hinge because of its robust contact algorithms and good stability for highly non-linear problems. LS-Dyna is primarily an explicit finite element code; recently implicit analysis capabilities were extended to composite materials and thin shell elements. Explicit solvers are advantageous due to their ability to handle non-linearities, such as contact and material non-linearities, without convergence problems more easily than implicit solvers. However, care must be taken to ensure accuracy of the explicit results as equilibrium is not enforced at each step of the solution. Both explicit and implicit modeling techniques were investigated in the present study, as detailed in the rest of this section. The respective advantages of the two techniques are compared in Section 5.3.1.

5.2.1 Finite Element Model Description

The hinge was modeled with the type 16 shell element in LS-Dyna, a 4 node fully integrated element modeling the mid-plane of the material based on the Reissner-Mindlin kinematic assumption. The element size was 0.75 mm in the fold region and 3 mm in the rest of the model, resulting in approximately 15,000 elements. The stiffness of the two composite materials was defined via a linear elastic laminated plate material model, `*MAT_117-Composite_Matrix`, which allows direct input of the ABD matrix as specified in Section 5.1.3. This avoids inaccuracies associated with CLT when predicting out-of-plane stiffness of woven composite materials. Furthermore, this facilitates an investigation of the effect of the material properties of the hinge on the deployment. Finally, frictionless contact between all surfaces in the simulation was defined using the keyword `*Contact_Automatic_Single_Surface`, a general 3D contact algorithm. This algorithm accounts for the thickness of the shell and uses a penalty formulation to enforce contact constraints. The model is shown in Figure 5.11.

The model included three steps: folding, stabilization, and deployment. To fold the hinge, a pressure of 12.5 Pa was applied in the fold area to pinch the shell, followed by opposing rotations of 1.5 rad applied to rigid patches at the two ends of the hinge with the pressure gradually removed. The rigid patches matched those in the experiments in Section 5.1.5, and are constrained using the keyword `*Constrained_Nodal_Rigid_Body`. The stabilization step, only required in the explicit model, was used to obtain a static, stable folded configuration. In the deployment step, the rotations at the rigid patches were reversed to slowly deploy the hinge.

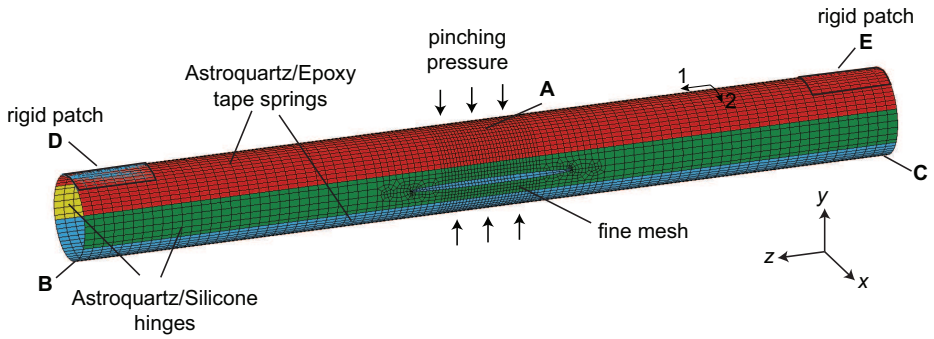

Figure 5.11: LS-Dyna model of the dual-matrix hinge

5.2.2 Quasi-Static Simulations with an Explicit Solver

Explicit solvers use the full dynamic equations of motion and therefore, to carry out a quasi-static analysis, the applied velocities must be kept as low as possible. As a general heuristic, the kinetic energy is kept at $< 1\%$ of the internal energy for all parts of the simulation where a quasi-static result is required [35]. In this study, the kinetic energy in the system was controlled through the loading rates and numerical damping. More gradual loading rates and damping both result in lower velocities while damping also smooths instabilities. The selection of these two parameters influences the stable time increment used by the solver and hence directly impacts the overall computational time.

In LS-Dyna Explicit, two forms of numerical damping can be applied: global damping and bulk viscosity. Using global damping (`*Damping_Global` keyword), the accelerations at each node are computed by introducing a mass, m, and velocity, $\boldsymbol{v}$, proportional force to the force balance,

$$\boldsymbol{a} = \boldsymbol{M}^{-1}(\boldsymbol{F}^{ext} - \boldsymbol{F}^{int} - \boldsymbol{F}^{damp}) = \boldsymbol{M}^{-1}(\boldsymbol{F}^{ext} - \boldsymbol{F}^{int} - D_s m\boldsymbol{v}) \tag{5.16}$$

where $\boldsymbol{a}$ is the nodal acceleration, $\boldsymbol{M}$ is the mass matrix, $\boldsymbol{F}^{ext}$, $\boldsymbol{F}^{int}$ and $\boldsymbol{F}^{damp}$ are the external, internal, and damping force vectors, respectively, and D_s is the damping constant [65]. The LS-Dyna manual recommends a damping constant close to twice the natural frequency, ω_0, to damp out significant dynamic response at system resonance frequencies. In practice, the amount of damping should be as small as required to prevent a dynamic response. Large values of D_s will result in an over-damped response that is potentially inaccurate.

A second type of stabilization is achieved through bulk viscosity (`*Control_Bulk_Viscosity` keyword) where a viscous pressure term, q, is added to smooth out discontinuities,

$$q = \begin{cases} \rho l(Q_1 l\dot{\varepsilon}_{kk}^2 - Q_2 a\dot{\varepsilon}_{kk}) & \dot{\varepsilon}_{kk} < 0 \\ 0 & \dot{\varepsilon}_{kk} \geq 0 \end{cases} \tag{5.17}$$

where Q_1 and Q_2 are the quadratic and linear bulk viscosity coefficients, $\dot{\varepsilon}_{kk}$ is the rate of change of the volumetric strain, l is the characteristic length of the element, and a is the speed of sound [65].

The magnitude of numerical damping will influence the stable time increment for the simulation. The Courant stability condition indicates that in explicit analysis the time step should not exceed the time it takes for a wave to travel across an element,

$$\Delta t_{crit} = \frac{l}{c}\left(\sqrt{1+\zeta^2} - \zeta\right) \tag{5.18}$$

where c is the wave speed, and $\zeta = D_s/(2m\omega)$ is the fraction of critical damping [65]. It can be seen that increasing damping will reduce the stable time increment.

5.2.3 Explicit Model Parameter Selection

Simulation Phase	D_s (rad/s)	Time (s)	Boundary Conditions A	B	C	D	E
Folding	5	0.6	$u_x = u_y = u_z = 0$	$u_x = 0$	$u_x = 0$	$\theta_x = -1.5$ rad	$\theta_x = 1.5$ rad
Stabilization	75	0.25	$u_x = 0$	none	none	$u_x = u_y = u_z = 0$ and $d\theta_x/dt = 0$	$u_x = u_y = 0$ and $d\theta_x/dt = 0$
Deployment	50	4	$u_x = 0$	none	none	$u_x = u_y = u_z = 0$ and $d\theta_x/dt = 1.5$ rad	$u_x = u_y = 0$ and $d\theta_x/dt = -1.5$ rad

Table 5.2: Simulation parameters for explicit model

The explicit model consisted of the folding, stabilization, and deployment steps with full restarts between each simulation step. The restarts were required as the boundary conditions to obtain the folded shape were selected to minimize numerical damping and hence reduce the computation times but do not match those of the deployment experiments in Section 5.1.5. The model boundary conditions and parameters are summarized Table 5.2, where the boundary condition regions correspond to those defined in Figure 5.11.

Global mass damping and bulk viscosity are used to stabilize all steps of the simulation. The fundamental frequency of the hinge is 1281 rad/s and hence the recommended damping constant is $D_s = 2562$ rad/s. However, in practice it was found that this value is orders of magnitude too high, a common trend when running quasi-static simulations using explicit dynamics [35]. The damping values were chosen such that the response of the hinge is critically damped and the kinetic energy during deployment is $< 1\%$ of the internal energy. Furthermore, the time step chosen for explicit analysis was set at $dt = 7.9 \times 10^{-8}$ s to satisfy the Courant condition.

5.2.4 Implicit Model Parameter Selection

Implicit models solve the static force balance by inversion of the stiffness matrix and hence they satisfy equilibrium at each increment. Instabilities and contact can cause singularities in the stiffness matrix and make convergence difficult. There is no numerical damping required in these simulations, although artificial stabilization can be used to improve convergence [65]. No stabilization was required for this model. The stable increment in implicit analysis is several orders of magnitude larger than in explicit analysis and is often limited by the contact algorithm.

The boundary conditions of the implicit model were identical to those of the deployment step (and experiments) in Table 5.2. No restarts were required and the hinge was folded and deployed in a single analysis step. Static implicit analysis was enabled by including the `*Control_Implicit_General` keyword. Non-linear analysis is used to account for geometric non-linearities. The folding and deployment was done over 4.85 s with the increment set to $dt = 5.0 \times 10^{-5}$ s, allowed to vary automatically between $dt/1000 < dt < 10dt$. This increment was found to be the maximum for which convergence could be achieved. Note that the times here have no physical significance and are instead representative of the load increments used in the simulation.

Contact in implicit analysis in LS-Dyna is by default 'sticky' i.e., once contact has occurred, a large penalty is applied to keep the parts in contact. This prevents the parts from coming in and out of contact and causing instabilities in the analysis. This behavior is controlled by the `IGAP` parameter of the contact algorithm and can be turned off by changing the parameter from 1 to 2 to disable the contact penalty. Alternatively, the `SFS` parameter can be modified to scale the penalty.

The contact parameters were tuned to compute an accurate folded shape for the hinge. With the default 'sticky' contact, the two tape springs remained in contact and would not deploy, resulting in an inversion in the sign of longitudinal curvature in the outer tape spring (Figure 5.12A). Selecting `IGAP` = 2 to disable the contact penalty resulted in contact constraint violations at the tape spring edges unless the time increment was significantly reduced (Figure 5.12B). To enable larger increments, the `SFS` parameter was scaled down to `SFS` = 0.01, reducing the contact penalty to 1% of its original value. This setup prevented contact failure while allowing larger time increments and reducing 'sticky' contact enough to allow tape spring deployment (Figure 5.12C).

5.3 Finite Element Results and Discussion

5.3.1 Comparison of Models

The most notable difference between the explicit and implicit models is the value of the stable increment used in the simulations. The explicit model had an increment of $dt = 7.9 \times 10^{-8}$ s whereas the implicit model had an average increment of $dt = 5.0 \times 10^{-5}$ s, three orders of magnitude larger.

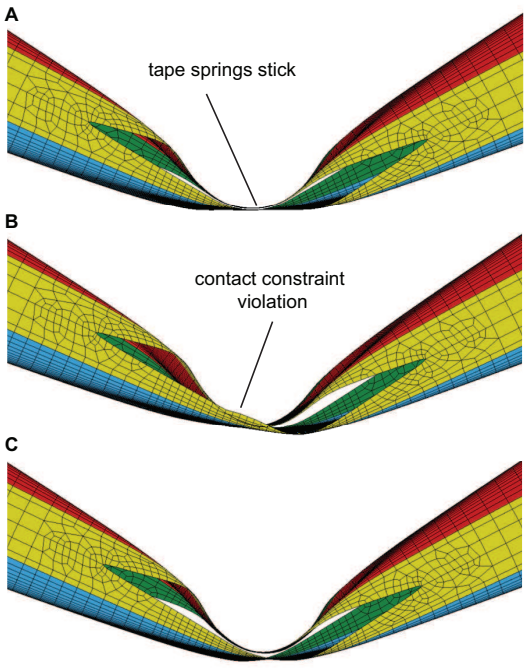

Figure 5.12: Effects of contact penalty on deployed shape at $\theta = 60^o$of the hinge with $w_s = 50$ mm (A) LS-Dyna defaults - 'sticky' contact (B) `IGAP` = 2 – 'sticky' contact disabled (C) `SPS` = 0.01 – contact penalty reduced to 1%

This resulted in a large difference in the runtime of the models. Despite using restarts to speed up explicit analysis, the three analysis steps needed to fold and deploy the hinge with $w_s = 50$ mm with an explicit solver took 35.17 hours on 8 cores (Intel Xeon X5680 CPU) whereas the implicit solver took only 1.01 hours on 8 cores.

Previous attempts by the authors to model this problem with the Abaqus/Explicit code revealed strong dependence of the simulation results with numerical damping [64]. The explicit model here was significantly more stable and required less tuning of the damping parameters. No filtering of the reaction moments was required to remove high-frequency oscillations. Convergence using implicit solvers in Abaqus was not successful for this problem but was achieved without stabilization in LS-Dyna.

Unless otherwise stated, implicit model results are reported for the folded shape of the hinge and the reaction moments during deployment. The explicit model results are in good agreement for all cases.

5.3.2 Folded Hinge Shape

From the analytical prediction with Equation 5.13, it is expected that, for fixed AQ/epoxy material properties, the bending stiffness of the AQ/silicone strips will have a significant impact on the overall

fold radius of the dual-matrix hinge, r. Hence, an investigation was conducted on the hinge with $w_s = 0$ mm where the bending stiffness of the AQ/silicone composite was varied through numerical simulations. Figure 5.13A illustrates the resulting steady-state fold radii for several values of the stiffness, assuming a quasi-isotropic layup where $D_{11,s} = D_{22,s}$. The finite element simulations show good agreement with the analytical predictions (using $r_c = 0.35$ mm for the radius of the AQ/silicone tubes formed during transverse flattening of the hinge). It can be seen that reducing the bending stiffness of the connection between the tape springs increases the fold radius of the hinge. This demonstrates that the AQ/silicone connections can be used to tune the fold radius even for quasi-isotropic layups for both composites, as predicted in Section 5.1.4.

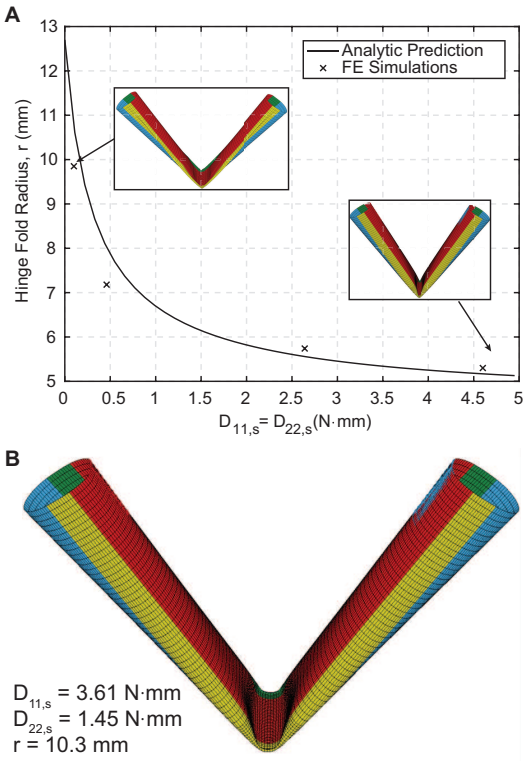

Figure 5.13: Comparison of analytic prediction of dual-matrix hinge fold radius and finite element simulation

In Figure 5.13B, the bending stiffness matches the experimental values where $D_{22,s} = 1.45$ N·mm is reduced to 40% of $D_{11,s} = 3.61$ N·mm to account for microbuckling of the fibers, as discussed in Section 5.1.3. This is the only case for which the hinge shape shows a smooth fold with no sharp kinks in the AQ/silicone strips. Furthermore, the fold radius of 10.3 mm obtained through simulation is in excellent agreement with the value $r = 10.0$ mm measured experimentally (3% error). Applying the model in Equation 5.13, a fold radius of $r = 8.2$ mm is predicted for the case of $D_{11,s} \neq D_{22,s}$. Comparing this value to the $r = 5.3$ mm prediction for the quasi-isotropic case $D_{11,s} = D_{22,s}$, it can be seen that the model predicts the increase in fold radius due to microbuckling

observed experimentally. However, the model results in an 18% error from the experimental value of r = 10.0 mm. This is to be expected as the model assumes quasi-isotropic properties.

5.3.3 Deployment Moments

Figure 5.14 shows the deployment moments for implicit and explicit simulations compared to experimental results for the hinge with w_s = 50 mm. Furthermore, Table 5.3 summarizes key deployment moment values for the three cases. Both implicit and explicit solvers predict the experimental behavior well with the steady state moments within experimental error. The simulations show two distinct peaks corresponding to the deployment of the two tape springs as predicted in Figure 5.4B in Section 5.1.4. The peak moments predicted in simulation are larger than measured. Experimentally, the hinge tends to self deploy and hence a lower peak moment is measured. Furthermore, the significant difference between peak moments from the two simulations is due to the smaller time step, and hence finer load increments, of the explicit simulation allowing it to provide a finer angular resolution.

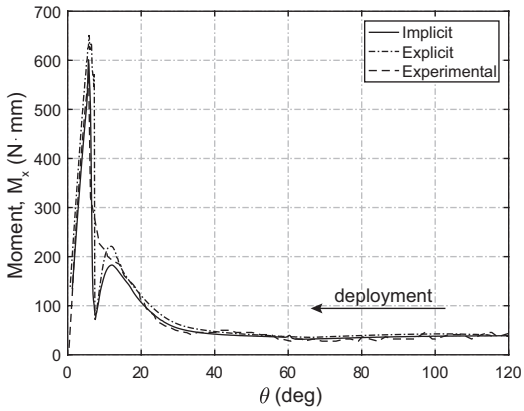

Figure 5.14: Comparison of finite element simulation and experimental results for a hinge with a 50 mm slot

	Implicit Solver	**Explicit Solver**	**Measurement**
M^* **(N·mm)**	41	45	43
M_1^+ **(N·mm)**	596	726	564
θ_1 **(deg)**	5.6	7.3	5.7

Table 5.3: Summary of key values of deployment response of hinge with w_s = 50 mm.

Figure 5.15 shows the dependence of the deployment moment on w_s in the implicit simulations. The same trend is seen for the explicit simulations. A comparison with Figure 5.7 shows that the simulations predict a much higher dependence of the moment on the slot length than is observed experimentally. Reducing the mesh size in the fold region, or reducing the transverse bending stiffness of the silicone composite, D_{22}, does not resolve the discrepancy. The higher moments seen

in simulation are attributed to the fully integrated elements used being too stiff when doubly curved. An investigation of the dependence on element type is beyond the scope of the present study. The model with w_s = 50 mm can be used to predict the deployment moments of hinges without slots, as experimentally there is little dependence on w_s.

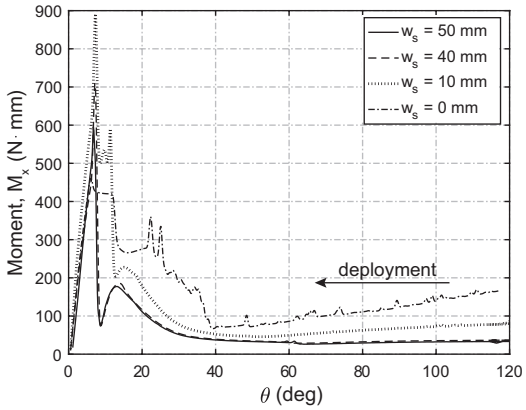

Figure 5.15: Dependence of deployment moment on the slot length in simulation - implicit model

5.3.4 Torsional Behavior

The closed cross-section of the dual-matrix hinges can provide superior torsional behavior compared to open cross-section booms such as the TRAC and STEM booms. However, the introduction of small slots in the AQ/silicone fold region, to remove the doubly-curved region and alleviate stresses, can have a significant effect on the torsional stiffness. The torsional behavior of the hinge was simulated in LS-Dyna implicit with the Ricks and Wempner arc-length method to capture the post-buckling response. The same hinge model as for folding was used. The hinge was clamped at one end and a rotation, ϕ, was applied around the z-axis of the hinge at the other.

Figure 5.16 shows the dependence of the torsional stiffness on w_s, where G is the shear modulus and J is the torsion constant. It can be seen that introducing small slots has a negligible effect, with w_s = 10 mm reducing the torsional stiffness by only 8%. However, for longer slots the torsional stiffness decreases more quickly. Hence, introducing a small 10 mm slot is a good way of alleviating stresses in dual-matrix hinges while maintaining their superior torsional behavior.

5.4 Conclusion

Dual-matrix composite shells have been proposed as a means of realizing stiff, lightweight structures capable of accommodating packaging schemes with small fold radii through the use of localized elastomer composite hinges. Previous research has focused on the elastomer composite constitutive modeling or on proof-of-concept studies of folding of dual-matrix structures. This chapter presented

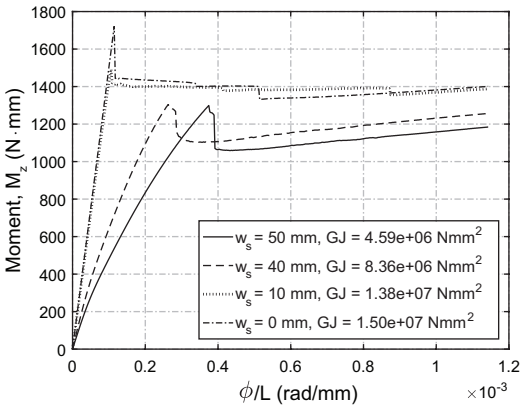

Figure 5.16: Simulated torsional stiffness of hinges with various slot widths

a more detailed look at the deployment mechanics of a simple closed cross-section dual-matrix hinge which can be used as a building block for more complex deployable structures.

This study focused on characterizing the quasi-static deployment behavior of the proposed building block in terms of its folded shape and deployment moments. These parameters are critical to the design of deployment mechanisms for dual-matrix structures. The hinge was studied using an analytic minimum energy approach, experimental deployment tests, and finite element simulations – with good agreement between all models. The radii of the localized fold in the hinge could be predicted within 3% of experimental measurements while the steady-state reaction moments of the hinge could be predicted within 5% of measurements. This suite of analysis tools can be used to investigate booms, truss structures, and large cylindrical and conical shells made of dual-matrix composites.

In addition to the development of analysis techniques for deployment of dual-matrix shells, this work also identified several interesting aspects of the behavior of these composites. As these structures rely on stored strain energy for deployment, the importance of using accurate material properties was demonstrated. In particular, the bending stiffness of the shells has a large impact on deployment moments and folded shape. It was found that the transverse bending stiffness of the elastomer composite must be reduced by as much as 60% to experimentally measured stiffnesses at high laminate curvatures to account for fiber microbuckling. Furthermore, the use of the elastomer composites to tailor the fold radius of the hinge was demonstrated, a behavior not possible with simple quasi-isotropic tape springs. It was shown that the addition of elastomer hinges reduces the localized fold radius from that of unconnected tape-springs. This shows the versatility of the hinge building block to meet various packaging requirements independent of the overall stiffness of the structure. Finally, techniques for simulation of this deployment problem using the LS-Dyna commercial software were developed, taking advantage of the robust restart capabilities and the stabilization of the contact algorithms to improve computational times. The implicit solver showed

a reduction in run times by a factor of 30 over the more commonly used explicit solver.

Although the finite element simulation techniques presented here proved very accurate for predicting the deployment moment for dual-matrix hinges with small slots, issues with the shell elements were highlighted when used for simulating doubly curved regions. A study of element types appropriate for high Gaussian curvatures is suggested as a follow-on study to this work. Of particular interest is the application of continuum shells with thickness stretch and multiple through-thickness integration points to this problem.

Chapter 6

Semi-Empirical Models for Stiffness of Plain-Weave Composites

6.1 Introduction

Comparison of experimental measurements of the stiffness of woven composites to mosaic theory predictions, a commonly used analytic approach, in Section 4.8 revealed large discrepancies, particularly for the bending stiffness of woven composites. The model's neglect of the undulations in the composite tows is the source of these discrepancies. In reality, the undulating tows straighten in response to loading of the laminate and are under combined axial and bending strains, resulting in very different stiffness than for straight fibers.

Experimental measurements of composite stiffness can be done to obtain accurate results, as was done in Chapter 4. This approach was sufficient to characterize antenna and hinge performance in the previous Chapters. However, experimental measurements of the stiffness are not always feasible, particularly at the design stage where a large number of design iterations is required and an estimate of the stiffness is required for an idea of how the structure will behave. Another example is the prediction of viscoelastic properties over long storage times as experimental measurements become very time consuming. The later example is the application of interest in Chapter 7. Hence a more accurate model of woven composites is required starting with the prediction of elastic properties which can be extended to viscoelasticity. This issue has been addressed in literature for epoxy composites but little data exists for woven elastomer composites. Typical models consists of two levels of homogenization: the tow and the weave. The microstructure of these two was described in detail in Section 4.5.

In this chapter, existing models for homogenization of woven epoxy composites are applied to the silicone composite used in the dual-matrix structures in this work. It is found that existing

analytic and finite element techniques for homogenization of the tows underpredict tow stiffness by hundreds of percent. The sensitivity of the composite stiffness to model parameters is explored in this study. In particular, sensitivity of the tow stiffness to the semi-empirical Halpin Tsai model parameters as well as to the finite element weave geometry is investigated. A modified Halpin-Tsai approach where predictions of tow stiffness are supplemented by experimental data is proposed to improve predictions of woven stiffness of arbitrary elastomer composite layups. The model is also shown to be applicable to traditional epoxy composites.

6.2 Tow Homogenization Models

The goal of the tow homogenization is to compute the transversely isotropic tow stiffness matrix, $\boldsymbol{S}$, given by,

$$\begin{pmatrix} \sigma_{11} \\ \sigma_{22} \\ \sigma_{33} \\ \sigma_{23} \\ \sigma_{12} \\ \sigma_{13} \end{pmatrix} = \begin{bmatrix} S_{11} & S_{12} & S_{12} & 0 & 0 & 0 \\ S_{12} & S_{22} & S_{23} & 0 & 0 & 0 \\ S_{12} & S_{23} & S_{33} & 0 & 0 & 0 \\ 0 & 0 & 0 & S_{44} & 0 & 0 \\ 0 & 0 & 0 & 0 & S_{55} & 0 \\ 0 & 0 & 0 & 0 & 0 & S_{55} \end{bmatrix} \begin{pmatrix} \varepsilon_{11} \\ \varepsilon_{22} \\ \varepsilon_{33} \\ \varepsilon_{23} \\ \varepsilon_{12} \\ \varepsilon_{13} \end{pmatrix} \tag{6.1}$$

where 1 is the fiber direction, directions 2 and 3 are transverse to the fibers, ε_{ij} are the strains, and σ_{ij} are the stresses. In this case, there are only 5 independent constants as $S_{44} = 0.5(S_{22} - S_{23})$.

There are three common approaches to composite tow homogenization seen in literature: analytic, representative volume element (RVE) modeling with uniform fiber distributions, and RVE modeling with random fiber distributions. In the analytic approach, the stiffness matrix is found through inversion of the compliance matrix, $\boldsymbol{C}$. For the transversely isotropic case,

$$\boldsymbol{C} = \begin{bmatrix} \frac{1}{E_1} & -\frac{\nu_{12}}{E_1} & -\frac{\nu_{12}}{E_1} & 0 & 0 & 0 \\ -\frac{\nu_{12}}{E_1} & \frac{1}{E_2} & -\frac{\nu_{23}}{E_2} & 0 & 0 & 0 \\ -\frac{\nu_{12}}{E_1} & -\frac{\nu_{23}}{E_2} & \frac{1}{E_2} & 0 & 0 & 0 \\ 0 & 0 & 0 & \frac{1}{G_{23}} & 0 & 0 \\ 0 & 0 & 0 & 0 & \frac{1}{G_{12}} & 0 \\ 0 & 0 & 0 & 0 & 0 & \frac{1}{G_{12}} \end{bmatrix} \tag{6.2}$$

where, E_1 and E_2 are the tow Young's moduli in and transverse to the fiber direction, respectively, ν_{12} and ν_{23}, are the Poisson's ratios parallel and transverse to the fibers, G_{12} and G_{23} are shear moduli parallel and transverse to the fiber direction. These elastic constants can be computed from the fiber and matrix properties. For non-woven composites, the plane stress assumption is made

and hence the elastic constants G_{23} and ν_{23} are not modeled. However, for woven composites all elastic constants should be estimated accurately.

A higher fidelity approach is the use of finite element simulations to model a tow RVE. The microstructure of the tow can be modeled by an RVE with a random arrangement of fibers with a matching fiber volume fraction and fiber spacings (Figure 6.1(A) [16]). Povirk [66], Rintoul et al [67], and Sanei et al [68] have studied algorithms to model the fiber distribution accurately. The importance of the size of the RVE and the length scale used for the reconstruction of the microstructure has been investigated by Kanit et al. [69], Sanei et al. [70], and Gitman et al. [71]. The approach was also extended to 3D by Fliegener et al. [72] to model variations in fiber angles.

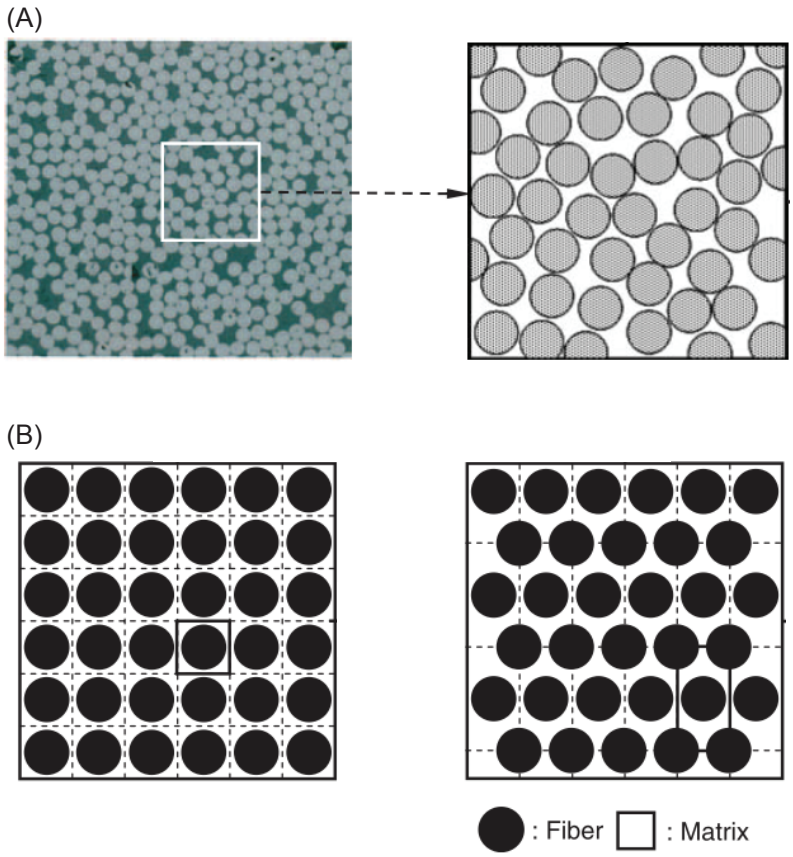

Figure 6.1: Fiber arrangements used to homogenize composites in finite elements [16] (A) Real fiber arrangement and random RVE (B) Simplified uniform square (left) and hexagonal (right) fiber arrangements

A simplified approach is to model an RVE with a uniform arrangement of fibers, often either square or hexagonal (Figure 6.1(B)). Heinrich et al. [73], and Kwok et al. [17] have used uniform RVEs for tow homogenization in woven composites. Huang et al. [16] have shown that uniform RVEs produce the same results as a random RVE for predicting elastic properties but are not appropriate for prediction of damage.

These models have been developed for epoxy composites and their application to prediction of the elastic response of silicone composite tows has been limited. Lopez-Jimenez et al. [53] used a random tow microstructure to model the transverse modulus, E_2, of unidirectional silicone composites and has shown large discrepancies from the analytic model. Maqueda has used the uniform RVE approach to study the fiber microbuckling wavelength in unidirectional elastomer composites [13]. Existing studies have not validated all of the components of the tow stiffness so it remains unclear whether they are appropriate for modeling woven composites.

6.2.1 Tow Homogenization Implementation

Here, a semi-empirical and a uniform RVE approach was applied to the silicone composite as only the elastic properties were of interest. The random RVE requires averaging over many simulations, making it computationally expensive to run parametric studies using such models.

In the semi-empirical approach used here, the estimation of all elastic constants was done using the Halpin-Tsai relations [74],

$$P^* = P_m \frac{1 + \xi \eta V_{f,tow}}{1 - \eta V_{f,tow}} \tag{6.3}$$

where,

$$\eta = \frac{P_f - P_m}{P_f + \xi P_m} \tag{6.4}$$

where P^* is the homogenized tow property of interest, P_f and P_m are the corresponding properties of the fiber and matrix, respectively, and ξ is the fiber reinforcement factor. ξ is dependent on the fiber geometry, fiber arrangement, and loading conditions or can be measured experimentally. It has been shown that ξ is proportional to the aspect ratio of the fibers in the direction of homogenization [75].

For properties in the fiber direction, the ratio of the fiber length to the diameter is very large and so $\xi \to \infty$ and Equation 6.3 reduces to the rule of mixtures. The modulus and Poisson's ratio in the fiber direction can be computed from,

$$E_1 = E_{1f} V_{f,tow} + E_m (1 - V_{f,tow}) \tag{6.5}$$

$$\nu_{12} = \nu_{12f} V_{f,tow} + \nu_m (1 - V_{f,tow}) \tag{6.6}$$

where $V_{f,tow}$ is the fiber volume fraction of the tow, and the f and m subscripts denote fiber and matrix properties, respectively.

The fibers are assumed to be circular and so the computation of the transverse modulus, E_2, and the in-plane shear, G_{12}, are typically computed using $1 < \xi < 2$. This is in good agreement with experimental data for unidirectional epoxy composites but has not been demonstrated for elastomer composites.

It can be shown that $\xi = \frac{K_m}{K_m+2G_m}$ for computation of the out-of-plane shear modulus [74], where K_m is the bulk modulus of the matrix. For incompressible material, $\xi \to 1$. The overall expression for the out-of-plane shear modulus is given by,

$$G_{23} = G_m \frac{K_m(G_m + G_{23f}) + 2G_{23f}G_m + K_m(G_{23f-G_m})V_{f,tow}}{K_m(G_m + G_{23f}) + 2G_{23f}G_m - (K_m + 2G_m)(G_{23f} - G_m)V_{f,tow}} \tag{6.7}$$

Finally, the transverse Poisson's ratio can be computed from the transverse Young's and shear moduli,

$$\nu_{23} = \frac{E_2}{2G_{23}} - 1 \tag{6.8}$$

The highlighted analytic method makes specific assumptions about the fiber arrangement in the tows. In addition, the selected values for ξ assume all fibers are aligned. Small misalignments in the fibers can result in higher transverse properties (and effectively higher values of ξ).

For the RVE method, a uniform unit cell with fibers arranged in a square pattern, shown in Figure 6.2, was modeled using Abaqus/Standard. The RVE was meshed using ~25,000 fully integrated `C3D8` brick elements. Full integration was used to avoid volumetric locking known to occur when modeling incompressible materials such as silicone [76]. Despite a uniform fiber arrangement and periodic boundary conditions, a dependence on the RVE size was found likely due to numerical effects at the corners of the RVE. The number of fibers in the RVE was increased until the values of the extracted stiffness coefficients converged. The minimum number of fibers required in the RVE was found to be 9. The volume fraction of the tow, $V_{f,tow}$, was controlled via the unit cell length, L,

$$L = \sqrt{9\pi r_f^2 / V_{f,tow}} \tag{6.9}$$

where, r_f is the fiber radius.

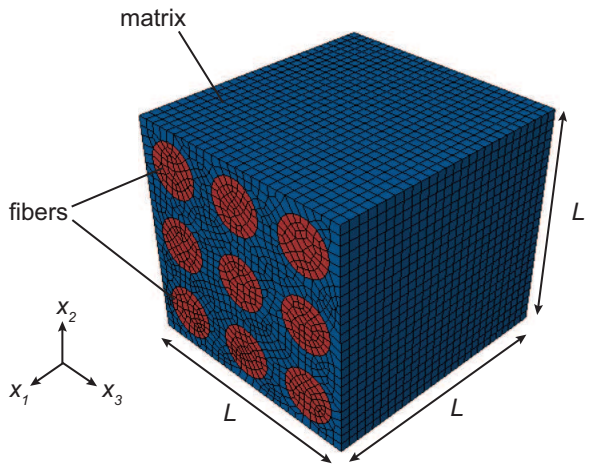

Figure 6.2: Unit cell model for composite tow with square fiber packing

Both the fibers and the matrix were modeled as isotropic, linear elastic with elastic constants defined as in Tables 4.1 and 4.2. Periodic boundary conditions constrained the deformation of opposing faces and corners,

$$u_1(L, x_2, x_3) - u_1(0, x_2, x_3) = \bar{\varepsilon}_{11} L \tag{6.10}$$

$$u_2(L, x_2, x_3) - u_2(0, x_2, x_3) = \bar{\varepsilon}_{12} L \tag{6.11}$$

$$u_3(L, x_2, x_3) - u_3(0, x_2, x_3) = \bar{\varepsilon}_{13} L \tag{6.12}$$

$$u_1(x_1, L, x_3) - u_1(x_1, 0, x_3) = \bar{\varepsilon}_{12} L \tag{6.13}$$

$$u_2(x_1, L, x_3) - u_2(x_1, 0, x_3) = \bar{\varepsilon}_{22} L \tag{6.14}$$

$$u_3(x_1, L, x_3) - u_3(x_1, 0, x_3) = \bar{\varepsilon}_{23} L \tag{6.15}$$

$$u_1(x_1, x_2, L) - u_1(x_1, x_2, 0) = \bar{\varepsilon}_{13} L \tag{6.16}$$

$$u_2(x_1, x_2, L) - u_2(x_1, x_2, 0) = \bar{\varepsilon}_{23} L \tag{6.17}$$

$$u_3(x_1, x_2, L) - u_3(x_1, x_2, 0) = \bar{\varepsilon}_{33} L \tag{6.18}$$

where $\bar{\varepsilon}_{ij}$ are the volume average strains over the RVE, and u_i is the displacement in direction x_i. The strain components were associated with the arbitrary displacement of a dummy node. Three separate analyses, applying unit displacements of $\bar{\varepsilon}_{11}$, $\bar{\varepsilon}_{22}$, and $\bar{\varepsilon}_{12}$, were carried out to extract the corresponding volume average stresses, $\bar{\sigma}_{ij}$, and compute the 5 independent engineering constants, E_1, E_2, ν_{12}, G_{12}, and G_{23}.

6.3 Plain-Weave Homogenization Models

The goal of the plain-weave homogenization is to compute the ABD stiffness matrix of the woven composite as defined in Section 4.6. A common assumption in modeling of woven composites is that the tows can be approximated as sinusoidal. Soykasap [37] and Kueh et al. [77] have modeled the tows as sinusoidal beams. Kuhn et al. [78], Heinrich et al. [35], and Kwok et al. [17] have modeled the tows using 3D elements, with varying assumptions for the matrix distribution. Furthermore, the effects of statistical variations in the weave were investigated by Vanaerschot et al. [79]. Typically for a plain-weave, a RVE with boundaries parallel to the warp and weft fibers is selected, with a single ply modeled. Soykasap [37] and Mallikarachchi et al. [35] have investigated unit cells of multiple plies. Soykasap [37] has furthermore modeled the interaction between plies due to neighbouring plies having in-phase or out-of-phase stacking of fibers. However, these models are limited to unidirectional laminates. Typically, prediction of properties for arbitrary laminates is achieved by modeling stiffness of a single ply, $\bar{\boldsymbol{Q}}$, and computing laminate stiffness using CLT (Equations 4.13 – 4.15).

6.3.1 Plain-Weave Homogenization Implementation

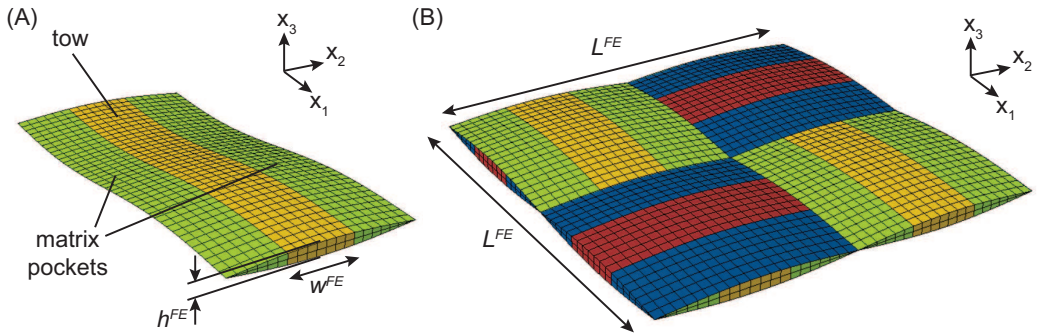

Figure 6.3: Unit cell model for plain-weave geometry modified from [17] (A) tow and resin pockets (B) full unit cell model with warp tows in yellow and weft tows in red

Here, the weave was modeled using the Abaqus/Standard finite element software with a geometry borrowed with modification from Kwok [17]. The model consisted of four of the solids in Figure 6.3(A), each rotated 90° from the previous, to form the unit cell in Figure 6.3(B). The boundaries of the solid in Figure 6.3(B) are given by,

$$x_3 = \pm\frac{h^{FE}}{2}\sin\left(\frac{2\pi x_2}{L^{FE}}\right) + \frac{h^{FE}}{2}\sin\left(\frac{2\pi x_1}{L^{FE}}\right) \tag{6.19}$$

where, L^{FE} is the unit cell wavelength, h^{FE} is the tow height, and w^{FE} is the tow width. The FE superscript indicates that the geometry in the finite element model is not necessarily identical to that of the physical weave in Section 4.5. Most notably, the RVE thickness varies from $t^{FE} = 0$ at the corners to $f^{FE} = 2h^{FE}$ at the apex of the sinusoids.

The surfaces of the tows were connected to each other using tie multi-point constraints. Furthermore, nodes of the surface of the tows were connected to the midplane of the tow via rigid beams to enforce Kirchhoff plate theory, implemented in Abaqus using `CONN3D2` connector elements. The model was meshed using 1600 8-node and 6-node brick elements, `C3D8` and `C3D6`, respectively. The matrix material properties were defined as elastic and isotropic using the properties in Table 4.2. The stiffness tensor of the tows was modeled as elastic and transversely isotropic using properties obtained through homogenization of the tow. The periodic boundary conditions on the unit cell are given by [77],

$$u_1\left(\frac{L}{2}, x_2\right) - u_1\left(-\frac{L}{2}, x_2\right) = \varepsilon_1 L \tag{6.20}$$

$$u_2\left(\frac{L}{2}, x_2\right) - u_2\left(-\frac{L}{2}, x_2\right) = \frac{1}{2}\varepsilon_3 L \tag{6.21}$$

$$u_3\left(\frac{L}{2}, x_2\right) - u_3\left(-\frac{L}{2}, x_2\right) = -\frac{1}{2}\kappa_3 x_2 L \tag{6.22}$$

$$\theta_1\left(\frac{L}{2}, x_2\right) - \theta_1\left(-\frac{L}{2}, x_2\right) = -\frac{1}{2}\kappa_3 L \tag{6.23}$$

$$\theta_2\left(\frac{L}{2}, x_2\right) - \theta_2\left(-\frac{L}{2}, x_2\right) = \kappa_1 L \tag{6.24}$$

$$\theta_3\left(\frac{L}{2}, x_2\right) - \theta_3\left(-\frac{L}{2}, x_2\right) = 0 \tag{6.25}$$

$$u_1\left(x_1, \frac{L}{2}\right) - u_1\left(x_1, -\frac{L}{2}\right) = \frac{1}{2}\varepsilon_3 L \tag{6.26}$$

$$u_2\left(x_1, \frac{L}{2}\right) - u_2\left(x_1, -\frac{L}{2}\right) = \varepsilon_2 L \tag{6.27}$$

$$u_3\left(x_1, \frac{L}{2}\right) - u_3\left(x_1, -\frac{L}{2}\right) = -\frac{1}{2}\kappa_3 x_1 L \tag{6.28}$$

$$\theta_1\left(x_1, \frac{L}{2}\right) - \theta_1\left(x_1, -\frac{L}{2}\right) = -\kappa_2 L \tag{6.29}$$

$$\theta_2\left(x_1, \frac{L}{2}\right) - \theta_2\left(x_1, -\frac{L}{2}\right) = \frac{1}{2}\kappa_3 L \tag{6.30}$$

$$\theta_3\left(x_1, \frac{L}{2}\right) - \theta_3\left(x_1, -\frac{L}{2}\right) = 0 \tag{6.31}$$

where u_i is the displacement in direction x_i, θ_i is the rotation about axis x_i, and ε_i and κ_i are the midplane strains and curvatures, respectively. The strains and curvatures were applied through displacements of dummy nodes. Four separate analyses with applied ε_1 and ε_3 unit strains and κ_1 and κ_3 unit curvatures are required to compute all coefficients of the ABD matrix.

The original model from Kwok set the finite element geometry to the corresponding parameters measured experimentally [17]. Since the matrix pocket distribution, thickness variation, and tow shape in the model are not identical to the physical weave, a different approach was taken here. The geometry of the finite element model was chosen to match several critical parameters of the physical weave: the composite volume fraction, the tow thickness, and the crimp ratio of the weave, h/L. These can be expressed in the following constraints, respectively,

$$V_f = \sin\left(\frac{\pi w^{FE}}{L^{FE}}\right) V_{f,tow} \tag{6.32}$$

$$h^{FE} = 0.5t \tag{6.33}$$

$$\frac{h^{FE}}{L^{FE}} = \frac{h}{L} \tag{6.34}$$

The geometry of the finite element unit cell can be computed by solving Equations 6.32 – 6.34

simultaneously. The results are given by,

$$h_{FE} = 0.5t \tag{6.35}$$

$$L_{FE} = h^{FE}\frac{L}{h} \tag{6.36}$$

$$w_{FE} = \frac{L_{FE}}{\pi}\sin^{-1}\left(\frac{V_f}{V_{f,tow}}\right) \tag{6.37}$$

These constraints are chosen intuitively and are only used to select a nominal geometry in the simulations.

6.4 Investigation of Composite Tow Properties

6.4.1 Applying Existing Models for Epoxy Composites

The two models in Section 6.2 were used to compute a baseline tow stiffness to gage whether commonly used models from literature for epoxy composites are appropriate for the woven elastomer composites studied here. The random fiber arrangement approach was not attempted due to long computational times associated with computing an average response not compatible with the sensitivity studies done here.

The homogenized elastic constants as a function of $V_{f,tow}$ using the RVE and analytic models are shown in Figure 6.4 for the AQ/epoxy composite. There is good agreement between the uniform RVE and the analytic model for the longitudinal stiffness, E_1, and the two shear stiffnesses. However, the analytic model predicts lower values of the transverse stiffness, E_2, than the finite element homogenization (by ~20%). The transverse Poisson's ratio is dependent on E_2 and shows a comparable difference in the ν_{23} models. Furthermore, the analytic approach predicts ν_{12} 15% higher than the RVE. As will be demonstrated in Section 6.4.2, the Poisson's ratios have very little influence on the weave stiffness and hence the discrepancy in their values is neglected here.

The results from this study are used to compute the ABD stiffness matrix of the AQ/epoxy composites for the experimentally measured tow fiber volume fraction, $V_{f,tow} = 0.75$. The geometry of the woven unit cell used is given in Table 6.3. The finite element model predicts the ABD matrix for a single ply. CLT is then used to compare this result to experimental measurements of stiffness of various laminates.

The predicted extensional stiffness, A_{11}, and bending stiffness, D_{11}, at two different fiber angles are compared to experimental results for the AQ/epoxy composite in Table 6.1. The uniform RVE and analytic Halpin-Tsai method both result in predictions lower than experimental measurements. It can be seen that the agreement in the 45° direction is much better than in the fiber direction. Furthermore, the models predict a higher bending stiffness in the 45° direction than in the fiber

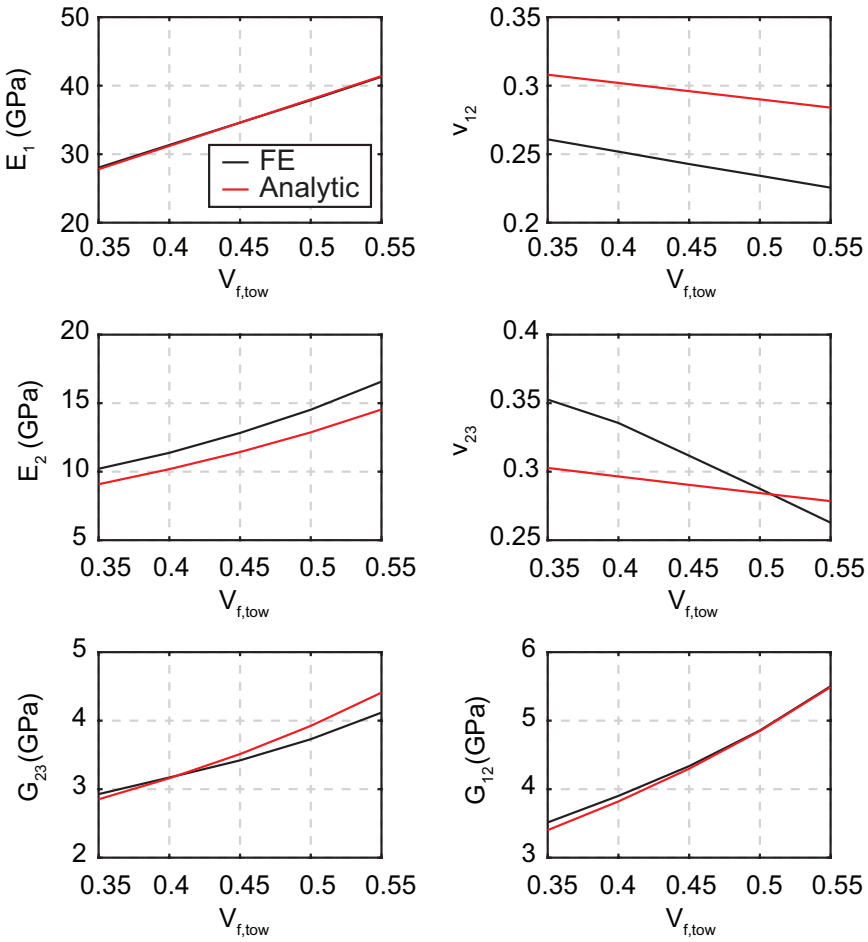

Figure 6.4: Tow elastic constants as a function of tow fiber volume fraction for the AQ/epoxy composite – uniform finite element RVE and analytic predictions from Equation 6.3

direction, in contrast to experimental observations and intuition. This indicates an inaccurate prediction of A_{12}, A_{33}, D_{12}, and D_{33}, for a single ply, with error then propagated through CLT. As both the RVE approach and the analytic approach have been shown to be accurate for epoxy composites in literature, and yield comparable results, there is little reason to consider large adjustments to the tow model. Instead, discrepancies can be accounted for by changes to the model weave geometry as will be demonstrated in Section 6.5.

The homogenized elastic constants as a function of $V_{f,tow}$ using the RVE and analytic models are shown in Figure 6.5 for the AQ/silicone composite. Comparing predictions for the AQ/silicone tow, a much larger discrepancy is seen between the two models compared to the AQ/epoxy composite. The longitudinal modulus shows excellent agreement. However, a large difference is observed in the predictions for E_2, G_{12}, and G_{23}. Moreover, the disagreement in E_2 grows with increasing fiber volume fraction in the tow. A similar trend was observed by Lopez-Jimenez in [53] for a carbon fiber reinforced silicone composite. For incompressible matrices, it is found that the Halpin-Tsai

Stiffness Coefficient	Layup	Measurement	Uniform RVE	Analytic
A_{11} (N/mm)	$[0_3]_{pw}$	4350	2614	2545
A_{11} (N/mm)	$[45_3]_{pw}$	2727	2412	2373
D_{11} (N·mm)	$[0_3]_{pw}$	15.2	6.0	5.9
D_{11} (N·mm)	$[45_3]_{pw}$	12.1	7.9	7.7

Table 6.1: Prediction of ABD stiffness of AQ/epoxy laminates using analytic and uniform RVE approaches

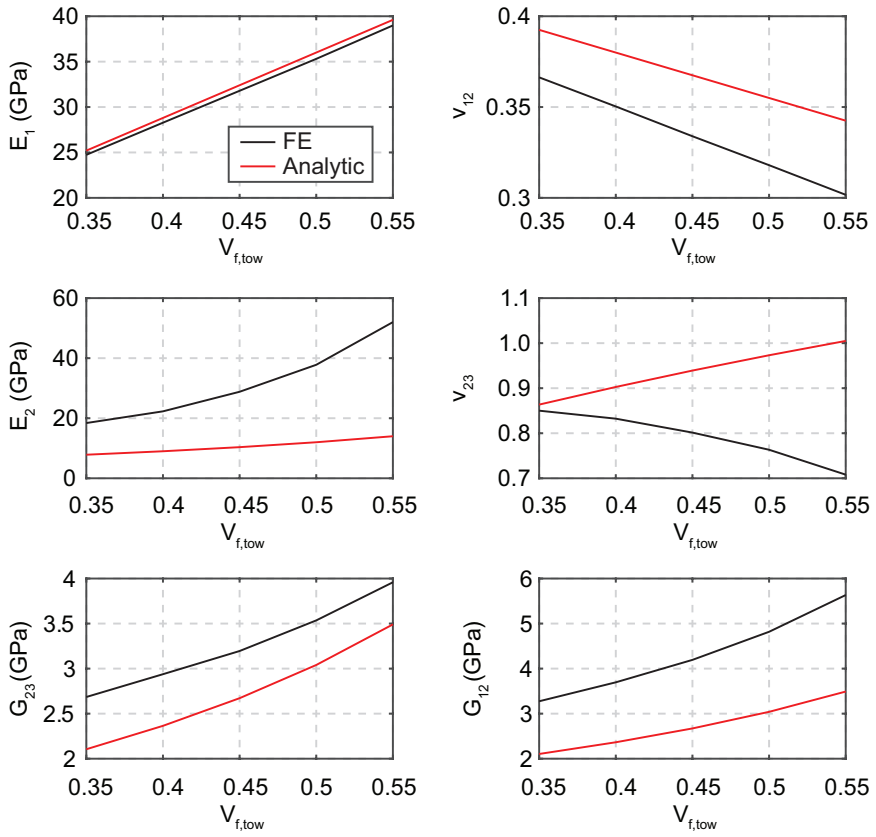

Figure 6.5: Tow elastic constants as a function of tow fiber volume fraction – uniform finite element RVE and analytic predictions from Equation 6.3

model no longer provides a good estimate and that the value of the experimental parameter ξ must be increased significantly to reproduce experimental measurements. Furthermore, the fiber arrangement may play a role in the transverse properties, where clumping of the fibers at low volume fractions can create load paths which increase the overall stiffness of the tow. Lastly, slight misalignments of the fibers can carry the load in the transverse direction, effectively increasing the stiffness. From these observations, it is clear that both the analytic and finite element models commonly used for epoxy composites result in large errors when homogenizing elastomer composites. Finally, note that $\nu_{23} > 0.5$ is a result of the incompressible matrix when reinforced with stiff fibers.

Extreme Poisson's ratios in elastomer reinforced composites have been reported in simulations and measured experimentally as discussed in [80].

The results are used to compute the ABD matrix of a single ply of AQ/silicone with $V_{f,tow} = 0.65$. The geometry of the woven model used is given in Table 6.3. The predicted extensional stiffness, A_{11}, and bending stiffness, D_{11}, at two different fiber angles are compared to experimental results for the AQ/silicone composite in Table 6.2. Similar to the AQ/epoxy composite, the predicted stiffness is lower but in this case by several orders of magnitude. As described above, the assumptions in the RVE and the analytic approach significantly under-predict the transverse tow stiffness and result in very low ply stiffness. The prediction of in-plane stiffness is a factor of ~400 lower than measurements and the prediction of bending stiffness is a factor of ~15 lower than measurements. Hence, the commonly used tow homogenization techniques are not appropriate for predicting the stiffness of elastomer composites.

Stiffness Coefficient	Layup	Measurement	Uniform RVE	Analytic
A_{11} (N/mm)	$[0_3]_{pw}$	2453	5.43	4.40
A_{11} (N/mm)	$[45_3]_{pw}$	1419	3.90	3.44
D_{11} (N·mm)	$[0_3]_{pw}$	5.71	0.37	0.31
D_{11} (N·mm)	$[45_3]_{pw}$	2.57	0.19	0.16

Table 6.2: Prediction of ABD stiffness of AQ/silicone laminates using analytic and RVE approaches

It can be seen that the standard approach to modeling of the tow properties is not appropriate for the woven composites here. The AQ/epoxy composite does not accurately predict the stiffness in all fiber direction. Studies in [17, 35] have tuned the geometry of the weave to yield reasonable predictions in the direction of interest. The AQ/silicone composite shows a significantly different behavior in simulation showing that the tow stiffness, in addition to the weave geometry, must be modified to reproduce measurements.

In the future, measurements of the tow stiffness would be advantageous for comparison with the estimates given here. This was beyond the scope of the present study as techniques for testing the tow stiffness differ significantly from those for laminate stiffness. Furthermore, experimental observation of fiber misalignments and subsequent simulations could prove the hypothesis that this is the cause of increased tow stiffness in elastomer composites.

6.4.2 Sensitivity to Tow Stiffness

It was demonstrated in Section 6.4.1 that neither the uniformly packed RVE nor the standard Halpin-Tsai model can predict the transverse stiffness of the tow for the AQ/silicone composite.

Here a modified analytic approach is investigated for predicting the tow stiffness. The composite

tow can be described by two limiting models: the parallel Voigt model and the series Reuss model. In the Voigt model, the fiber and matrix are assumed to have equal uniform strain leading to the following estimate,

$$P^* = P_f V_{f,tow} + P_m(1 - V_{f,tow}) \tag{6.38}$$

where P^*, P_f, P_m are the composite, fiber, and matrix stiffnesses, respectively. This represents an upper bound on the composite stiffness and has previously been introduced in Section 6.2 as the rule of mixtures.

In contrast, the Reuss model assumes the fiber and matrix have equal uniform stress leading to the following estimate,

$$P^* = \frac{1}{V_{f,tow}/P_f + (1 - V_{f,tow})/P_m} \tag{6.39}$$

This represents a lower bound on the composite stiffness. In reality, the stress and strain in the composite are not uniform and the true stiffness lies between these two limits. Energy methods can be used to obtain more accurate bounds and correspond to the estimates presented in Section 6.2.

For the Halpin-Tsai model in Equation 6.3, it can be seen that taking $\xi \to 0$ leads to the Reuss model and taking $\xi \to \infty$ leads to the Voigt model, providing a convenient way for varying the tow stiffness. The appropriate value of ξ for each stiffness component of the composite can be found experimentally, instead of using the heuristic that $1 < \xi < 2$. This simple method can account for clumping of fibers in the tow microstructure as well as misalignments of fibers causing higher transverse tow stiffness. Here, the effects of varying ξ on the composite stiffness are investigated.

Four parameters are introduced: ξ_{E_2}, $\xi_{\nu_{12}}$, $\xi_{G_{12}}$, and $\xi_{G_{23}}$, where the subscripts indicate which elastic constant of the composite tow the parameter is used to predict. Each parameter is varied between 0 and ∞ and used to predict the corresponding tow elastic constant. The longitudinal stiffness is computed using the rule of mixtures ($\xi = \infty$) as this has been shown to be a very accurate estimate, even for elastomer composites. The resulting tow stiffness is used as an input to the plain-weave finite element RVE model to predict the resulting ABD stiffness of the composite ply.

The effects of varying each ξ on the AQ/epoxy ply stiffness are shown in Figure 6.6. Each subplot shows the percent change in each ABD stiffness component in response to an increase in ξ. The percent change is defined with respect to the ABD stiffness for $\xi = 0$,

$$\%\text{ change in stiffness} = \frac{ABD_{ij}(\xi) - ABD_{ij}(\xi = 0)}{ABD_{ij}(\xi = 0)} \tag{6.40}$$

It is seen that the largest increase ABD stiffness of the AQ/epoxy ply is in response to the in-plane shear stiffness, G_{12}, of the tow. The largest effects are for the composite twisting stiffness, D_{33}, and the ply Poisson's effects, A_{12}. Furthermore, the out-of-plane shear stiffness, G_{23}, also shows a large proportionality with the twisting stiffness. The extensional, A_{11}, and bending, D_{11}, stiffnesses

show moderate increases in response to an increasing transverse extensional stiffness of the tow, E_2. Finally, the Poisson's ratio has very little effect on the ply stiffness. Overall, the effects of increasing ξ are moderate for the AQ/epoxy tow, with variation of ply stiffness less than a factor of 2.5 for all coefficients.

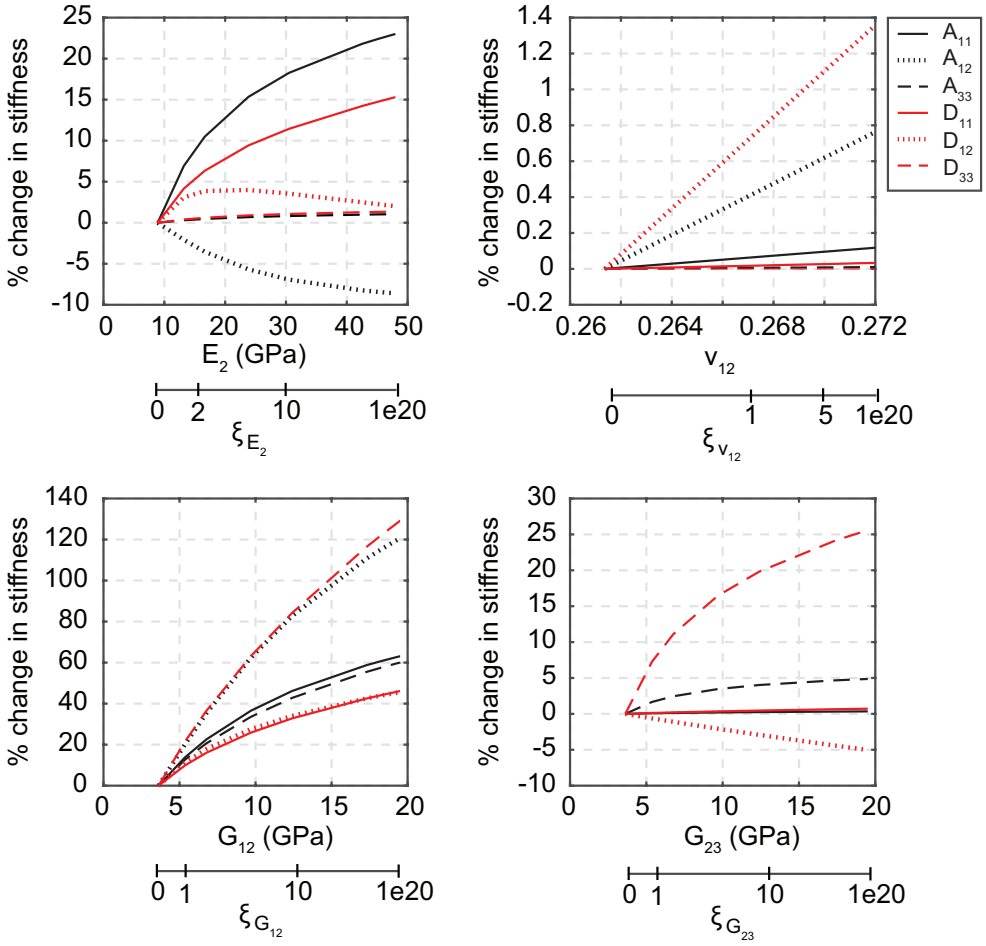

Figure 6.6: Dependence of weave stiffness of a single ply on tow elastic constants – AQ/epoxy composite

The effects of varying each ξ on the AQ/silicone ply stiffness are shown in Figure 6.7. The trends for the silicone composite are similar to the epoxy composite but the overall increase in ply stiffness is much higher in response to changes of tow stiffness. The extensional stiffness, A_{11}, rises by a factor of greater than 10 over the allowed range of E_2. The composite twisting stiffness, D_{33}, can increase by a factor of 250 in response to an increase in G_{12}. This extreme sensitivity to tow properties seen in the AQ/silicone ply shows the need for estimating them correctly.

It is worth noting that for the AQ/epoxy composite, a small change in ξ (e.g., from 1 to 2) can results in a large increase in corresponding tow stiffness. This is illustrated by the dual x-axis in Figure 6.6. To obtain similar increase in stiffness of the AQ/silicone composite, very large values of

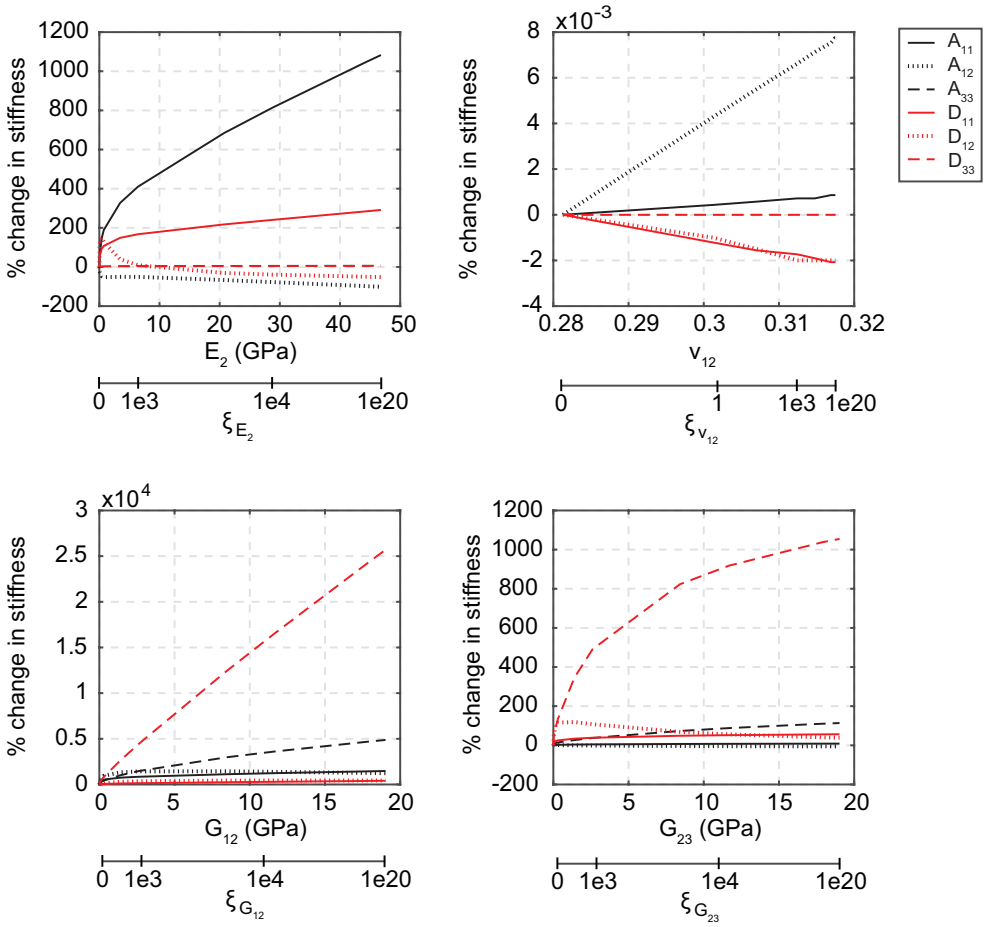

Figure 6.7: Dependence of weave stiffness of a single ply on tow elastic constants – AQ/silicone composite

ξ are required (e.g., 1000), as shown by the dual x-axis in Figure 6.7. Hence, the heuristic ξ values used for epoxy are not appropriate for silicone.

6.5 Dependence on Unit Cell Geometry

The nominal RVE weave geometry was selected as described in Section 6.3. The nominal geometric parameters used in the finite element model for the AQ/epoxy and AQ/silicone composites are computed using Equations 6.35 – 6.37, using the experimentally measured geometries summarized in Tables 4.5 and 4.6. The results for the two composites are summarized in Table 6.3. The finite element tow width, chosen to match the measured fiber volume fractions, is quoted for 3-ply composites as finite element predictions are compared with measurements of 3-ply laminates.

There are experimental errors associated with the averages in Tables 4.5 and 4.6 as well as a spread in the measured values as indicated by the quoted standard deviations. Furthermore, there is not a one-to-one correspondence between physical weave geometry and the modeled RVE geometry.

	h^{FE} (µm)	L^{FE} (µm)	w^{FE} (µm) (3-ply)
AQ/epoxy	38	919	235
AQ/silicone	46	1043	220

Table 6.3: Nominal plain-weave finite element geometry of AQ/epoxy and AQ/silicone composites

Sensitivity studies were conducted to understand the influence of changes to the weave geometry on the resulting ABD stiffness of a single ply.

6.5.1 Sensitivity to h^{FE} and L^{FE}

The effects of varying the RVE tow height and wavelength on a single $[0]_{pw}$ ply of AQ/epoxy and AQ/silicone are shown in Figures 6.8 and 6.9, respectively. In these studies, the tow properties were computed using the analytic Halpin-Tsai approach with default value for the reinforcement parameter of $\xi_{E_2} = \xi_{G_{23}} = 2$ and $\xi_{G_{12}} = 1$.

Applying a pure tensile load to a woven ply results in combined axial and bending strains in the tows as they straighten in response to the applied load. The same holds for a pure bending load applied to the woven ply. As a result, both the axial and bending stiffnesses are reduced from a non-woven composite of the same material with the same thickness. For woven plies with lower fiber crimp (i.e., lower h/L), this coupling is reduced and the ply behavior begins to approximate that of a unidirectional composite. This observation can explain much of the dependence on finite element unit cell geometry that is seen in this study.

For the AQ/epoxy ply, increasing the height of the tows significantly increases all of the ABD stiffness coefficients (Figure 6.8). The in-plane stiffness, $\boldsymbol{A}$, increases by a factor of approximately 1.5 upon doubling the height. The impact on the out-of-plane stiffness, $\boldsymbol{D}$, is even more pronounced, where doubling the tow height increases the coefficients by a factor of $3-4$. This proportionality is not surprising and is predicted by Equations 4.13 and 4.15 which show that the the in-plane stiffness is proportional to the ply thickness and the out-of-plane stiffness is proportional to the cube of the ply thickness. This dependence is slightly reduced here as the stiffness, $\bar{\boldsymbol{Q}}$, also changes with h^{FE} and L^{FE}. Increasing the wavelength of the finite element unit cell causes a large increase in extensional and bending stiffnesses, A_{11} and D_{11}. A smaller crimp in the fibers causes the composite to behave closer to a non-woven composite, thereby increasing the stiffness. However, the wavelength has very little effect on the shear stiffness, A_{33}, and the twisting stiffness, D_{33}, of the composite.

The AQ/silicone composite shows a very different dependence on the finite element unit cell (Figure 6.9). The tow height has a similar effect on D_{11} for the AQ/silicone ply as for the AQ/epoxy ply. However, A_{11} does not exhibit the same increase with tow height as seen for the AQ/epoxy ply. In fact, there is little impact from increasing tow height, particularly for smaller unit cell wavelengths.

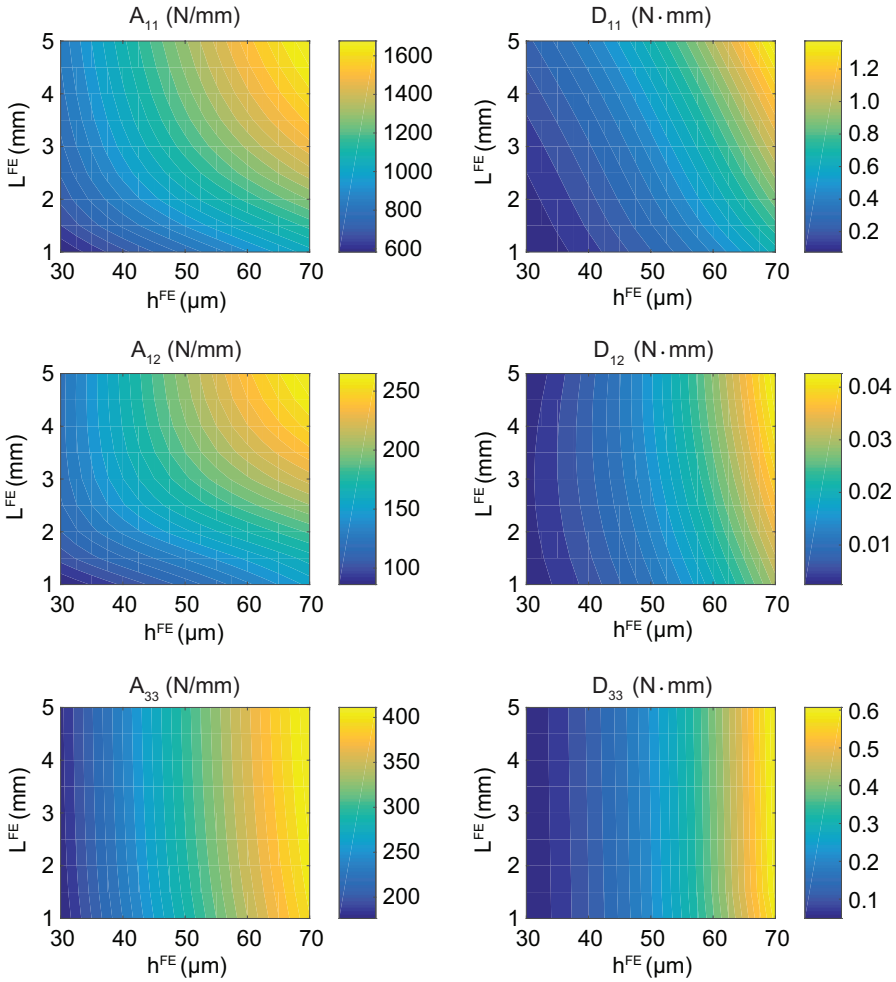

Figure 6.8: Sensitivity of the ABD matrix of a single ply of AQ/epoxy composite to the finite element weave geometry ($\xi_{E_2} = \xi_{G_{23}} = 2; \xi_{G_{12}} = 1$)

At higher crimp ratios, a larger fraction of the axial loading of the ply is accommodated through bending of the tows, decreasing the axial stiffness. A competing effect is the increase in area of the tows. For a compliant silicone tow, these two effects balance out resulting in very little dependence on the tow height. As for the AQ/epoxy composite, increasing L^{FE} results in higher A_{11} and D_{11} but has little effect on A_{33} and D_{33}.

It is also interesting to examine the sensitivity of the AQ/silicone composite to geometry at higher values of the reinforcing parameter – $\xi_{E_2} = 1 \times 10^4$ and $\xi_{G_{23}} = 1 \times 10^3$ (Figure 6.10). It can be seen that the behavior is changed from lower values of the tow stiffness. For this case, the AQ/silicone composite behaves similar to the AQ/epoxy composite. The only difference seen is a higher dependence of A_{33} and D_{33} on L^{FE}.

The dependence of the A_{11} and D_{11} coefficients on the weave geometry is also computed for the $[0_3]_{pw}$ and $[45_3]_{pw}$ layups to facilitate comparison with experimental measurements. The stiffness

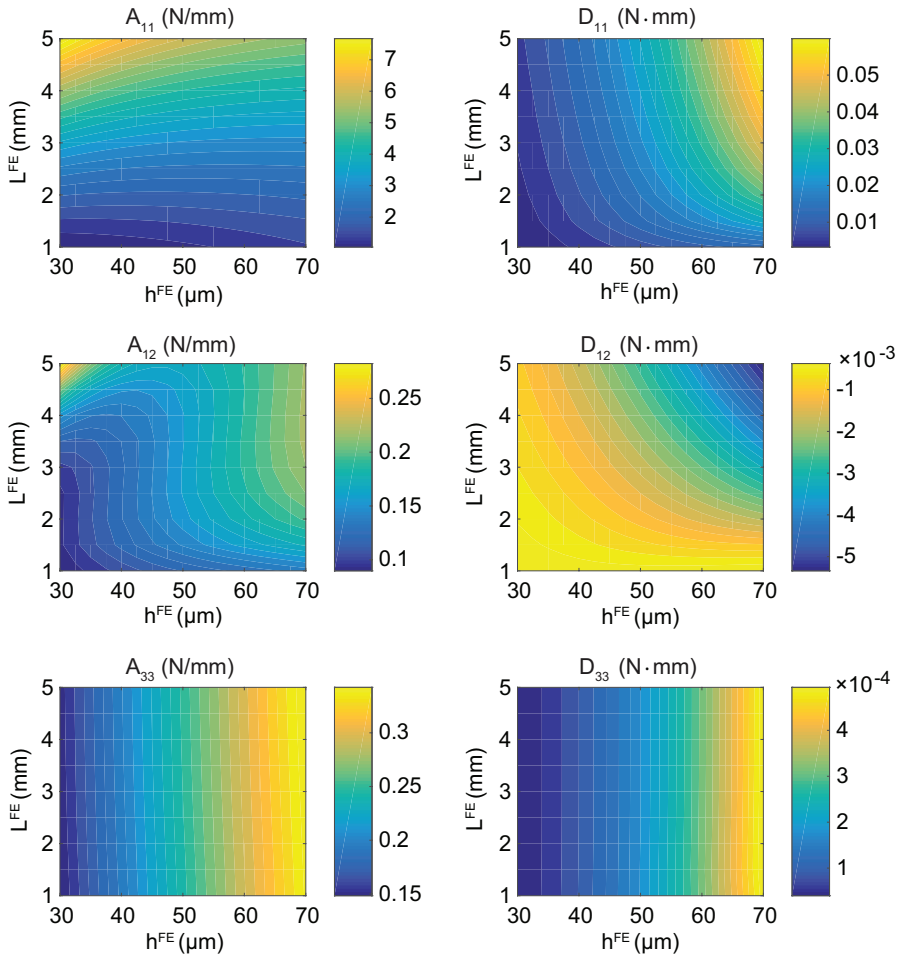

Figure 6.9: Sensitivity of the ABD matrix of a single ply of AQ/silicone composite to the finite element weave geometry ($\xi_{E_2} = \xi_{G_{23}} = 2; \xi_{G_{12}} = 1$)

of these AQ/epoxy laminates as a function of h^{FE} and L^{FE} is plotted in Figure 6.11. Comparison with measurements in column 3 of Table 6.1 show that experimental agreement can be achieved by modifying the finite element weave geometry. Much higher values of tow height and wavelength may be required in simulation than predicted by the constraints in Equations 6.35 – 6.37. Since the model weave is only an approximation of the the physical weave geometry this is to be expected.

The stiffness of the $[0_3]_{pw}$ and $[45_3]_{pw}$ AQ/silicone laminates as a function of h^{FE} and L^{FE} are plotted in Figure 6.12 with $\xi_{E_2} = \xi_{G_{23}} = 2$ and $\xi_{G_{12}} = 1$. Comparison with measurements in column 3 of Table 6.2 reveals that no value of h^{FE} and L^{FE} can reproduce experimental results. The tow wavelength would need to be set to unrealistically high values (>100 mm) to increase the stiffness to measured values. The AQ/silicone tow stiffness must be varied along with weave geometry to obtain good agreement with the experimental measurements.

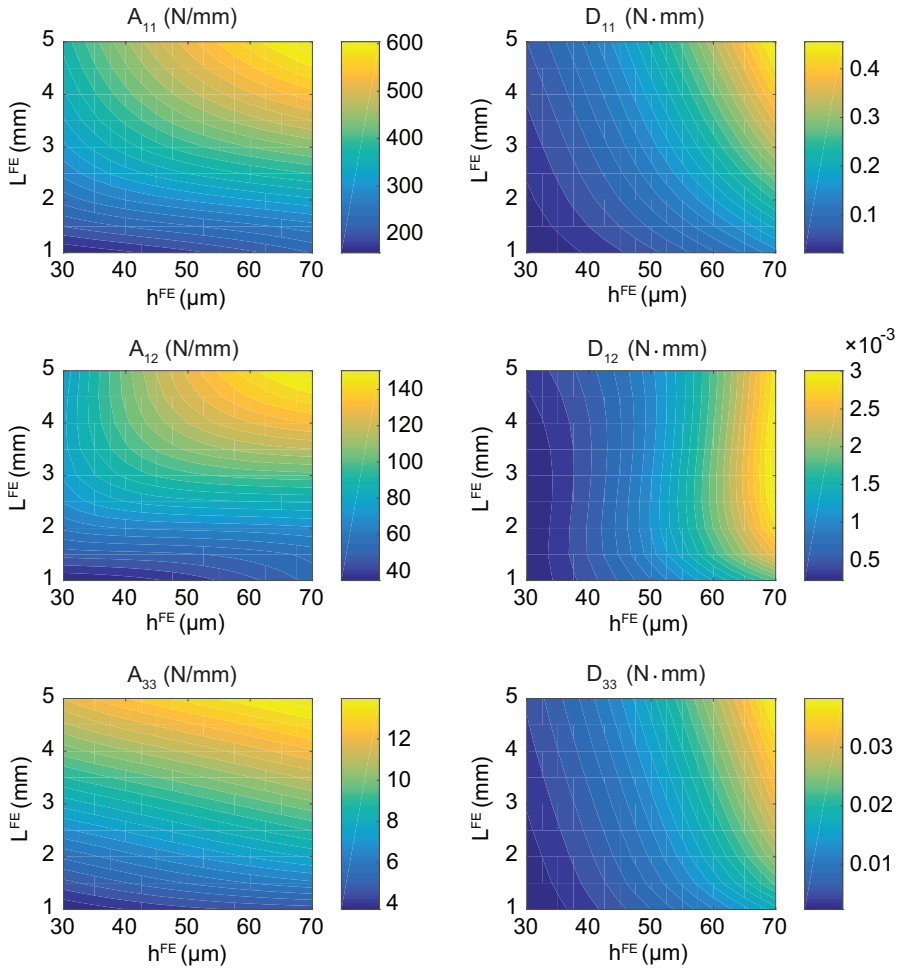

Figure 6.10: Sensitivity of the ABD matrix of a single ply of AQ/silicone composite to the finite element weave geometry ($\xi_{E_2} = 1 \times 10^4; \xi_{G_{23}} = 1 \times 10^3; \xi_{G_{12}} = 1$)

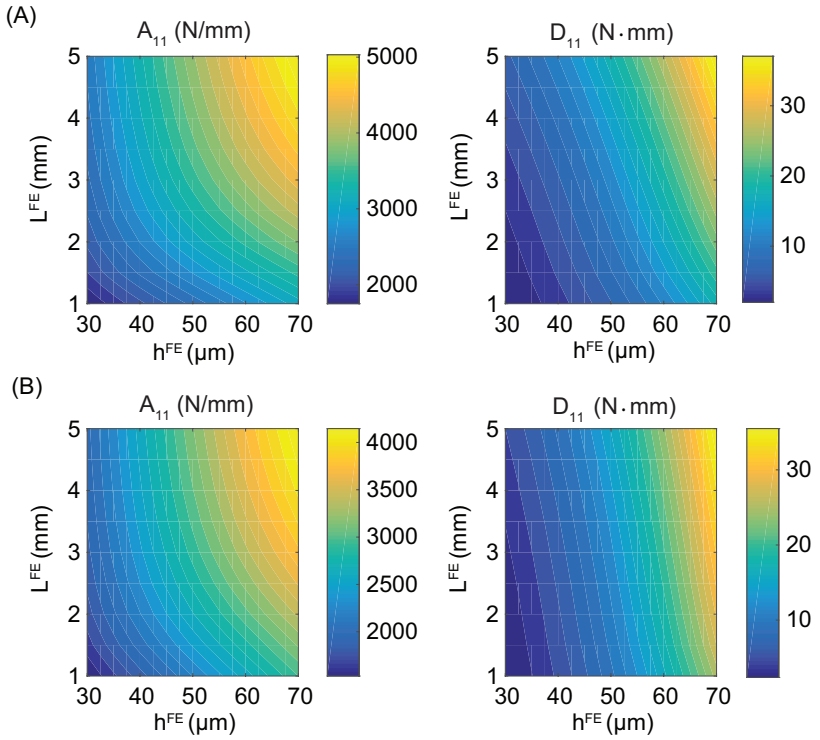

Figure 6.11: Sensitivity of the extensional and bending stiffness of AQ/epoxy laminates to the finite element weave geometry ($\xi_{E_2} = \xi_{G_{23}} = 2; \xi_{G_{12}} = 1$) (A) $[0_3]_{pw}$ (B) $[45_3]_{pw}$

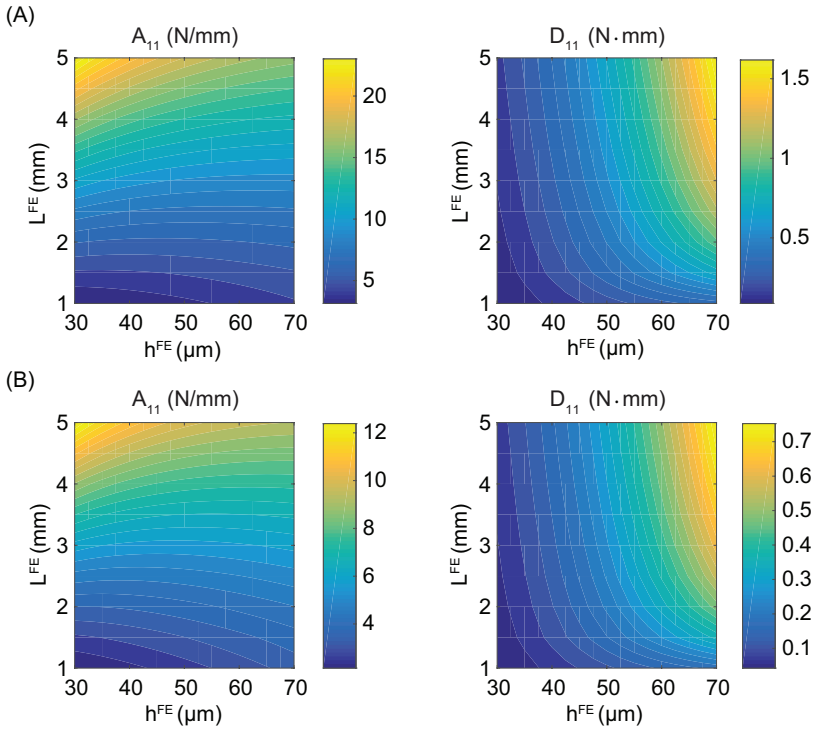

Figure 6.12: Sensitivity of the extensional and bending stiffness of AQ/silicone laminates to the finite element weave geometry ($\xi_{E_2} = \xi_{G_{23}} = 2; \xi_{G_{12}} = 1$) (A) $[0_3]_{pw}$ (B) $[45_3]_{pw}$

6.5.2 Dependence on Fiber Volume Fractions

The effects of varying the tow and composite fiber volume fractions in simulation on the woven ply stiffness are illustrated in Figures 6.13 and 6.14 for the AQ/epoxy ($\xi_{E_2} = \xi_{G_{23}} = 2$ and $\xi_{G_{12}} = 1$) and AQ/silicone ($\xi_{E_2} = 1 \times 10^4$, $\xi_{G_{23}} = 1 \times 10^3$ and $\xi_{G_{12}} = 1$) composites, respectively.

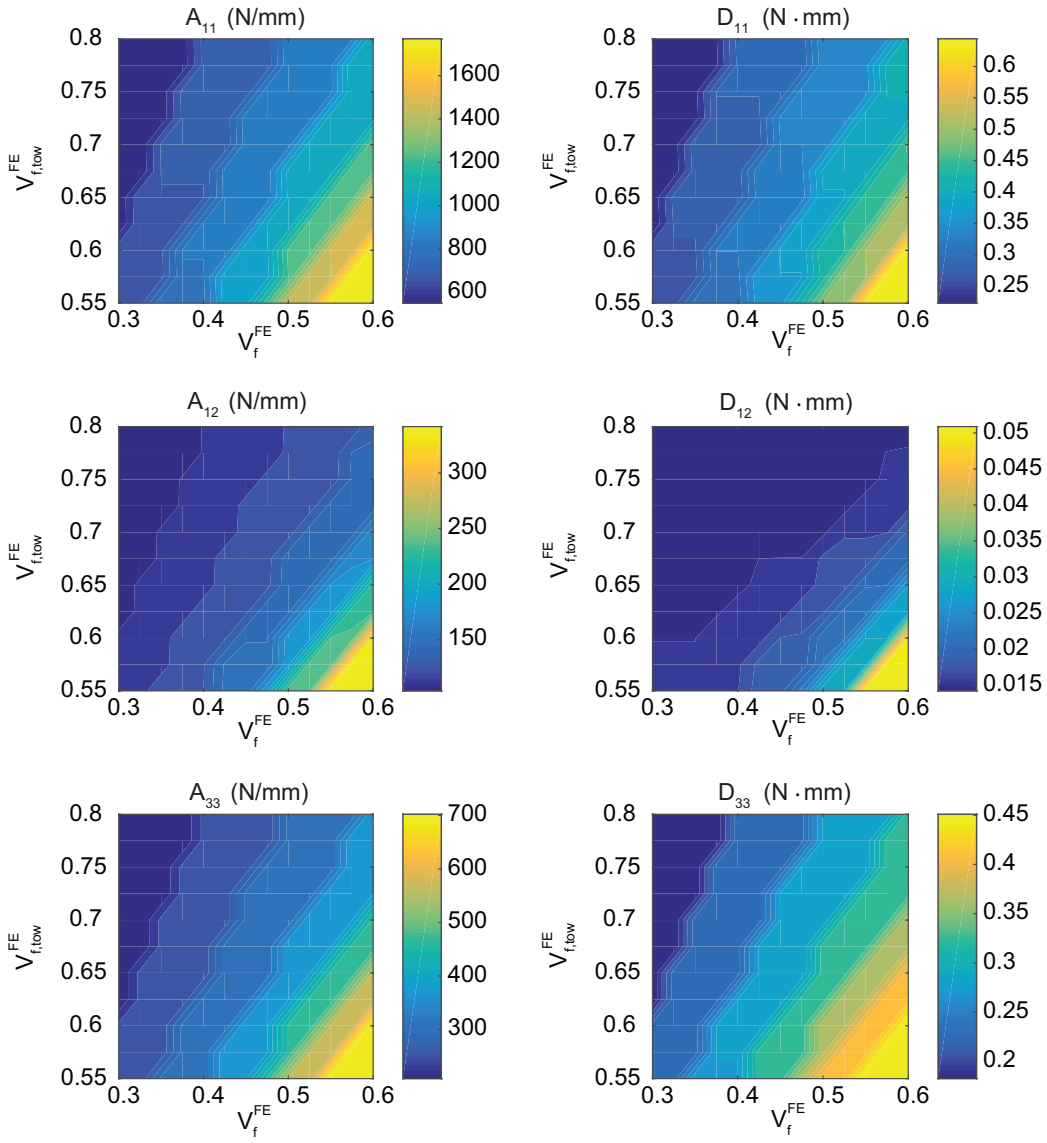

Figure 6.13: Sensitivity of the ABD matrix of a single ply of AQ/epoxy composite to the composite and tow fiber volume fractions

The behavior of the two composites is similar. All stiffness components increase with the fiber volume fraction of the composite, V_f^{FE}, but decrease with increasing fiber volume fraction of the tow, $V_{f,tow}^{FE}$. The increase of stiffness with V_f^{FE} is not surprising due to the increasing fiber content. Furthermore, the main contribution to stiffness of the ply stems from the tows. For a given V_f^{FE}, increasing $V_{f,tow}^{FE}$ results in narrower (i.e., smaller w^{FE}) but stiffer tows. From the inverse propor-

tionality, it is evident the decrease in width has a higher effect on the bending and extensional stiffness of the tows than the increase in stiffness. The only exception to this are the A_{12} and D_{33} stiffness coefficients for the AQ/silicone composite which are proportional to $V_{f,tow}^{FE}$.

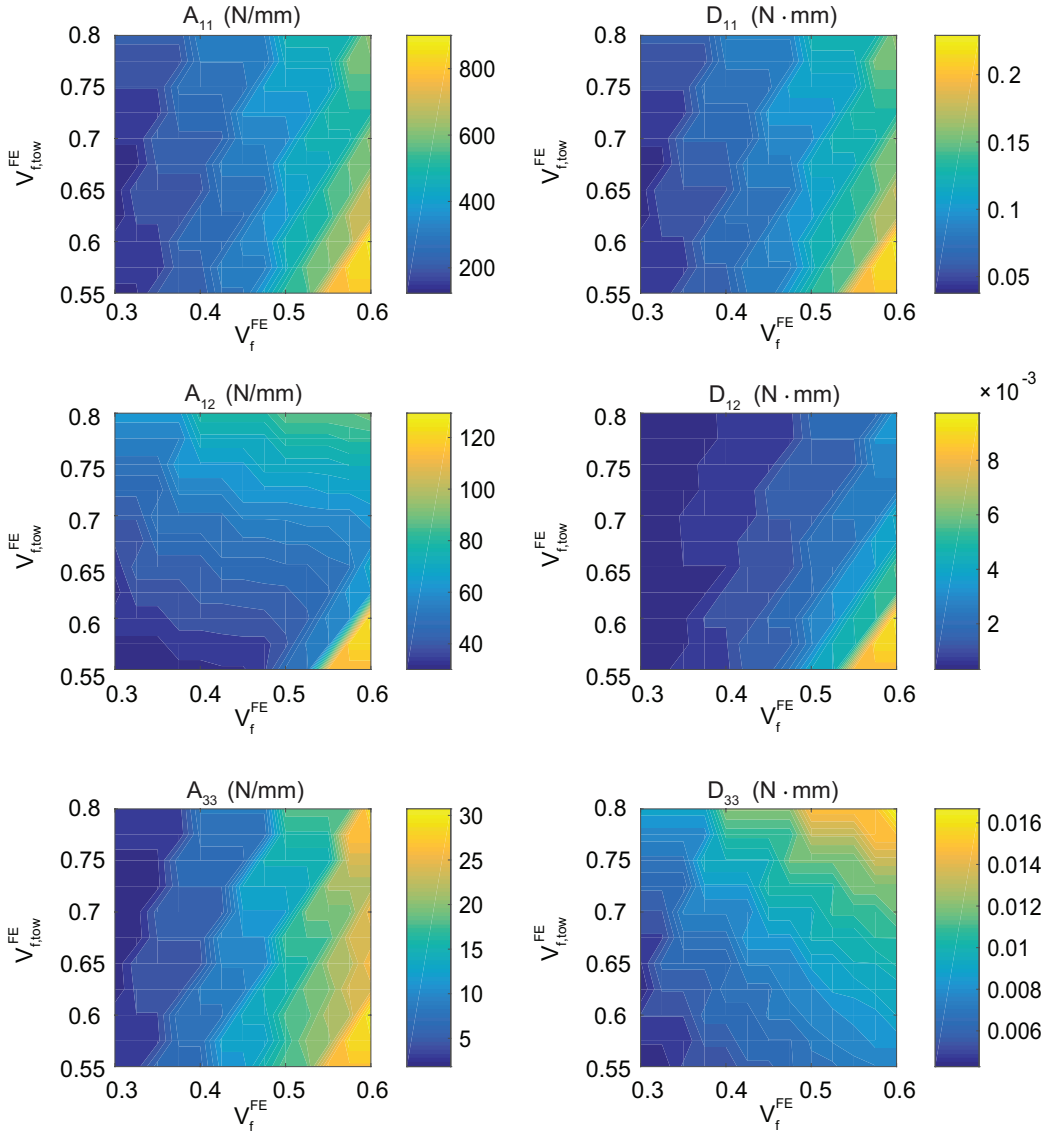

Figure 6.14: Sensitivity of the ABD matrix of a single ply of AQ/silicone composite to the composite and tow fiber volume fractions

6.6 Optimization of Woven Laminate Stiffness

The sensitivity studies above identified the tow stiffness and weave geometry as parameters significant to the stiffness of composite laminates. It was demonstrated that the geometry of the RVE weave may need to be changed significantly from the physical weave. As a result, the model geometry can be chosen to optimize agreement with experimental measurements. This is sufficient to accurately model the stiffness of the AQ/epoxy weave. However, for the AQ/silicone composite all considered values of the geometry underpredict the weave stiffness by several orders of magnitude. In this case, the tow stiffness can be modified by computation of the ξ parameter in the Halpin-Tsai model experimentally for the transverse properties.

6.6.1 Model Description

To tune the homogenization, the following optimization problem is of interest,

$$\begin{aligned}
\underset{\boldsymbol{x}}{\text{minimize}} \quad & \sum_{i=1}^{n} \left(\frac{ABD_i^{FE}(\boldsymbol{x}) - ABD_i^{exp}}{ABD_i^{exp}} \right)^2 \\
\text{subject to} \quad & 0.95V_f < V_f^{FE} < 1.05V_f, \\
& 0.95V_{f,tow} < V_{f,tow}^{FE} < 1.05V_{f,tow}, \\
& 0.9\frac{1}{2}t < h^{FE} < 1.1\frac{1}{2}t, \\
& \xi_{E_2} > 0, \\
& \xi_{G_{12}} > 0, \\
& \xi_{G_{23}} > 0.
\end{aligned} \tag{6.41}$$

where the optimization variable is,

$$\boldsymbol{x} = [\xi_{E_2} \quad \xi_{G_{12}} \quad \xi_{G_{23}} \quad h^{FE} \quad L^{FE} \quad V_f^{FE} \quad V_{f,tow}^{FE}] \tag{6.42}$$

The optimization function is the sum of squares of the errors of select ABD coefficients from corresponding experimental measurements. The composite and tow volume fractions are allowed to vary ±5% from their experimentally measured values. The model tow height can vary ±10% from the constraint in Equation 6.33. The ξ parameters of the Halpin-Tsai model used to predict the transverse tow properties must be positive, allowd to vary between the Reuss and Voigt bounds. The equal crimp ratio constrain in Equation 6.34 was removed.

The optimization problem is implemented in the Matlab software using a built-in genetic algorithm to robustly deal with the non-convex objective function and obtain a global minimum. For the initial population, the algorithm selects 100 values for $\boldsymbol{x}$. For all following generations, the

population consists of 5 values of $\boldsymbol{x}$ resulting in the best objective function value in the previous population, 80 values of $\boldsymbol{x}$ created by the scattered crossover function, and 15 values of $\boldsymbol{x}$ created through perturbation of attempted solutions [81]. The algorithm is run until the objective function value changes less than 0.01. For each value of $\boldsymbol{x}$, the framework computes tow elastic constants for the selected ξ, meshes a woven unit cell with parameters h^{FE} and L^{FE} and appropriate fiber volume fractions, and writes an Abaqus input file for modeling the woven unit cell. Four Abaqus analyses are executed to apply unit values of ε_1, ε_3, κ_1, and κ_3. The reaction forces and moments are extracted from the Abaqus output databases using Python scripts. The values of the objective function can then be computed using Matlab. This framework is illustrated in Figure 6.15.

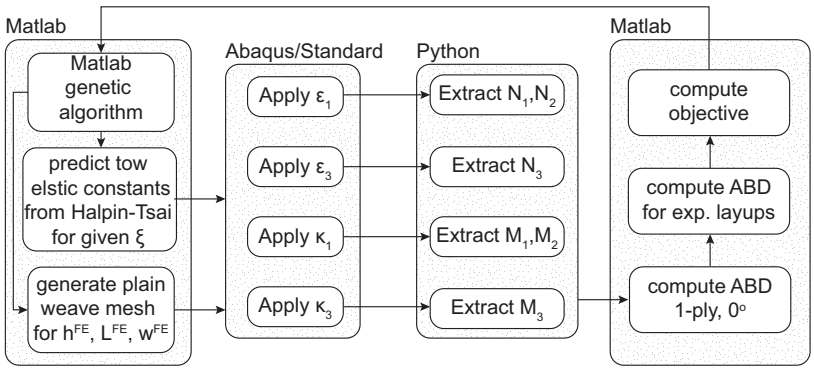

Figure 6.15: Schematic of the plain-weave stiffness optimization

6.6.2 Results

The above algorithm was applied to the two composites. Tension, A_{11}, and bending, D_{11}, measurements for $[0_3]_{pw}$ and $[45_3]_{pw}$ composite layups (column 3 of Tables 6.1 and 6.2) were used in the objective function in Equation 6.41. The data at 45° ensures that the algorithm calibrates the shear, A_{33}, and twist, D_{33}, stiffnesses for the single 0° ply in addition to A_{11} and D_{11}. Measurements at 45° are simpler than measuring the shear and twisting stiffness of the composite at 0°.

Table 6.4 shows the values of $\boldsymbol{x}$ selected by the optimization for the AQ/epoxy and AQ/silicone composites. As predicted by the sensitivity studies in Sections 6.5, modification to the geometry alone can reproduce experimental measurements of the AQ/epoxy composite. However, to reproduce measurements of the AQ/silicone composite, E_2 and G_{12} must be increased by using a higher value of ξ, in addition to modifying the geometry. Although the ξ values appear very high compared to those for the AQ/epoxy composites the overall increase in tow stiffness is not large as explained in Section 6.4.2. With the selected ξ parameters, E_2 = 23.8 GPa and G_{12} = 5.4 GPa for the AQ/epoxy tow and E_2 = 8.2 GPa and G_{12} = 2.0 GPa for the AQ/silicone tow.

It can be seen that for both composites, the selected finite element model wavelength is approximately a factor of 5 higher than the measured wavelength. The effect of increasing the wavelength

is a reduction in A_{33} and D_{33} relative to A_{11} and D_{11}, allowing the model to be accurate for all fiber angles. It is surprising that the required L^{FE} is so high relative to experiments. This may be a result of inaccuracies in matrix pocket distribution and tow shape in simulation. It is hypothesized that this is an artifact of the chosen model weave geometry and a different geometry will result in different sensitivities.

	ξ_{E_2}	$\xi_{G_{12}}$	$\xi_{G_{23}}$	h^{FE} (µm)	L^{FE} (mm)	V_f^{FE}	$V_{f,tow}^{FE}$
AQ/epoxy	5	1	0.3	43	5.5	0.52	0.78
AQ/silicone	1331	748	1.5	45	6.2	0.42	0.65

Table 6.4: Optimal solution for optimization problem

Tables 6.5 and 6.6 summarize the measured and simulated ABD stiffness coefficients of the AQ/epoxy and AQ/silicone composites using the values in Table 6.3. The first four layups in each table were the ones used for the optimization. The remaining measurements were used to test the model on other layups. The $[\pm 30/0]_{s,pw}$ AQ/epoxy measurements were made by Maqueda and are taken from [13]. The AQ/silicone $[45/0/45]_{pw}$ measurement was taken from Table 4.8. The agreement between measurement and finite element results for the AQ/epoxy composite is excellent, with simulations within 15% of experiments for all stiffnesses, including ones not used as part of the optimization. The agreement for the AQ/silicone composite is also within 15% but the average errors are observably higher. Still, good agreement is seen when predicting stiffness of layups not used in the optimization.

Stiffness Coefficient	Layup	Measurement	Finite Element	Error (%)
A_{11} (N/mm)	$[0_3]_{pw}$	4350	3703	14.8
A_{11} (N/mm)	$[45_3]_{pw}$	2727	2943	7.9
D_{11} (N·mm)	$[0_3]_{pw}$	15.2	15.6	2.6
D_{11} (N·mm)	$[45_3]_{pw}$	12.1	12.2	0.8
A_{11} (N/mm)	$[\pm 30/0]_{s,pw}$	7356	6650	9.5
D_{11} (N·mm)	$[\pm 30/0]_{s,pw}$	110	105	4.5

Table 6.5: Comparison of optimized finite element stiffness with measurements of AQ/epoxy composite

6.7 Conclusion

This work applied existing models developed for epoxy composites to the homogenization of the tows and weave of the AQ/epoxy and AQ/silicone laminates studied in this work revealing poor

Stiffness Coefficient	Layup	Measurement	Finite Element	Error (%)
A_{11} (N/mm)	$[0_3]_{pw}$	2453	2082	15.1
A_{11} (N/mm)	$[45_3]_{pw}$	1419	1247	11.0
D_{11} (N·mm)	$[0_3]_{pw}$	5.7	5.4	5.3
D_{11} (N·mm)	$[45_3]_{pw}$	2.6	3.0	15.4
D_{11} (N·mm)	$[45/0/45]_{pw}$	3.6	3.1	13.9

Table 6.6: Comparison of optimized finite element stiffness with measurements of AQ/silicone composite

agreement with experimental measurements for the silicone composite. Sensitivity studies of the weave stiffness to the model parameters identified the weave geometry and tow elastic constants, E_2 and G_{12}, as the source of the discrepancy. Hence, a modified Halpin-Tsai approach was proposed which computes parameter ξ from experimental measurements rather than the heuristic approach claiming $1 < \xi < 2$. These sensitivity studies allow for improvement of modeling of woven composites – both epoxy composites and elastomer composites.

By using axial and bending stiffness measurements at 0^o and 45^o to the weave fiber angle, the tow stiffness and model weave geometry were optimized for prediction of woven ply stiffness at any fiber orientation. The optimization framework developed here predicted laminate stiffness of both AQ/epoxy and AQ/silicone composites within 15% of experimental measurements. This held true even for laminates not part of the optimization. This is a significant improvement over the mosaic model which is known to predict bending stiffness hundreds of percent off from measurements, as shown in Section 4.8 and in [37]. Furthermore, measurement of the tow stiffness were not required for the model, as measurements of laminate stiffness are simpler to execute.

The model proposed here shows potential for improving woven composite stiffness predictions and could be improved further. In particular, the weave model used here was fixed and the only degree of freedom was its geometric parameters. As shown in Section 4.5, the AQ/epoxy and AQ/silicone composites have differing microstructures, particularly when examining the relation between tow height and ply thickness distribution. Hence, future efforts can focus on identifying model weave geometries with tow shape, thickness distributions, and matrix pockets locations that are optimized for silicone composites. Furthermore, incorporation of random fiber distributions was not addressed here due to significant increase in computation time required for parametric studies. However, considering random fiber distributions in the tow and the spread in weave geometry parameters may yield better predictions and may remove reliance on experimental stiffness measurements.

Chapter 7

Viscoelastic Characterization of Dual-Matrix Composites

7.1 Introduction

The dual-matrix composite structures studied in this work are deployed using stored strain energy from deformation of the thin shells. Folding and instantaneous deployment of such structures does not guarantee deployment after long-term storage in various thermal environments due to the viscoelastic nature of the polymer matrices used in the composites. Hence, constitutive modeling of the viscoelastic behavior of dual-matrix composites is required to guarantee deployment on orbit.

Several researchers have studied the viscoelastic behavior of composite thin shell structures. Domber et al. [82] studied viscoelastic recovery in composite hinge structures for precision optics. Soykasap et al. [33] studied experimentally the dynamic deployment of slotted composite tubes after long storage times. Brinkmeyer et al. [83] studied deployment failure in bi-stable composite tape-springs due to viscoelastic relaxation.

When studying non-woven composites, it is often assumed that the relaxation in the fiber direction is negligible, greatly simplifying the analysis. However, for woven composites, the assumption no longer holds as the undulations of the tows cause relaxation in the weave direction. The viscoelastic behavior of woven composites is also addressed in literature. Relaxation of woven composites has been studied using analytic characterization of simplified weave geometries [84, 85]. Furthermore, three-dimensional finite element models of the weave micromechanics have been used to study the relaxation of woven composites in a higher fidelity approach [17,86,87]. In particular, Zhu et al. [86] have demonstrated the improved accuracy of full 3D finite element models when studying weaves in comparison to 2D models with the plane stress assumption.

Existing studies focus on epoxy composites and there is limited information on the viscoelastic behavior of woven elastomer composites. Existing models rely on time-temperature superposition to compute long-term relaxation of the matrix using short-term test data [17,83,86]. It has been demon-

strated that elastomer materials such as silicones also follow time-temperature superposition [88,89]. Hence, to characterize the viscoelastic behavior of dual-matrix structures, this approach is followed to compute long-term relaxation curves for the constituent matrices. This data is combined with the micromechanics model developed in Chapter 6 to predict the relaxation of the dual-matrix composites for arbitrary layups. The resulting material models can be used to study behavior of dual-matrix composite structures following long storage times or storage under varying thermal environments to predict deployment reliability.

7.2 Linear Viscoelasticity

The time dependent behavior of polymers can be described by linear viscoelasticity. The uniaxial stress-strain relationship for the material can be expressed in terms of the Boltzmann superposition integral,

$$\sigma(t) = \int_0^t E(t-\tau)\frac{d\varepsilon(\tau)}{d\tau}d\tau \tag{7.1}$$

where σ is the stress, ε is the strain, and E is the time-dependent relaxation modulus. Alternatively, the constitutive relation can be expressed in terms of the time-dependent creep compliance, D,

$$\varepsilon(t) = \int_0^t D(t-\tau)\frac{d\sigma(\tau)}{d\tau}d\tau \tag{7.2}$$

Interconversion between the relaxation modulus and creep compliance can be achieved through numerical solution of the relation [90],

$$\int_0^t E(t-\tau)\frac{dD(\tau)}{d\tau} = 1 \tag{7.3}$$

The relaxation modulus and creep compliance can be expressed in terms of the Prony series representation,

$$E(t) = E_\infty + \sum_{i=0}^{n} E_i e^{-\frac{t}{\rho_i}} \tag{7.4}$$

where E_∞ is the long-term relaxation modulus, E_i are the Prony relaxation coefficients, and ρ_i are the relaxation times. Equivalently, the creep compliance can be expressed as,

$$D(t) = D_g + \sum_{i=0}^{n} D_i\left(1 - e^{-\frac{t}{\tau_i}}\right) \tag{7.5}$$

where D_g is the glassy compliance, D_i are the Prony compliance coefficients, and τ_i are the retardation times. The coefficients can be computed by fitting experimental data. Typically, the number of terms in the Prony series representation is equal to the number of decades spanned by the experimental data.

Furthermore, the above uniaxial relations can be extended to 3D,

$$\sigma_{ij}(t) = \int_0^t S_{ij}(t-\tau)\frac{d\varepsilon_j(\tau)}{d\tau}d\tau \tag{7.6}$$

where $\boldsymbol{S}$ is the relaxation modulus tensor in Voigt notation.

It is assumed here that the matrix materials under test are thermorheologically simple, meaning all processes contributing to the viscoelastic behavior of the material are equally accelerated by temperature. Hence, if one is interested in studying the long-term behavior of the material, the time-temperature superposition principle can be invoked to avoid long test times, which claims that aging of the material can equivalently be achieved through time or elevated temperatures. This principle assumes the existence of a shift factor, a_T, defined as the ratio of relaxation times at different temperatures, T,

$$a_T = \frac{\rho(T)}{\rho(T_0)} \tag{7.7}$$

where T_0 is an arbitrary reference temperature. The shift factor can be modeled by the empirical Williams-Landel-Ferry equation [91],

$$\log_{10} a_T = -\frac{c_1(T-T_0)}{c_2+T-T_0} \tag{7.8}$$

where c_1 and c_2 are material dependent constants. A reduced time, t' is introduced to capture the time and temperature dependence. For the case of isothermal test conditions,

$$t' = \frac{t}{a_T} \tag{7.9}$$

Substituting Equations 7.8 and 7.9 into Equation 7.4 yields,

$$E(t,T) = E(t',T_0) \tag{7.10}$$

which states that the relaxation modulus at time t and temperature T is the same as the relaxation modulus at reduced time t' and reference temperature T_0. Hence the time dependent relaxation modulus (or equivalently the creep compliance) can be measured using short-term tests at multiple temperatures. The long-term relaxation modulus can be computed by constructing a master curve at arbitrary reference temperature, T_0, by shifting each short-term curve by shift factor, $a_T(T)$.

7.3 Matrix Viscoelastic Characterization

To develop a general approach for modeling the viscoelastic behavior of woven composites, the long-term relaxation moduli of the constituent matrices were measured experimentally and then used as

input into the models developed in Chapter 6. The matrix materials are modeled as isotropic and linear viscoelastic. The Poisson's ratio is assumed to be time-independent and so only $E(t)$ needs to be measured. The assumption that the Poisson's ratio is constant is known to be a poor assumption but continues to be made due to difficulties in accurately measuring a time dependent Poisson's ratio experimentally [92, 93].

The procedure for characterizing the silicone matrix relaxation is detailed below. The epoxy used in this work has previously been characterized in [17] and the data is reproduced in Section 7.3.5.

7.3.1 Pure Silicone Samples

The samples used for viscoelastic characterization of the neat silicone resin were rectangular with dimensions of $178 \times 12.7 \times 2$ mm^3. The silicone was cast using three acrylic plates joined together with screws. The middle plate formed a rectangular cavity for the silicone and was covered by acrylic plates on either side. A small hole in the upper plate enabled filling the inner cavity with silicone by injecting it through a syringe. The mold was held vertically for 2 mins to allow all air bubbles to rise. The silicone was then cured under a UV lamp (Spectroline XX-15A operating at 365 nm) with an irradiance of 40 mW/cm^2 at a distance of 35 mm for 5 mins. The cured samples were subjected to a heat treatment of 48 hours at 140°C under vacuum to bake out the volatiles generated during the cure (water and methanol). Without a bake-out, the volatiles would diffuse out during the creep tests at elevated temperatures causing the samples to shrink, resulting in inaccurate strain measurements.

7.3.2 Experimental Techniques

Short-term creep tests were conducted on the silicone samples described in Section 7.3.1. The samples were clamped at two ends, with one end attached to an Instron 5569 load frame while the other end supported a mass of 580 g. Sandpaper was placed between the sample and the grips, with the rough side facing the sample, to prevent slipping. The mass resulted in ~5% strain in the silicone samples. This was verified to be in the linear regime of the material through a tension test. The setup was enclosed in an Instron 3119-506 thermal chamber which could stabilize the test temperature to within ±0.5°C. At the beginning of the test, the mass was supported by resting it on the bottom of the thermal chamber. The chamber was brought to the desired temperature and allowed to stabilize for 30 mins. Then the load frame was used to raise the sample and mass to approximate instantaneous loading. The strain in the load direction was measured for 3 hours using the LE-01 laser extensometer from Electronic Instrument Research by measuring the changing distance between two reflective tapes mounted on the sample through a window in the chamber. Two tests were conducted every 5°C from 30 – 55°C and at 65°C to construct a master curve.

7.3.3 Data Analysis

The load profile applied in the experiments can be approximated as instantaneous. Therefore, the derivative of the stress is given by,

$$\frac{d\sigma(t)}{dt} = \sigma_0 \delta(t) \tag{7.11}$$

where δ is the delta function, and $\sigma_0 = F/A$ is the applied stress, F is the force applied by the suspended mass, and A is the cross-sectional area of the samples. Substitution of Equation 7.11 into the integral in Equation 7.2 yields,

$$\varepsilon(t) = D(t)\sigma_0 \tag{7.12}$$

Therefore, the creep compliance can be obtained directly from the measured time-dependent strains. In reality, the load is not exactly a step function and so measurements taken during the first 30 mins of each test are neglected from the data to remove the effects of any transients. The creep compliance, D, is the only quantity that needs to be characterized as the material is isotropic and the Poisson's ratio is assumed to be independent of time, fixed at $\nu = 0.48$ for the silicone.

The tests at each temperature were averaged and then shifted horizontally by $a_T(T)$ until a smooth master curve was obtained. The reference temperature for the tests was 40^oC to match the reference temperature used when characterizing the epoxy resin in [17].

To work more easily with finite element codes, a relaxation modulus, $E(t)$ was obtained from the creep compliance by solving the following linear system of equations,

$$A_{ki} E_i = B_k \tag{7.13}$$

where,

$$A_{ki} = f(D_g, D_i, \rho_i, \tau_i) \tag{7.14}$$

and,

$$B_k = f(D_g, D_i, \rho_i, \tau_i) \tag{7.15}$$

The full closed form expression for A_{ki} and B_k are included in Appendix B. The derivation of Equation 7.13 follows an analogous procedure to that in [90] and is included in Appendix B.

7.3.4 Silicone Master Curve

The averaged creep compliance at each test temperature is shown in Figure 7.1. As expected, the compliance increases with temperature. This data can be shifted horizontally using Equation 7.9 relative to the curve at the reference temperature $T_0 = 40^o$C to assemble a long-term creep compliance for up to 1 year in storage.

The shift factors, a_T, used for assembling the silicone master curve are plotted as a function of

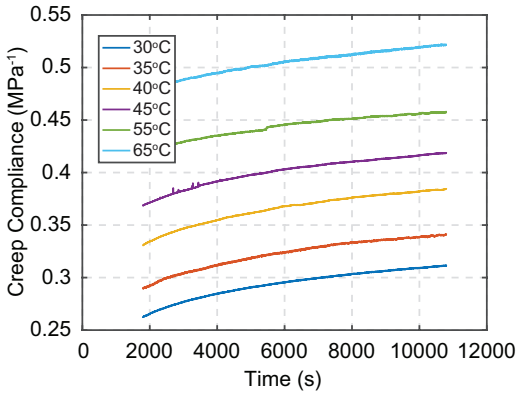

Figure 7.1: Creep test data for neat silicone samples

temperature in Figure 7.2. The Williams-Landel-Ferry model (Equation 7.8) is fitted to the data to compute constants c_1 and c_2 for the silicone. The resulting fit values are c_1 = 9.2 and c_2 = 91.6 K. These values agree well with those found for a large range of polymers in [91].

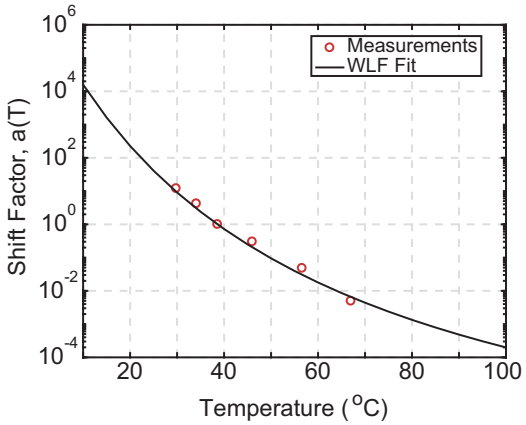

Figure 7.2: Shift factors for silicone and WLF fit

The shifted data was fitted using a Prony series representation in Equation 7.5 using a least-squares fit with the Levenberg-Marquardt algorithm, with the retardation times used given in column 2 of Table 7.1. The Prony series representation for the relaxation modulus is computed numerically using Equation 7.13. Both Prony series are plotted in Figure 7.3 and the values for the coefficients are given in Table 7.1.

7.3.5 Epoxy Master Curve

The PMT-F4B epoxy matrix used here for the AQ/epoxy composite has already been characterized in [17] through creep tests. The resulting isotropic relaxation modulus is shown in Figure 7.4. The computed Prony series for the epoxy matrix is reproduced in Table 7.2.

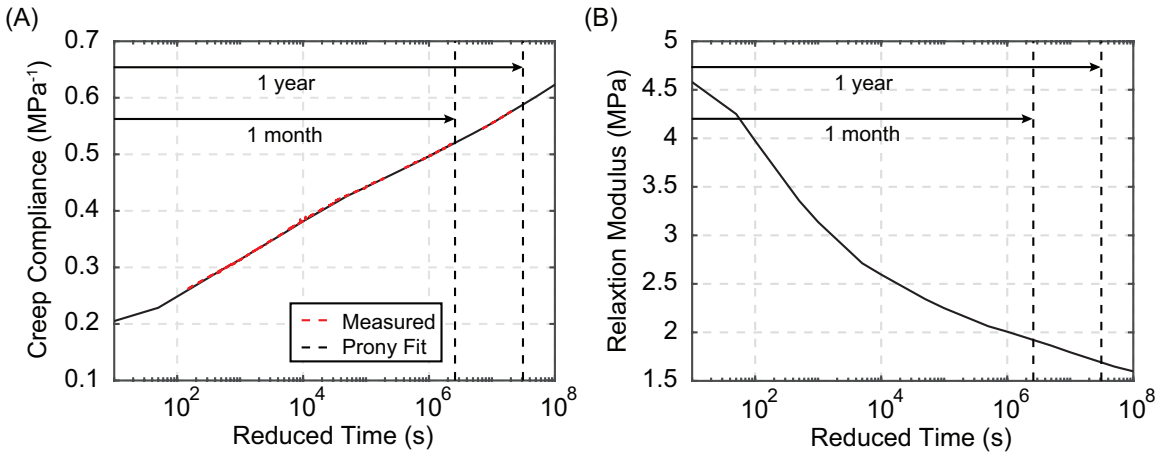

Figure 7.3: Prony series fit of silicone viscoelastic moduli (A) creep compliance (B) relaxation modulus

i	$\tau_i = \rho_i$ (s)	D_i (MPa^{-1})	E_i (MPa)
g/∞	-	0.1978	1.5253
1	1×10^2	0.0696	0.9930
2	1×10^3	0.0617	0.8087
3	1×10^4	0.0741	0.3965
4	1×10^5	0.0522	0.3410
5	1×10^6	0.0551	0.1756
6	1×10^7	0.0571	0.2432
7	1×10^8	0.0881	0.1989

Table 7.1: Prony series representation of Loctite 5055 silicone creep compliance and relaxation modulus

i	ρ_i (s)	E_i (MPa)
∞	-	1000
1	1×10^3	224.1
2	1×10^5	450.8
3	1×10^6	406.1
4	1×10^7	392.7
5	1×10^8	810.4
6	1×10^9	203.7
7	1×10^{10}	1486.0

Table 7.2: Prony series representation of PMT-F4 epoxy relaxation, reproduced from [17]

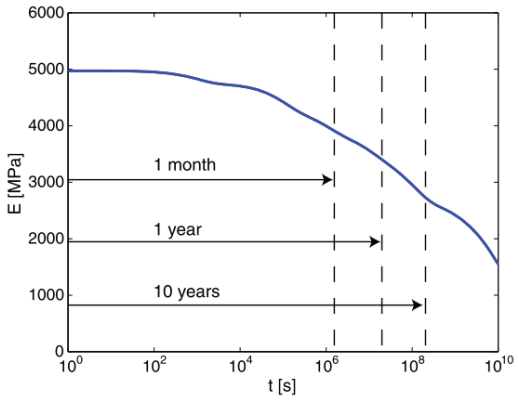

Figure 7.4: Relaxation modulus of PMT-F4 epoxy resin, reproduced from [17]

7.4 Modeling of Woven Viscoelastic Composites

7.4.1 Model Description

The modified Halpin-Tsai analytic method developed in Section 6.4.2 was used to predict the tow relaxation moduli. The relaxation modulus of the matrix, $E_m(t)$, and a constant Poisson's ratio was used to model the matrix. The fibers were assumed to be elastic and isotropic. This model computed the time-dependent elastic constants of the tow. The relaxation moduli of the tow, $S_{ij}(t)$, were computed using Equations 6.1 – 6.2. The ξ parameters matched the optimized values in Table 6.4.

The time-dependent ABD matrix was computed using the finite element RVE described in Section 6.3.1. The matrix was modeled as viscoelastic using the built linear viscoelastic material model in Abaqus/Standard. The `*Elastic, moduli = long term` keyword was used to specify E_∞ and the Poisson's ratio and the `*Viscoelastic, time = prony` keyword was used to specify the Prony coefficients and relaxation times. A UMAT user subroutine was used to define the viscoelastic behavior of the tows in terms of the tow relaxation moduli, S_{ij}, computed in the first homogenization step. The UMAT was written by Kwok and is available in [94]. The geometry of the unit cell matched the optimized parameters in Table 6.4.

7.4.2 Results and Experimental Validation

The tow relaxation moduli for the AQ/epoxy and AQ/silicone composites are shown in Figure 7.5. As expected intuitively, the relaxation in the fiber direction, $S_{11}(t)$, is negligible for both composites. The Prony series representation of the composite tows are given in Tables 7.3 and 7.4 for the AQ/epoxy and AQ/silicone composites, respectively. These coefficients are used as input into the weave homogenization.

The time-dependent ABD matrices for a single ply of the two composites are shown in Figure

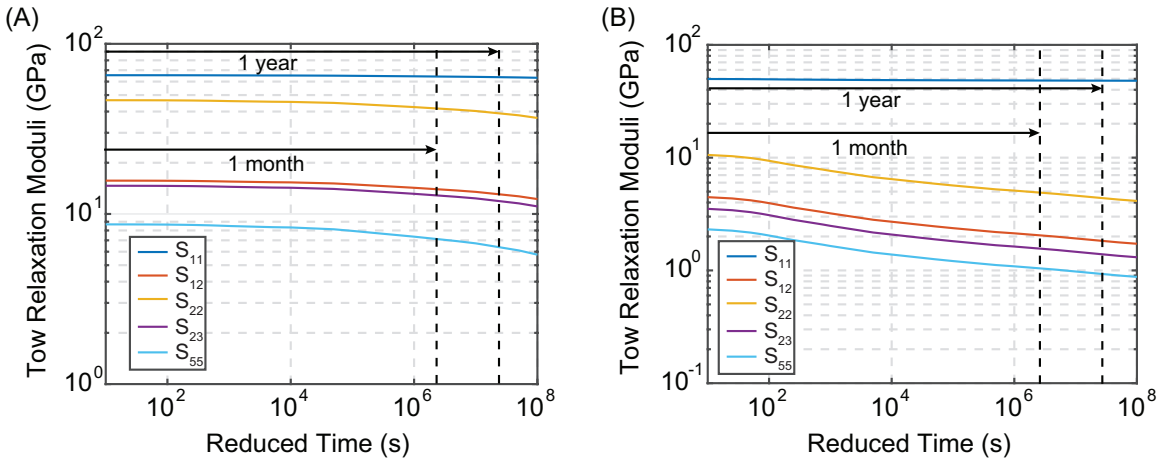

Figure 7.5: Finite element prediction of tow relaxation moduli (A) AQ/epoxy composite (B) AQ/silicone composite

i	$\tau_i = \rho_i$ (s)	S_{11} (MPa)	S_{12} (MPa)	S_{22} (MPa)	S_{23} (MPa)	S_{55} (MPa)
∞	-	59776	6432.3	19665	5438.6	2282.7
1	1×10^3	203.5	301.6	860.0	316.9	292.8
2	1×10^5	424.0	635.1	1811.6	666.8	604.0
3	1×10^6	448.6	702.1	2018.3	721.9	588.7
4	1×10^7	298.3	609.7	1737.7	641.7	558.1
5	1×10^8	1123.3	1846.2	5355.8	1849.5	1311.3
6	1×10^9	200.8	305.0	842.3	341.8	308.0
7	1×10^{10}	2821.4	4871.6	14339	4673.9	2743.3

Table 7.3: Prony series representation of AQ/epoxy tow relaxation moduli

i	$\tau_i = \rho_i$ (s)	S_{11} (MPa)	S_{12} (MPa)	S_{22} (MPa)	S_{23} (MPa)	S_{55} (MPa)
∞	-	48047	1649.1	3954.7	1250.7	837.8
1	1×10^2	532.3	839.5	195.5	696.6	447.2
2	1×10^3	470.9	742.8	174.5	599.7	389.7
3	1×10^4	236.0	372.2	876.9	297.9	194.4
4	1×10^5	210.5	332.1	785.6	262.7	274.0
5	1×10^6	109.1	172.1	407.5	135.6	89.1
6	1×10^7	154.2	243.3	577.6	190.5	125.6
7	1×10^8	128.2	202.2	481.1	157.3	104.0

Table 7.4: Prony series representation of AQ/silicone tow relaxation moduli

7.6. It is interesting to note that for the AQ/silicone ply, the A_{12} coefficient increases slightly with time. Both composites show moderate drops in extensional stiffness, A_{11}, of ~20% and a larger drop in the shear stiffness, A_{33}, of ~40%. However, the AQ/silicone composite shows a larger decrease in bending stiffness, D_{11}, of 40% as compared to only 31% for the AQ/epoxy. Similarly, the drop in twisting stiffness, D_{33}, is 50% for the AQ/silicone composite and only 37% for the AQ/epoxy.

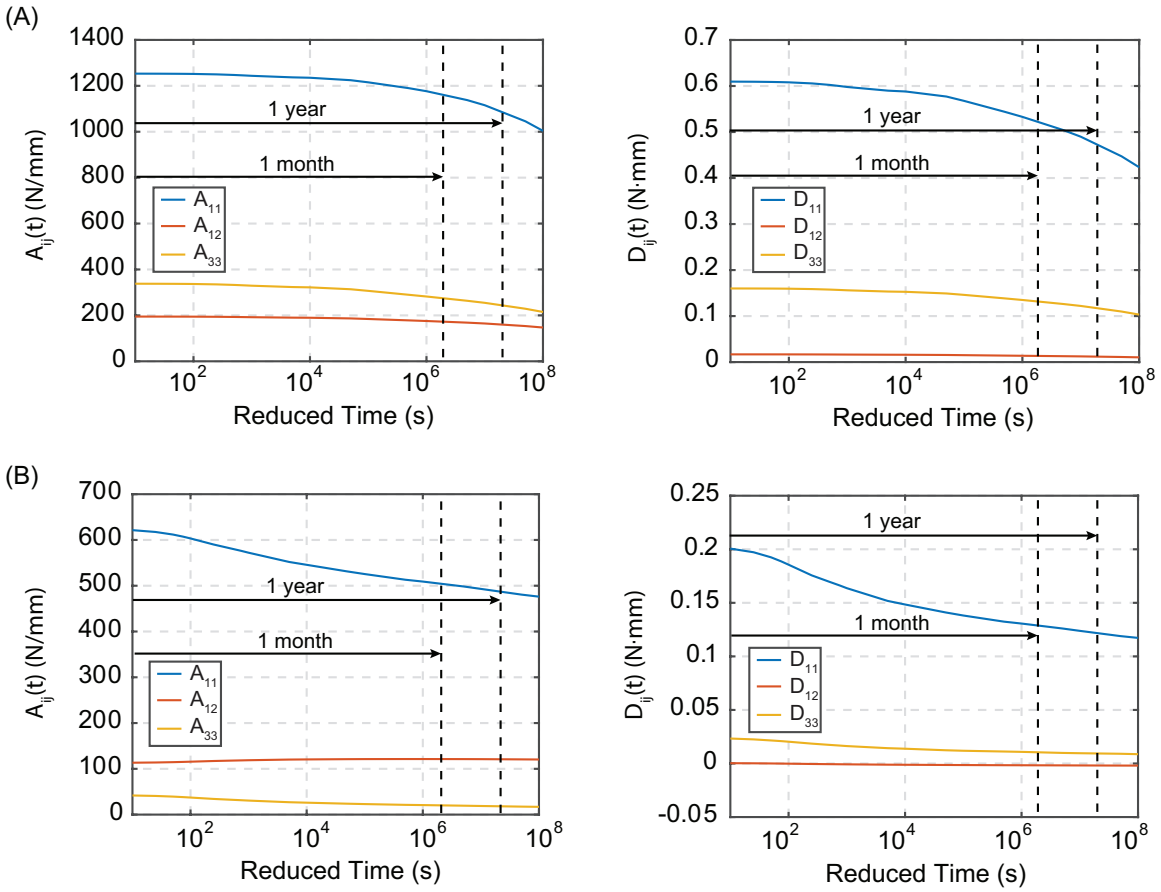

Figure 7.6: Finite element prediction of time-dependent ABD stiffness for $[0]_{pw}$ (A) AQ/epoxy composite (B) AQ/silicone composite

Classical lamination theory is used to predict the relaxation in bending stiffness of a $[45_3]_{pw}$ layup of the AQ/epoxy and AQ/silicone composites using the data in Figure 7.6. The predictions are compared to experimental measurements of relaxation for this laminate in Figure 7.7. The finite element predictions were shifted to a reference temperature of $T_0 = 40^{\circ}$C as they were computed with the parameter values given in Table 6.4 which were optimized using data at room temperature. The shift factors used were $a_T(T = 22^{\circ}\text{C}) = 9.2$ for the AQ/epoxy composite and $a_T(T = 22^{\circ}\text{C}) = 38.4$ for the AQ/silicone composite, obtained by fitting Equation 7.8 to the shift factors used for the experimental data in Figure 7.7. The need for shifting can be removed by optimization of the finite element parameters (i.e., tow stiffness and RVE weave geometry) using experimental data measured at the reference temperature.

The agreement between finite element predictions and measurements is within 11% for the AQ/epoxy laminate and within 18% for the AQ/silicone laminate. These are similar values to the errors found in Chapter 6 for the elastic data. A slightly larger error is seen here due to the assumption that the Poisson's ratio of the silicone and epoxy matrices is time-independent.

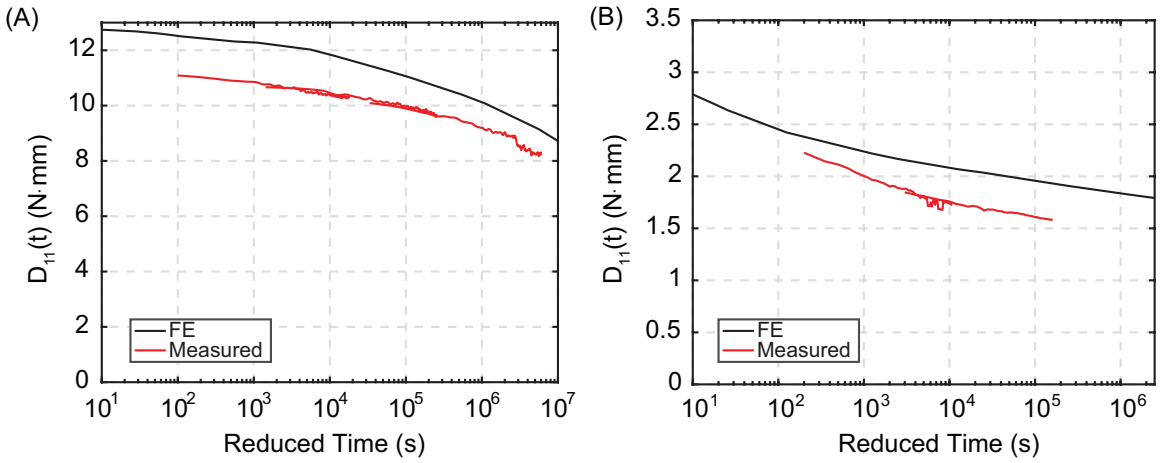

Figure 7.7: Finite element prediction of D_{11} relaxation for $[45_3]_{pw}$ layup and comparison with experimental measurements (A) AQ/epoxy composite (B) AQ/silicone composite

7.5 Conclusion

The model developed in Chapter 6 was extended to viscoelasticity here. An accurate model for the viscoelastic behavior of woven composites is of particular importance due to the long test times associated with characterizing viscoelastic materials. The model here uses only the matrix relaxation measurements and fiber elastic properties to predict the relaxation of arbitrary composite layups. The matrix master curves were obtained using the principle of time-temperature superposition in order to reduce test times. Comparison of model predictions for the relaxation of a $[45_3]_{pw}$ layup to experimental measurements showed agreement within 11% for the AQ/epoxy composite and 18% for the AQ/silicone composite.

Predicting of the extent of relaxation in the two composites will help investigate the deployment of dual-matrix composites structures in future studies. In particular, the time-dependent ABD matrices developed here can be used in finite element simulations of long-term stowage followed by dynamic deployment to predict deployment failure as well as the times required for viscoelastic recovery of the deployed structure.

Chapter 8

Conclusions

There were four main research objectives set for this work:

1. Development of scaling relations between structural and electromagnetic performance of deployable antennas to enable rapid design and concept comparison.

2. Evaluation of dual-matrix composites as a novel approach to deployable antennas including prototype design, analysis and testing.

3. Investigation of modeling and experimental techniques addressing the quasi-static deployment of dual-matrix composites to enable design of deployment mechanisms.

4. Development of modeling techniques for woven elastomer composites for the accurate prediction of elastic and viscoelastic properties of dual-matrix composite structures.

To address the first objective, a novel methodology for presenting deployable antenna performance in terms of its geometry has been proposed. Existing deployable CubeSat antennas have been parametrized in terms of their heights and diameters to provide a common framework for describing concept performance. The structural and electromagnetic performance of these concepts was computed analytically or interpolated from experimental data to enable rapid prediction of achievable performance of each concept. Plotting performance as a function of geometry on a set of 2D co-ordinated plots, complete with design requirements, has allowed designers to visualize the performance of various concepts relative to each other and select specific designs meeting all requirements. The proposed methodology was applied to compare the performance of dual-matrix composite antennas to existing off-the-shelf designs. It was demonstrated that dual-matrix composites can enable high gain, broadband antennas with high bit rates capable of packaging very efficiently compared to existing designs. In particular, the use of this tool to evaluate dual-matrix composite antennas enabled the design of a conical log spiral (CLS) antenna for CubeSats.

The second research objective was addressed by designing, fabricating, and testing a particular CLS antenna prototype as a follow-on to the initial design suggested by the rapid design methodology.

Not only was the geometry of the CLS optimized to increase gain and bandwidth using finite element simulations, but the interaction of the antenna with the CubeSat from which it is deployed was also considered. A deployment scheme utilizing a dual-matrix composite hinge to stow the antenna inside the satellite for launch and to separate it from the satellite on orbit was proposed. All parts of the integrated satellite assembly were fabricated including the antenna, the hinge, and a custom flexible feed network to fold inside the antenna for launch. Structural and electromagnetic testing was conducted on the fabricated prototypes verifying finite element predictions of antenna performance and revealing that the antenna gain, bandwidth, and structural vibration frequencies are unaffected by antenna folding. This indicates that the deployment accuracy of the proposed scheme is sufficient for application to antennas operating at UHF frequencies.

The quasi-static deployment of dual-matrix composites was tackled by studying the behavior of a dual-matrix hinge experimentally, analytically, and though finite element simulations. An energy approach was applied to the hinge structure to analytically predict its folded shape and deployment moments. Furthermore, finite element models were developed using the LS-Dyna commercial software to study these metrics. Taking advantage of the robust re-start capabilities of LS-Dyna as well as its stable contact algorithms, an approach was developed to significantly reduce simulation times for this problem. The models developed were used to demonstrate control of the folded shape of the dual-matrix hinge through the bending stiffness of the elastomer composite fold lines. Comparison of model predictions with experimental measurements of the folded shape and deployment moments yielded excellent agreement within 5% for all metrics, enabling future design of deployment mechanisms for dual-matrix composites.

Finally, the prediction of stiffness of woven elastomeric composites used in the dual-matrix structures in this research was done through a combined analytic and finite element RVE approach. Application of existing models for woven composites developed for epoxy composites was shown to significantly underpredict the tow stiffness of elastomer composites. As a result, an RVE of the composite weave was combined with a semi-empirical approach using a modified Halpin-Tsai model where the reinforcing efficiency for each tow elastic constant was computed from experimental measurements of the composite ply stiffness. By using measurements of the composite stiffness at two fiber angles, the model could be tuned to predict stiffness of any arbitrary composite layup. Application of the model to the composites used in the dual-matrix structures proposed in this work showed the capability to predict both extensional and bending stiffness of arbitrary layups within 15% of measurements, a significant improvement over the commonly used mosaic model for woven composites which has shown errors as large as 100% for bending stiffness of woven composites. Furthermore, the model is general enough to predict stiffness of both epoxy and silicone composites. The model developed was extended to the prediction of viscoelastic behavior of dual-matrix composites.

8.1 Contributions

The present research has made several contributions to the field of deployable structures and composite materials. In particular, several prototypes developed as part of this research are useful for deployable structures applications:

- A prototype of a deployable dual-matrix antenna with structural and electromagnetic performance fully tested for use as a high bit-rate deployable CubeSat antenna for low Earth orbit operating at UHF.
- A closed-cross section dual-matrix deployable hinge for use in space structures requiring high torsional stiffness and high deployed precision. The hinge can be used to build larger hinged or coilable booms as well as deployable truss structures.
- Flexible broadband feed lines to use in place of traditional, stiff co-axial cables to facilitate more efficient packaging of thin shell structures.

In addition to the physical prototypes produced, several analysis tools and techniques have been developed in this work:

- A user interface implementing the rapid design methodology and concept comparison for deployable CubeSat antennas. The methodology itself is general enough to applied to any type of deployable structure design, of particular use to multi-disciplinary design problems. Users can add their own antenna designs through stand alone functions.
- Analytic and finite element methods for analysis of quasi-static deployment of dual-matrix composites applicable beyond the hinge structure analyzed in this work. The analytic model accounts for fiber microbuckling during stowage to predict folded shape and deployment moments within 5% of experiments.
- A novel model for prediction of the elastic stiffness and viscoelastic relaxation of woven composites – applicable to both traditional epoxy resins and elastomer matrices. The technique has been shown to predict stiffness of arbitrary layups within 15% of measurements, a significant improvement over the commonly used mosaic model with errors of up to 100% when predicting stiffness.
- The understanding of the behavior of silicone composites has been improved in this work through several contributions showing them to be applicable to deployable space structures. In particular, it was demonstrated that folding and instantaneous deployment of silicone composite hinges has no detrimental effects of the performance of dual-matrix structures. Furthermore, the viscoelastic behavior has been characterized enabling studies of the effects of long term stowage.

8.2 Future Work

A natural extension of the dual-matrix antennas built here is to antennas operating at higher frequencies to enable even higher bit-rates. Scaling to higher frequencies would be advantageous where extremely high gain antennas are required (e.g., for deep space missions). As the mass and volume are even more restricted for such applications, dual-matrix composites could provide a lightweight and efficient packaging scheme. However, antennas operating at this frequency require higher shape accuracy and dimensional stability. This is not an aspect of the behavior of dual-matrix composites that has been studied in detail as this work only showed functionality in the UHF band by measuring antenna performance rather than directly measuring the deployed shape. Precise measurements of the deployed accuracy of these structures is required (e.g., with DIC or photogrammetry). Research into methods of improving shape accuracy of dual-matrix structures could follow including design of stiffening elements out-of-plane of the shell. Furthermore, automation of the fabrication techniques is required for manufacture of more precise structures with complex folding schemes that will be required for such applications. These studies would benefit the development of high surface accuracy deployable structures for space applications in general, including large aperture telescopes and large deployable booms.

In addition, the large configuration changes achievable by dual-matrix composites make them of interest to reconfigurable space structures. This includes mechanically reconfigurable antennas which can change their radiation pattern or operating frequency in response to changing mission requirements. To enable such applications, the fatigue behavior of dual-matrix composites should be investigated. Moreover, the elastomer hinges would need to be combined with an actuation scheme to enable configurations other than fully packaged and fully deployed. These actuation schemes would need to be lightweight, ideally embedded in the composite shells, and able to actuate the structure to both deploy and stow reversibly.

At the material modeling level, the work done here to develop tools for predicting the stiffness of woven elastomer composites is only the beginning. The modified Halpin-Tsai model proposed here begs the question of whether there is a heuristic value for the reinforcing parameter, ξ, valid for elastomer composites just like there is one for epoxy composites. The answer to this question requires a more experimental data on elastomer composites than is currently available. The rationale for using higher values of ξ in this work was to account for out-of-plane misalignment in the angles of the fibers which work to reinforce the transverse composite tow response. However, this hypothesis has not been verified here. Experimental observation of these misalignments (e.g., using micrographs or X-ray CT scans) as well as 3D finite element models of the composite tows which include these misalignments are required to address this issue.

Finally, this work focused on the quasi-static deployment of dual-matrix structures. However,

their dynamic deployment is just as critical to their performance. The viscoelastic characterization done as part of this work enables studies of long storage and subsequent deployment of dual-matrix composite structures to characterize their deployment reliability and viscoelastic shape recovery.

Appendix A

Design Equations for Electromagnetic and Structural Performance Metrics

Table A.1: Design equations for electromagnetic performance metrics

Antenna Type	**Gain,** G	**Fractional Bandwidth,** $BW(\%)$	**Polarization**
Half-wavelength Dipole	1.643	3	linear
Single Helix	$\frac{15(\pi D)^2 h}{\lambda^3}$	56	circular
Conical Log Spiral	Interpolated from experimental data in [46]	Interpolated from experimental data in [46]	circular
Conical Horn	$20\log\left(\frac{\pi D}{\lambda}\right) - \ell$ where, $\ell = 2.912$ for optimum	$40 < BW < 75$	linear/circular
Patch	$\frac{2}{15 G_{rad}}\left(\frac{D}{\lambda}\right)^2$	$\frac{\epsilon_r - 1}{\epsilon_r^2}\frac{Dt}{h}$	linear/circular
Reflector	$\left(\frac{\pi D}{\lambda}\right)^2 \epsilon_{ap}$	$5 < BW < 10$	various
Yagi-Uda	Interpolated from experimental data in [48]	Interpolated from experimental data in [48]	linear

Table A.2: Design equations for structural performance metrics

Antenna Type	**Folding Scheme**	**Packaged Dimensions,** L_1, L_2, L_3	**Packaging Ratio,** p	**Fundamental Frequency,** f_0
Dipole	Hinge	$L_1 = h$ $L_2 = L_3 = D_{wire}$	1	$\frac{3.516}{2\pi h^2}\sqrt{\frac{EI}{\rho_l}}$
	Tape-springs	$L_1 = \frac{h}{i}$ $L_2 = L_3 = D_{wire}$		
Helix	Helical pantographs	$L_1 = L_2 = 2\sqrt{\left(\frac{D}{2}\right)^2 + \left(\frac{h}{N}\right) - \left(\frac{a}{2\pi}\right)}$ $L_3 = \frac{3}{2}hD_{wire}$	$\frac{D^2 h}{2ND_{wire}L_1}$	$\frac{D_{wire}}{4\pi D^2 N}\sqrt{\frac{E}{\rho(1+\nu)}}$
	Coilable conductors	$L_1 = 2ND_{wire}$ $L_2 = L_3 = \frac{1}{\pi}\sqrt{(\pi D)^2 + \left(\frac{h}{N}\right)^2 - 4D_{wire}^2}$	$\frac{D^2 h}{L_1 L_2^2}$	
	Z-Folding	$L_1 = h$ $L_2 = \frac{\pi D}{i}$ $L_3 = 3ti$	$C_1 D$ where, $C_1 = 50\ \mathrm{m}^{-1}$	$\frac{3}{8\pi}\frac{h}{D}\sqrt{\frac{E}{\rho_a(1\nu^2)}}$

Antenna Type	**Folding Scheme**	**Packaged Dimensions,** L_1, L_2, L_3	**Packaging Ratio,** p	**Fundamental Frequency,** f_0
Helix	Miura-Ori	$L_1 = L_2 = \frac{\pi D}{2i}$ $L_3 = \frac{\pi D}{2i}\tan\phi + \frac{h}{j}$	$C_1 D$ where, $C_1 = 50\ \mathrm{m}^{-1}$	$\frac{3}{8\pi}\frac{h}{D}\sqrt{\frac{E}{\rho_a(1\nu^2)}}$
Conic horn and CLS	Z-Folding	$L_1 = g\left[1 + \left(\frac{D\cot\theta}{2h} - 1\right)\left(1 - \cos\frac{\theta_0}{2i}\right)\right]$ $L_2 = 2g\frac{D\cot\theta}{2h}\sin\frac{\theta_0}{2i}$ $L_3 = 3ti$ where, $g = h\sqrt{\tan^2\theta + 1}$ $\theta_0 = \frac{\pi h\tan\theta}{g}$	$C_2\frac{Dh}{\sqrt{h^2 + \frac{D^2}{4}}}$ where, $C_2 = 133\ \mathrm{m}^{-1}$	$\frac{2h}{\sqrt{15}\pi D^2}(3 - 4\sin\left(\frac{3\theta}{4}\right))\sqrt{\frac{E}{\rho(1-\nu^2)}}$ where, $\tan\theta = \frac{D}{2h}$
	Miura-Ori	$L_1 = L_2 = \frac{\pi D}{2i}$ $L_3 = \frac{\pi D}{2i}\tan\phi + \frac{1}{j}\sqrt{h^2 + \frac{D^2}{4}}$		
Patch	Fixed	$L_1 = h$ $L_2 = D$ $L_3 = t$	1	$\frac{a}{2\pi h^2}\sqrt{\frac{Et^3}{12\rho(1-\nu^2)}}$ where, $a = f\left(\frac{h}{D}\right)$ can be found in [51]

Antenna Type	**Folding Scheme**	**Packaged Dimensions,** L_1, L_2, L_3	**Packaging Ratio,** p	**Fundamental Frequency,** f_0
Reflector	Hinged Ribs	$L_1 = L_2 = \frac{D}{10}$ $L_3 = \frac{h}{2}\tan^{-1}\left\lvert\frac{\frac{h}{2D}}{(\frac{h}{D})^2 - \frac{1}{16}}\right\rvert$	$\frac{D^2 h}{L_1^2 L_3}$	$\min\left(\frac{2t^2}{\pi h^3}\sqrt{\frac{E}{\rho}}\frac{g_1}{g_2}, \frac{3}{8\pi}\frac{h}{D_{hub}}\sqrt{\frac{E}{\rho_{hub}(1+\nu)}}\right)$ where, $\frac{g_1}{g_2} = f(\theta_0)$ can be found in [47]
	Wrapped Mesh	$L_1 = \frac{\pi D}{i}$ $L_2 = L_3 = D_{hub} + 3t\cot\frac{\pi}{i}$	$\frac{iDh}{4L_2^2}$	
Yagi-Uda	Tape-springs	$L_1 = D_{wire}(\pi + 2)$ $L_2 = \frac{\pi}{2}D_{wire}$ $L_3 = D_{wire}$	$\frac{2hD}{D_{wire}^2(\pi+2)}$	$\frac{0.621}{h^2}\sqrt{\frac{EtD_{wire}^3}{\pi\rho_l}}$

Appendix B

Interconversion Between Creep Compliance and Relaxation Modulus

This appendix outlines the interconversion from creep compliance to relaxation modulus following the methods proposed in [90].

The interconversion can be done by solving,

$$\int_0^t E(t-\tau)\frac{dD(\tau)}{d\tau}d\tau = 1 \tag{B.1}$$

where the creep compliance, $D(t)$, and the relaxation modulus, $E(t)$, can be expressed in terms of their respective Prony series representations,

$$D(t) = D_g + \sum_{j=1}^{n} D_j \left(1 - e^{-t/\tau_j}\right) \tag{B.2}$$

and,

$$E(t) = E_\infty + \sum_{i=1}^{m} E_i e^{-t/\rho_i} \tag{B.3}$$

Substitution of Equations B.2 and B.3 into Equation B.1 yields,

$$\int_0^t \left[E_\infty + \sum_{i=1}^{m} E_i e^{-(t-\tau)/\rho_i}\right]\left[D_g\delta(\tau) + \sum_{j=1}^{n}\frac{D_j}{\tau_j}e^{-\tau/\tau_j}\right]d\tau = 1$$

$$D_g[E_\infty + \sum_{i=1}^{m} E_i e^{-t/\rho_i}] + E_\infty \sum_{j=1}^{n}\frac{D_j}{\tau_j}\int_0^t e^{-\tau/\tau_j}d\tau + \sum_{i=1}^{m}\sum_{j=1}^{n}\frac{E_i D_j}{\tau_j}e^{-t/\rho_i}\int_0^t e^{-(\tau/\tau_j - \tau/\rho_i)} = 1 \tag{B.4}$$

The remaining integrals can be evaluated as follows,

$$\int_0^t e^{\tau/\tau_j}d\tau = \tau_j(1 - e^{-t/\tau_j}) \tag{B.5}$$

and,

$$\int_0^t e^{-(\tau/\tau_j - \tau/\rho_i)} = \begin{cases} \frac{\rho_i \tau_j}{\rho_i - \tau_j}(1 - e^{-(t/\tau_j - t/\rho_i)}) & \rho_i \neq \tau_j \\ t & \rho_i = \tau_j \end{cases} \tag{B.6}$$

Equation B.4 can be solved by collocation at times $t_k = \tau_j$. in this case, Equation B.4 can be re-expressed as a system of linear equations,

$$A_{ki} E_i = B_k \tag{B.7}$$

where,

$$A_{ki} = \begin{cases} D_g e^{-t_k/\rho_i} + \sum_{j=1}^{n} \frac{D_j \rho_i}{\rho_i - \tau_j} \left(e^{-t_k/\rho_i} - e^{-t_k/\tau_j} \right) & \rho_i \neq \tau_j \\ D_g e^{-t_k/\rho_i} + \sum_{j=1}^{n} \frac{D_j t_k}{\tau_j} e^{-t_k/\rho_i} & \rho_i = \tau_j \end{cases} \tag{B.8}$$

and,

$$B_k = 1 - E_\infty [D_g + \sum_{j=1}^{n} D_j \left(1 - e^{-t_k/\tau_j} \right)] \tag{B.9}$$

where the long term-term modulus, E_∞, is given by,

$$E_\infty = \frac{1}{D_g + \sum_{j=1}^{n} D_j} \tag{B.10}$$

Park et al. showed that taking $\tau_i = \rho_i$ is a good assumption resulting in little error [90].

Bibliography

[1] Canadian Space Agency, "CubeSat," 2017. [Online]. Available: www.asc-csa.gc.ca/eng/satellites/cubesat/default.asp

[2] ISIS, "Deployable dipole antenna system," 2016. [Online]. Available: www.cubesatshop.com/product/dipole-antenna-system/

[3] Endurosat, "S-Band Patch Antenna," 2018. [Online]. Available: https://www.endurosat.com/products/cubesat-s-band-patch-antenna/

[4] Northrop Grumman, "AstroMesh," 2018. [Online]. Available: www.northropgrumman.com/BusinessVentures/AstroAerospace/Products/Pages/AstroMesh.aspx

[5] J. Sauder, N. Chahat, M. Thomson, R. Hodges, E. Peral, and Y. Rahmat-Samii, "Ultra-Compact Ka-Band Parabolic Deployable Antenna for Radar and Interplanetary CubeSats," in *29th Annual AIAA/USU Conference on Small Satellites*, Logan, Utah, 2015.

[6] K. Dontchev, "Michigan Multipurpose MiniSat M-Cubed," in *Summer CubeSat Workshop*, San Luis Obispo, CA, USA, 2009.

[7] H. C. Technologies, "Helios Deployable Antenna," 2004. [Online]. Available: https://www.helicomtech.com/helios-deployable-series

[8] C. S. Macgillivray, "Miniature Deployable High Gain Antenna for CubeSats," in *CubeSat Developers Workshop*, San Luis Obispo, California, 2011.

[9] R. Charles, "Design, Construction and Testing of the Deployable UHF Antenna for SKYNET 4, Stage 2," in *IUTAM-IASS Symposium on Deployable Structures: Theory and Applications*, Cambridge, UK, 1998, pp. 77–86.

[10] S. A. Robinson, "Simplified Spacecraft Antenna Reflector for Stowage in Confined Envelopes," 1996.

[11] W. H. Francis, M. S. Lake, and J. S. Mayes, "A review of classical fiber microbuckling analytical solutions for use with elastic memory composites," in *47th AIAA/ASME/ASCE/AHS/ASC Structures, Structural Dynamics, and Materials Conference, 1 - 4 May 2006, Newport, Rhode Island*, Newport, Rhode Island.

[12] K. Saito, S. Pellegrino, and T. Nojima, "Manufacture of Arbitrary Cross-Section Composite Honeycomb Cores Based on Origami Techniques," *Journal of Mechanical Design*, vol. 136, no. 5, pp. 1–9, 2014.

[13] I. Maqueda, "High-strain composites and dual-matrix composite structures," Ph.D. dissertation, California Institute of Technology, 2014.

[14] G. M. Olson, S. Pellegrino, J. Banik, and J. Costantine, "Deployable Helical Antennas for CubeSats," in *54th AIAA/ASME/ASCE/AHS/ASC Structure, Structural Dynamics, and Materials Conference*, Boston, Massachusetts, 2013.

[15] M. Sakovsky, I. Maqueda, C. Karl, and S. Pellegrino, "Dual-Matrix Composite Wideband Antenna Structures for CubeSats," in *AIAA SciTech*, Orlando, Florida, 2015.

[16] Y. Huang, K. K. Jin, and S. K. Ha, "Effects of fiber arrangement on mechanical behavior of unidirectional composites," *Journal of Composite Materials*, vol. 42, no. 18, pp. 1851–1871, 2008.

[17] K. Kwok and S. Pellegrino, "Micromechanics Models for Viscoelastic Plain-Weave Composite Tape Springs," *AIAA Journal*, vol. 55, no. 1, pp. 309–321, 2017.

[18] J. C. Materials, "JPS Databook," Tech. Rep., 2015. [Online]. Available: http://jpsglass.net/wp-content/uploads/2015/08/docslide.us_jpsdatabook-55845c9747baf.pdf

[19] Patz Materials and Technologies, "Current PMT Prepreg Resin Systems," 2018. [Online]. Available: http://patzmandt.com/services/

[20] Henkel, "Loctite 5055 Technical Data Sheet," Tech. Rep., 2010. [Online]. Available: http://www.loctite.com.au/aue/content_data/283350_5055EN.pdf

[21] TWP Inc, "325 Mesh Phos. Bronze," 2014. [Online]. Available: www.twpinc.com

[22] R. E. Freeland, N. F. Garcia, and H. Iwamoto, "Wrap-Rib Antenna Technology Development," in *Large Space Antenna Systems Technology*, 1984.

[23] R. I. Harless, "Lightweight, Compactly Deployable Support Structure with Telescoping Members," 2003.

[24] M. W. Thomson, "The AstroMesh deployable reflector," in *IEEE Antennas and Propagation Society International Symposium: Wireless Technologies and Information Networks, APS 1999 - Held in conjunction with USNC/URSI National Radio Science Meeting*, vol. 3, 1999, pp. 1516–1519.

[25] J. Costantine, Y. Tawk, C. G. Christodoulou, J. Banik, and S. Lane, "CubeSat Deployable Antenna Using Bistable Composite Tape-Springs," *IEEE Antennas and Wireless Propagation Letters*, vol. 11, pp. 285–288, 2012.

[26] J. M. Mejia-Ariza, K. Guidanean, T. W. Murphey, and A. Biskner, "Mechanical Characterization of L'Garde Elastomeric Resin Composite Materials," in *51st AIAA/ASME/ASCE/AHS/ASC Structures, Structual Dynamics, and Materials Conference*, Orlando, Florida, 2010.

[27] L. Datashvili, H. Baier, E. Wehrle, T. Kuhn, and J. Hoffmann, "Large Shell-Membrane Space Reflectors," in *51st AIAA/ASME/ASCE/AHS/ASC Structures, Structual Dynamics, and Materials Conference*, Orlando, Florida, 2010.

[28] L. D. Peel, J. Mejia, B. Narvaez, K. Thompson, and M. Lingala, "Morphing Wing Using Elastomeric Composites as Skins," *Journal of Mechanical Design*, vol. 131, 2009.

[29] F. Lopez Jimenez, "Mechanics of thin carbon fiber composites with a silicone matrix," Ph.D. dissertation, California Institute of Technology, 2011.

[30] A. Todoroki, K. Kumagai, and R. Matsuzaki, "Self-deployable Space Structure using Partially Flexible CFRP with SMA Wires," *Journal of Intelligent Material Systems and Structures*, vol. 20, pp. 1415–1424, 2009.

[31] I. Maqueda, S. Pellegrino, and J. Mejia-Ariza, "Characterization of a High Strain Composite Material," in *53rd AIAA/ASME/ASCE/AHS/ASC Structures, Structural Dynamics and Materials Conference, 23-26 April 2012*, Honolulu, Hawaii, 2012.

[32] G. M. Olson, S. Pellegrino, J. Costantine, and J. Banik, "Structural Architectures for a Deployable Wideband UHF Antenna," in *53rd AIAA/ASME/ASCE/AHS/ASC Structures, Structural Dynamics and Materials Conference*, Honolulu, Hawaii, 2012.

[33] Ö. Soykasap, "Deployment analysis of a self-deployable composite boom," *Composite Structures*, vol. 89, no. 3, pp. 374–381, 2009.

[34] J. A. Banik and T. W. Murphey, "Performance Validation of the Triangular Rollable and Collapsible Mast," in *24th Annual AIAAUSU Conference on Small Satellites*, Logan, Utah, 2010.

[35] H. Mallikarachchi and S. Pellegrino, "Quasi-Static Folding and Deployment of Ultrathin Composite Tape-Spring Hinges," *Journal of Spacecraft and Rockets*, vol. 48, no. 1, pp. 187–198, 2011.

[36] A. Stabile and S. Laurenzi, "Coiling dynamic analysis of thin-walled composite deployable boom," *Composite Structures*, vol. 113, no. 1, pp. 429–436, 2014.

[37] Ö. Soykasap, "Micromechanical Models for Bending Behavior of Woven Composites," *Journal of Spacecraft and Rockets*, vol. 43, no. 5, pp. 1093–1100, 2006.

[38] ANSYS, "ANSYS HFSS," 2018. [Online]. Available: www.ansys.com/Products/Electronics/ANSYS-HFSS

[39] Computer Simulation Technology, "CST - 3D Electromagnetic Simulation Software," 2018. [Online]. Available: www.cst.com

[40] Altair, "FEKO - EM Simulation Software," 2018. [Online]. Available: https://www.feko.info/

[41] Antenna Magus, "Antenna Magus," 2018. [Online]. Available: www.antennamagus.com

[42] Dassault Systemes, "Abaqus Unified FEA," 2018. [Online]. Available: www.3ds.com/products-services/simulia/products/abaqus

[43] M. F. Ashby, *Materials Selection in Mechanical Design*, 3rd ed. Oxford: Elsevier, 2005.

[44] Granta Material Intelligence, "CES Selector," 2018. [Online]. Available: www.grantadesign.com/products/ces/

[45] P. Muri, O. Challa, and J. McNair, "Enhancing small satellite communication through effective antenna system design," in *IEEE Military Communications Conference MILCOM*, San Jose, California, 2010.

[46] J. D. Dyson, "The Characteristics and Design of the Conical Log-Spiral Antenna," *IEEE Transactions on Antennas and Propagation*, vol. 13, no. 4, pp. 488–499, 1965.

[47] C. A. Balanis, *Antenna Theory: Analysis and Design*, 3rd ed. Hoboken, New Jersey: John Wiley and Sons, 2005.

[48] The US National Bureau of Standards, "Yagi Antenna Design - NBS Technical Note 688," Tech. Rep., 1976.

[49] T. W. Murphey, S. Jeon, A. Biskner, and G. Sanford, "Deployable Booms and Antennas Using Bi-stable Tape-springs," in *24th Annual AIAA/USU Conference on Small Satellites*, Logan, Utah, 2010.

[50] L. Alminde, K. Kaas, M. Bisgaard, J. Christiansen, and D. Gerhardt, "GOMX-1 Flight Experience and Air Traffic Monitoring Results," in *AIAA/USU Conference on Small Satellites, Technical Session XII*, Logan, Utah, 2014.

[51] R. D. Blevins, *Formulas for Natural Frequency and Mode Shape*, 1st ed. New York: Van Nostrand Reinhold Company, 1979.

[52] D. J. Ewins, *Modal testing : theory, practice, and application*, 2nd ed. Philadelphia: Research Studies Press, 2000.

[53] F. López Jiménez and S. Pellegrino, "Constitutive modeling of fiber composites with a soft hyperelastic matrix," *International Journal of Solids and Structures*, vol. 49, pp. 635–647, 2012.

[54] Bruker, "Hysitron TI 950 Nanomechanical Test Instrument," 2018. [Online]. Available: www.bruker.com/products/surface-and-dimensional-analysis/nanomechanical-test-instruments/standalone-nanomechanical-test-instruments/ti-950-triboindenter/overview.html

[55] A. C. Fischer-Cripps, *Nanoindentation*, 3rd ed. New York: Springer, 2011.

[56] I. M. Daniel and O. Ishai, *Engineering Mechanics of Composite Materials*, 2nd ed. Oxford University Press, 2005.

[57] K. A. Seffen and S. Pellegrino, "Deployment dynamics of tape springs," *Proceedings of the Royal Society A: Mathematical, Physical and Engineering Sciences*, vol. 455, no. 1983, pp. 1003–1048, 1999.

[58] S. Pellegrino, "Folding and Deployment of Thin Shell Structures," in *Extremely Deformable Structures*, D. Bigoni, Ed. Vienna: Springer, 2015, pp. 179–267.

[59] K. Schulgasser, "Confuguration of a bent tape of curved cross-section," *Transactions of the ASME, Journal of Applied Mechanics*, vol. 59, pp. 692–693, 1992.

[60] P. Reu, "Stereo-rig design: Stereo-angle selection - Part 4," *Experimental Techniques*, vol. 37, no. 2, pp. 1–2, 2013.

[61] C. Leclerc, L. Wilson, M. Bessa, and S. Pellegrino, "Characterization of ultra-thin composite triangular rollable and collapsible booms," in *4th AIAA Spacecraft Structures Conference*, Grapevine, Texas, 2017.

[62] C. Sickinger, L. Herbeck, T. Strohlein, and J. Torrez-Torres, "Lightweight Deployable Booms: Design, Manufacture, Verification, and Smart Materials Application," in *55th International Astronautical Congress of the International Astronautical Federation, the International Academy of Astronautics, and the International Institute of Space Law*, Vancouver, Canada, 2004.

[63] K. Ubamanyu and H. Mallikarachchi, "Simulation of Dual-Matrix Composite Boom," in *Proceedings of Annual Session of Society of Structural Engineers*, 2016.

[64] M. Sakovsky, S. Pellegrino, and H. Mallikarachchi, "Folding and Deployment of Closed Cross-Section Dual-Matrix Composite Booms," in *3rd AIAA Spacecraft Structures Conference*, San Diego, CA, 2016.

[65] Livermore Software Technology Corporation, "LS-Dyna Keyword User's Manual," Tech. Rep., 2012.

[66] G. L. Povirk, "Incorporation of microstructural information into models of two-phase materials," *Acta Metallurgica Et Materialia*, vol. 43, no. 8, pp. 3199–3206, 1995.

[67] M. D. Rintoul and S. Torquato, "Reconstruction of the structure of dispersions," *Journal of Colloid and Interface Science*, vol. 186, no. 2, pp. 467–476, 1997.

[68] S. H. R. Sanei, E. J. Barsotti, D. Leonhardt, and R. S. Fertig, "Characterization, synthetic generation, and statistical equivalence of composite microstructures," *Journal of Composite Materials*, vol. 51, no. 13, pp. 1817–1829, 2017.

[69] T. Kanit, S. Forest, I. Galliet, V. Mounoury, and D. Jeulin, "Determination of the size of the representative volume element for random composites: Statistical and numerical approach," *International Journal of Solids and Structures*, vol. 40, no. 13, pp. 3647–3679, 2003.

[70] S. H. R. Sanei and R. S. Fertig, "Uncorrelated volume element for stochastic modeling of microstructures based on local fiber volume fraction variation," *Composites Science and Technology*, vol. 117, pp. 191–198, 2015.

[71] I. M. Gitman, H. Askes, and L. J. Sluys, "Representative volume: Existence and size determination," *Engineering Fracture Mechanics*, vol. 74, no. 16, pp. 2518–2534, 2007.

[72] S. Fliegener, M. Luke, and P. Gumbsch, "3D microstructure modeling of long fiber reinforced thermoplastics," *Composites Science and Technology*, vol. 104, pp. 136–145, 2014.

[73] C. Heinrich, M. Aldridge, A. S. Wineman, J. Kieffer, A. M. Waas, and K. Shahwan, "The influence of the representative volume element (RVE) size on the homogenized response of cured fiber composites," *Modelling and Simulation in Materials Science and Engineering*, vol. 20, no. 7, 2012.

[74] J. Halpin and J. Kardos, "The Halpin-Tsai Equations: A Review," *Polymer Engineering and Science*, vol. 16, no. 5, pp. 344–352, 1976.

[75] R. Foye, "An Evaluation of Various Engineering Estimates of the Transverse Properties of Unidirectional Composites," in *10th National SAMPE Symposium*, San Diego, CA, 1966.

[76] Dassault Systèmes, *Abaqus 6.14 Documentation*, 2014.

[77] A. Kueh and S. Pellegrino, "ABD Matrix of Single-Ply Triaxial Weave Fabric Composites," in *48th AIAA/ASME/ASCE/AHS/ASC Structures, Structural Dynamics, and Materials Conference*, Honolulu, Hawaii, 2007.

[78] J. L. Kuhn and P. Charalambides, "Modeling of Plain Weave Fabric Composite Geometry," *Journal of Composite Materials*, vol. 33, no. 10, pp. 928–940, 1999.

[79] A. Vanaerschot, B. N. Cox, S. V. Lomov, and D. Vandepitte, "Experimentally validated stochastic geometry description for textile composite reinforcements," *Composites Science and Technology*, vol. 122, pp. 122–129, 2016.

[80] L. D. Peel, "Exploration of high and negative Poisson's ratio elastomer-matrix laminates," *Physica Status Solidi (B) Basic Research*, vol. 244, no. 3, pp. 988–1003, 2007.

[81] Mathworks, "How the Genetic Algorithm Works," 2018. [Online]. Available: www.mathworks.com/help/gads/how-the-genetic-algorithm-works.html

[82] J. L. Domber, J. D. Hinkle, L. D. Peterson, and P. A. Warren, "Dimensional Repeatability of an Elastically Folded Composite Hinge for Deployed Spacecraft Optics," *Journal of Spacecraft and Rockets*, vol. 39, no. 5, pp. 646–652, 2002.

[83] A. Brinkmeyer, S. Pellegrino, and P. M. Weaver, "Effects of Long-Term Stowage on the Deployment of Bistable Tape Springs," *Journal of Applied Mechanics*, vol. 83, p. 011008, 2015.

[84] S. Govindarajan, N. A. Langrana, and G. J. Weng, "An experimental and theoretical study of creep of a graphite/epoxy woven composite," *Polymer Composites*, vol. 17, no. 3, pp. 353–361, 1996.

[85] P. Shrotriya and N. R. Sottos, "Viscoelastic response of woven composite substrates," *Composites Science and Technology*, vol. 65, pp. 621–634, 2005.

[86] Q. Zhu, P. Shrotriya, N. R. Sottos, and P. H. Geubelle, "Three-dimensional viscoelastic simulation of woven composite substrates for multilayer circuit boards," *Composites Science and Technology*, vol. 63, no. 13, pp. 1971–1983, 2003.

[87] M. Machado, U. D. Cakmak, I. Kallai, and Z. Major, "Thermomechanical viscoelastic analysis of woven-reinforced thermoplastic-matrix composites," *Composite Structures*, vol. 157, pp. 256–264, 2016.

[88] U. D. Çakmak, F. Hiptmair, and Z. Major, "Applicability of elastomer time-dependent behavior in dynamic mechanical damping systems," *Mechanics of Time-Dependent Materials*, vol. 18, pp. 139–151, 2014.

[89] A. Rauh, R. Hinterhölzl, and K. Drechsler, "Application of the time-temperature superposition principle to the mechanical characterization of elastomeric adhesives for crash simulation purposes," *European Physical Journal: Special Topics*, vol. 206, pp. 15–24, 2012.

[90] R. Schapery and S. Park, "Methods of interconversion between linear viscoelastic material functions. Part I - a numierical methods based on Prony series," *International Journal of Solids and Structures*, vol. 36, no. 11, pp. 1653 – 1675, 1999.

[91] M. L. Williams, R. F. Landel, and J. D. Ferry, "The Temperature Dependence of Relaxation Mechanisms in Amorphous Polymers and Other Glass-forming Liquids," *Journal of American chemical society*, vol. 77, no. 12, pp. 3701–3707, 1955.

[92] N. W. Tschoegl, W. G. Knauss, and I. Emri, "Poisson's Ratio in Linear Viscoelasticity - A Critical Review," *Mechanics of Time-Dependent Materials*, vol. 6, no. 1, pp. 3–51, 2002.

[93] R. S. Lakes and A. Wineman, "On poisson's ratio in linearly viscoelastic solids," *Journal of Elasticity*, vol. 85, no. 1, pp. 45–63, 2006.

[94] K. Kwok, "Mechanics of viscoelastic thin-walled structures," Ph.D. dissertation, California Institute of Technology, 2013.